COMPUTATIONAL STRATEGIES FOR DATA-DRIVEN MODELING OF STOCHASTIC SYSTEMS

A Dissertation
Presented to the Faculty of the Graduate School
of Cornell University
in Partial Fulfillment of the Requirements for the Degree of
Doctor of Philosophy

by
Baskar Ganapathysubramanian
August 2008

COMPUTATIONAL STRATEGIES FOR DATA-DRIVEN MODELING OF STOCHASTIC SYSTEMS

Baskar Ganapathysubramanian, Ph.D.
Cornell University 2008

Many physical systems of fundamental and industrial importance are significantly affected by the underlying fluctuations/variations in boundary, initial conditions as well as variabilities in operating and surrounding conditions. There has been increasing interest in analyzing and quantifying the effects of uncertain inputs in the solution of partial differential equations that describe these physical phenomena. Such analysis naturally leads to a rigorous methodology to design/control physical processes in the presence of multiple sources of uncertainty. Spectral stochastic methods and Monte-Carlo based sampling methods are two approaches that have been used to analyze these problems. As the complexity of the problem or the number of random variables involved in describing the input uncertainties increases, these approaches become highly impractical from implementation and convergence points-of-view, creating a bottle-neck to the utility of stochastic analysis. In this thesis, the sparse grid collocation method based on the Smolyak algorithm is developed as a viable alternate method for solving high-dimensional stochastic partial differential equations. The second bottleneck to the utility of stochastic modelling is the construction of realistic, viable models of the input variability. In the second part of the thesis, a framework to construct realistic input models that encode the variabilities in initial and boundary conditions as well as other parameters using data-driven strategies are developed.

In the third part of the thesis, the data-driven input model generation strategies coupled with the sparse grid collocation strategies are utilized to analyze systems characterized by multi-length scale uncertainties. A stochastic variational multiscale formulation is developed to incorporate uncertain multiscale features. The framework is applied to analyze flow through random heterogeneous media when only limited statistics about the permeability variation are given.

BIOGRAPHICAL SKETCH

The author was born in Madurai, India in October, 1981. After completing his high school, the author was admitted into the Mechanical Engineering program at IIT, Madras in 1999, from where he recieved his Bachelor's degree in engineering in June, 2003. The author entered the doctoral program at the Sibley School of Mechanical and Aerospace Engineering, Cornell University in August, 2003.

The thesis is dedicated to my parents and brother for their constant support and encouragement towards academic pursuits during my school years.

"We have not succeeded in answering all our problems. The answers we have found only serve to raise a whole set of new questions. In some ways we feel we are as confused as ever, but we believe we are confused on a higher level and about more important things." - Posted outside the mathematics reading room,
Tromsø University

ACKNOWLEDGEMENTS

I would like to thank my thesis advisor, Professor Nicholas Zabaras, for his constant support and guidance over the last 3 years. I would also like to thank Professors Tomas Arias and Michael Thompson for serving on my special committee and for their encouragement and suggestions at various times during the course of this work.

The financial support for this project was provided by NASA (grant NAG8-1671) and the National Science Foundation (grant DMI-0113295). I would like to thank the Sibley School of Mechanical and Aerospace Engineering for having supported me through a teaching assistantship for part of my study at Cornell. The computing for this project was supported by the Cornell Theory Center during 2003-2008. The parallel simulators were developed based on open source scientific computation package `Pestc`. I would like to acknowledge the effort of its developers. I am indebted to present and former members of the MPDC group, especially to Dr. Shankar Ganapathysubramanian, and Dr. Lijian Tan.

I would like to thank my good friends Jared, Poorna, Stephanie, Marleen and Dmitry. You have made life beyond the lab fun and fullfilling!

TABLE OF CONTENTS

LIST OF TABLES

LIST OF FIGURES

CHAPTER 1

INTRODUCTION

1.1 Introduction

With the rapid advances in computational power and easier access to high-performance computing platforms, it has now become possible to computationally investigate and design realistic multiscale, multiphysics phenomena. As a direct consequence of this computational ability, there has been growing awareness that the tightly coupled and highly nonlinear systems (that such problems are composed of) are affected to a significant extent by the inherent (usually unresolvable) uncertainties in material properties, fluctuations in operating conditions, and system characteristics. The scale at which these phenomena occur can range from the micro-scale (MEMS devices), macro-scale (devices/components made from polycrystalline or functionally graded materials) to the geological scale (geothermal energy systems).

A good example of how the underlying variability affects performance is in Micro-Electro Mechanical Systems (MEMS). The material properties and the geometric parameters specifying MEMS devices play a significant part in determining their performance. Commercial feasibility requires using low cost manufacturing processes to fabricate the MEMS devices. This often results in significant uncertainties in these parameters, which leads to large variations in the device performance. To accurately predict and subsequently design/tailor the performance of such systems, it becomes essential for one to include the effects of these input uncertainties into the system and understand how they propagate and alter the final solution.

Another class of problems that illustrate the necessity of incorporating the effects of uncertainty (in the lower scales) is in the design and analysis of components made of polycrystalline, functionally graded and other heterogeneous materials. Most engineering devices involve the use of such multi-component materials which constitute a major element in structural, transport, and chemical engineering applications. They are ubiquitous, entering wherever there is a need for cheap, resilient and strong materials. The thermal and elastic properties of such materials (particularly polycrystals) are highly anisotropic and heterogeneous, depending on the local microstructure. Experimental evidence has shown that microstructural variability in polycrystalline materials can have a significant impact on the variability of macro-properties such as strength or stiffness as well as in the performance of devices made of random heterogeneous media. Nevertheless, there has been no dedicated effort in the engineering community for incorporating the effect of such microstructural uncertainty in process or device design even though it is well known that most performance related failures of critical components are directly related with rare events (tails of the PDF) of microstructural phenomena [1, 2, 3, 4, 5, 6]. In addition, no predictive modeling or robust design of devices made of heterogeneous media (MEMs, energetic materials, polycrystals, etc.) is practically feasible without accounting for microstructural uncertainty.

Sources of uncertainties: The above two examples clearly underscore the necessity of incorporating the effects of uncertainty in property variation and operating conditions during the analysis and design of components and devices. This necessity of understanding uncertainty effects extends to almost all complex systems involving multiple coupled physical phenomena. Familiar systems include analysis of thermal transport through devices (nozzle flaps, gears, etc.) that are composed of polycrystals and/or functionally graded materials, hydrodynamic transport through porous media and chemical point operations (e.g. filtration, packed columns. fluidization, sedimentation and distillation operations). Other sources of uncertainty include errors/fluctuations/variations in input constitutive relations, material properties as well as initial/boundary conditions that are used in the model of the system that is being analyzed. These inputs are usually available or derived from experimental data. The presence of uncertainties/perturbations in experimental studies implies that these input parameters have some inherent uncertainties. The uncertainties in the physical model may also be due to inaccuracies or indeterminacies of the initial conditions. This may be due to variation in experimental data or due to variability in the operating environment. Uncertainties may also creep in due to issues in describing the physical system. This may be caused by errors in geometry, roughness, and variable boundary conditions. Uncertainties could also occur due to the mathematical representation of the physical system. Examples include errors due to approximate mathematical models (e.g. linearization of non-linear equations) and discretization errors.

Ingredients for stochastic analysis: There are two key ingredients for constructing a framework to analyze the effects of various sources of uncertainty in a system.

- The first is a mathematically rigorous framework that can be used to define the stochastic differential equations representing the systems along with a *viable solution strategy for the same*. The stochasticity (i.e. inclusion of the effects of uncertainty) in this set of differential equations enters as uncertain boundary and initial conditions, variations in properties, fluctuations and thermal perturbations, or more generally as noise. We denote these as the input uncertainties.

- The second ingredient is a set of techniques to construct usable, realistic models of these input uncertainties. These models should utilize available experimental information and/or expert knowledge. This is a crucial (yet understated) issue with stochastic modeling. It is necessary to provide meaningful/realistic models for the input uncertainty to draw any meaningful conclusions from the resulting solutions. For instance, trying to account for the variability in room temperature (in a simple heat transfer in a room problem) using an input model that allows the room temperature to vary from -100 ^{O}C to +100 ^{O}C is a valid albeit probably useless model.

Solving stochastic partial differential equations: There are various frameworks that have been developed in recent years for incorporating the effects of uncertainties in various systems. The presence of uncertainties can be modelled in the system through reformulation of the governing equations as stochastic partial differential equations (SPDEs). Solution techniques for SPDEs can be broadly classified into two approaches: statistical and non-statistical. Monte-Carlo simulations and its variants constitute the statistical approach to solve SPDEs. This approach gives access to the complete statistics. This method does not approximate the solution space (like the other methods discussed later) The other major attraction of these methods are that their convergence rates do not depend on the number of independent random variables. Further, they are very easy to implement. The only necessity of computing uncertainties using the statistical approach is the availability of a working deterministic code. However, the statistical approach becomes quickly intractable for complex problems in multiple random dimensions. This is because the number of realizations required to acquire good statistics is usually quite large. Furthermore, the number of realizations changes with the variance of the input parameters and the truncation errors in this inherently statistical method are hard to estimate. This has in part been alleviated by improved sampling techniques like Latin hypercube sampling and importance sampling among others [31].

A non-statistical approach consists of approximating and then modelling the uncertainty in the system. One example of this approach is the perturbation method. Here, the random field is expanded about its mean in a truncated Taylor series. This method is usually restricted to small values of uncertainties. A similar method is to expand the inverse of the stochastic operator in a Neumann series. This method is again restricted to small uncertainties and furthermore it is almost impossible to apply these methods to complex problems [7]. In the context of expanding the solution in terms of its statistical moments, there has been some recent work in reformulating the problem as a set of moment differential equations (MDE). The closure equations for these MDE's are then derived from Taylor expansions of the input uncertainty as well as perturbation and asymptotic expansions. The random domain decomposition method [33, 34, 35, 36] coupled with the MDE method has been shown to be successful in solving complex fluid flow problems in porous media having large input variances.

A more recent approach to model uncertainty is based on the spectral stochastic finite element method (SSFEM) [7]. In this method, the random field is discretized directly, i.e uncertainty is treated as an additional dimension along with space and time and a field variable is expanded along the uncertain dimension using suitable expansions. The basic idea is to project the dependent variables of the model onto a stochastic space spanned by a set of complete orthogonal polynomials. These polynomials are functions of a set of random variables $\boldsymbol{\xi}(\theta)$ where θ is a realization of the random event space. Ghanem and Spanos first used SSFEM in linear elastic problems in [7]. Ghanem and co-workers subsequently applied it to transport in random media [8], structural dynamics applications [9] and heat conduction problems [10]. Karniadakis and co-workers applied a generalized polynomial chaos expansion to model uncertainty in diffusion [11], fluid flow applications [12] and transient heat conduction problems [13]. In the original work by Wiener, Gaussian random variables were used with Hermite polynomials. The scheme has been extended to include other random distributions [37, 38, 39, 40, 41, 42]. Error bounds, and convergence studies [43, 44, 45, 46, 47] have shown that these methods exhibit fast convergence rates with increasing orders of expansions. These convergence studies assume that the solutions are sufficiently smooth in the random space.

Like the statistical methods, the SSFEM approach also reduces the problem to a set of deterministic equations. But unlike the statistical methods, the resulting deterministic equations are often coupled. This coupled nature of the deterministic problems makes the solution of the stochastic problem extremely complex as the number of stochastic dimensions increases or the number of expansion terms is increased. In fact, computational complexity of the problem increases combinatorially with the number of stochastic dimensions and the number of expansion terms. This problem is especially acute when dealing with realistic problems in fluid mechanics. The number of random dimensions needed to represent surface fluctuations (roughness) or permeability variations is relatively high ($N \geq 8$). To solve these problems in high-dimensional spaces and to allow non-smooth variations of the solution in the random space, there have been recent efforts to couple the fast convergence of the Galerkin methods with the decoupled nature of Monte-Carlo sampling [48]. Babuska et al. [15] proposed a methodology wherein the Galerkin approximation is used to model the physical space while a collocation scheme is used to sample the random space. A tensor product rule was used to interpolate the variables in stochastic space using products of one-dimensional interpolation functions (double orthogonal polynomials) based on Gauss points. Though this scheme effectively decoupled the deterministic system of equations, the number of realizations required to build the interpolation scheme increased as power of the number of random dimensions (n_{pt}^{N}). Xiu and Hesthaven [16] recently used the Smolyak algorithm to build sparse grid interpolants in high-dimensional space. The sparse grid collocation and cubature schemes have been well studied and utilized in different fields [49, 50, 52, 53, 54]. Using this method, interpolation schemes can be constructed with orders of magnitude reduction in the number of sampled points to give the same level of approximation (up to a logarithmic factor) as interpolation on a uniform grid.

In the standard sparse grid collocation approach, all the dimensions are treated equally. In many problems usually encountered, not all the dimensions are important. That is, the solution varies much more smoothly in some particular dimension than in others. This brings up the possibility of reduction in the computational effort required to solve the stochastic problem by weighting the number of sampling points in the stochastic dimensions according to the solution smoothness in that dimension. But it is not possible to know a priori which dimensions are more important. It is however possible to develop heuristic methods to adaptively sample the stochastic space to reduce the number of function evaluations.

In Chapter. 2, an adaptive extension to the sparse grid collocation method is developed that can automatically detect the important dimensions and bias the sparse sampling towards those dimensions. This results in substantial savings in the computational effort required to solve large dimensional problems. We further utilize these methods to tackle significant problems in natural convection like investigating the effects of surface roughness on the dynamics of Rayleigh-Bénard convection and the effects of heterogeneous porous media on natural convection. We are able to accurately capture equilibrium shifts and efficiently scale to a moderately large number of stochastic dimensions. We further provide a road map to convert any deterministic code to include the effects of input uncertainty in a non-intrusive manner utilizing the adaptive sparse grid collocation method (ASGC).

Constructing reliable stochastic input models: In most complex systems involving multiple coupled physical phenomena, the material (thermo-physical) properties as well as the material distribution (topology) vary at a length scale much smaller than the system size. Familiar systems include analysis of thermal transport through devices (nozzle flaps, gears, etc.) that are composed of polycrystals and/or functionally graded materials, hydrodynamic transport through porous media and chemical flow through packed filtration beds. In such problems, the only information that is usually available experimentally to quantify these variations are statistical correlations. This leads to an analysis of the problem assuming that the property and topological variations are random fields satisfying the experimental correlations. To perform any such analysis, one must first construct models of these variations to be used as inputs in the subsequent uncertainty analysis. The analysis of the effect of such uncertainties on the system needs the construction of a stochastic model (preferably a low-dimensional, continuous mapping) that encodes and quantifies the variation of material topology and properties in a mathematically rigorous way.

There have been very few previous investigations into developing stochastic input representations. The recent work in [19] looks at developing probabilistic models of random coefficients in SPDEs using a maximum likelihood framework. The random domain decomposition (RDD) method was used in [32, 33, 34] to construct probabilistic models for heterogeneous permeability distributions. This methodology has been shown to work very well in describing permeability variations in geological strata [32]. Nevertheless, almost all of these techniques for constructing input models are based on the concept of transforming experimental data and statistics into probability distributions of the property. These techniques are usually highly application specific, require expert knowledge in assigning probabilities and invariably require some amount of heuristic parameter fitting.

The framework developed in this thesis (Chapter. 3) utilizes the available statistical information about the variability of random media to construct a set of plausible realizations of the material topology and property. The framework subsequently encodes *these property realizations* into a low-dimensional continuous space that represents all the possible property variations permitted by the experimental data. By sampling over this low-dimensional equivalent surrogate space, one is essentially sampling over the random space of property variations that satisfy the experimental data. This low-dimensional representation is subsequently used as a stochastic input model in the uncertainty analysis. The major advantages of this framework are the enormous reduction in complexity due to the analysis in a low-dimensional space and more importantly the absence of the requirement of any expert knowledge. In addition, the generality of the mathematical developments results in a framework that can construct input models for any property variability, seamlessly meshing with any reconstruction algorithm and software that produce plausible data sets.

We develop linear and non-linear dimension reduction strategies to embed data variations into a low-dimensional manifold that can serve as the input model for subsequent analysis. The significant features of this framework are as follows: A completely general methodology to generate viable, realistic, reduced-order stochastic input models based on experimental data is proposed. To the best knowledge of the author, this is the first time that such a broad framework for generating models for *any* property variation has been developed. We provide a rigorous mathematical basis for the proposed framework. Furthermore, error estimates and strict convergence estimates of the reduced-order model are provided. The basic model reduction ideas developed are not just limited to generation of viable stochastic input models of property variations. This framework has direct applicability to problems where working in high-dimensional spaces is computationally intractable, for instance, in visualization of property evolution, extracting process-property maps in low-dimensional spaces, among others. Furthermore, the generation of a low-dimensional surrogate space has major ramifications in the optimizing of properties, processes and structures, making complicated operations like searching, contouring and sorting computationally much more feasible.

Transport through random porous media- Stochastic multiscaling: One of the challenging mathematical issues in the analysis of transport through heterogeneous random media is the multiscale nature of the property variations.

Complete response evaluation involving full (fine-scale) spatial and temporal resolution simulations of multiscale systems is extremely expensive. Computational techniques have been developed that solve for a coarse-scale solution by defining an appropriate coarse-scale problem that captures the effect of the fine-scales [94]. The more popular techniques developed for such upscaling fall under the category of multiscale methods viz. the variational multiscale (VMS) method (operator upscaling) [95, 96, 97, 98, 99, 100], the heterogenous multiscale method [101, 102] and the multiscale finite element method [103, 104, 105, 106, 107]. Further related techniques are presented in [108, 109]. These computationally scalable techniques have resulted in the development of black box simulators that have been used with significant success in the solution of large scale transport problems in complex geometries.

The multiscale analysis of such systems inherently assumes that the complete, fine-scale variation of the permeability is known. This assumption limits the applicability of these frameworks since it is usually not possible to experimentally determine the complete structure of the media at the finest scale. In most cases, only a few statistical descriptors of the property variation or the property variation in small test regions can be experimentally determined. This limited information about the permeability necessitates viewing the permeability variation as a random field that satisfies certain statistical properties/correlations. This naturally results in describing the physical phenomena as stochastic multiscale partial differential equations (SPDEs) instead of multiscale partial differential equations (PDEs).

The basic idea to solve the stochastic multiscale set of equations is to extend deterministic multiscale methods to their stochastic analogues. Spectral strategies to pose and solve stochastic multiscale problems have been investigated by Xu [112] and Asokan and Zabaras [42]. Collocation based strategies have recently been developed in [20]. The key is to define appropriate ways to link the fine-scale (subgrid) stochastic variation with the coarse-scale stochastic variation of the dependent variables.

In the final part of the thesis, we utilize the computational strategies developed to analyzing flow through random heterogeneous media given limited statistical information about the multiscale permeability variation. We link stochastic analysis and multiscale methods to investigate this problem. We utilize data-driven strategies to encode the limited information and subsequently construct a finite-dimensional representation of the multiscale permeability variation. A stochastic variational multiscale method is formulated to incorporate the effects of the multiscale (stochastic) permeability. This is based on a straightforward extension to the Mixed Multiscale Finite Element Method [113] to solve the resulting SPDEs.

In the next section we go over some necessary basic mathematical preliminaries before discussing the input model generation strategies and the stochastic sparse grid collocation approach to solving stochastic partial differential equations.

1.2 Some definitions and mathematical preliminaries

For the sake of clarity, let us denote the variable's of interest as θ, $\boldsymbol{u}$, p. Denote by $\mathcal{D}$, a region in R^{nsd}, the domain of interest. $nsd = 1, 2, 3$ is the number of space dimensions over which $\mathcal{D}$ is defined. Denote by $\mathcal{T} \equiv [0, t_{max}]$ the time domain of interest. Denote the boundary of $\mathcal{D}$ as $\partial\mathcal{D}$. Denote the set of governing (deterministic) differential equations defining the evolution of θ as

$$\mathcal{B}(\boldsymbol{u}, p, \theta : \boldsymbol{x}, t, \{q, \alpha\}) = 0. \tag{1.1}$$

The solution of the above set of equations results in functions $\boldsymbol{u} : \mathcal{D} \times \mathcal{T} \rightarrow R^{nsd}$, $p : \mathcal{D} \times \mathcal{T} \rightarrow R$, $\theta : \mathcal{D} \times \mathcal{T} \rightarrow R$. In the above equation, $\{q, \alpha\}$ represent the input conditions, boundary conditions, material parameters as well as any constitutive relations that the physical system may require. For instance in the context of thermal problems, $\{q, \alpha\}$ could represent the heat flux and the thermal conductivity of the system while in the context of elastic deformation problems, $\{q, \alpha\}$ could represent the displacement boundary conditions and the elastic tensor. In conventional deterministic analysis one is given values or a deterministic function representation for $\{q, \alpha\}$ and subsequently solves for the evolution of $(\boldsymbol{u}, p, \theta)$ as a function of these input conditions. As emphasized earlier, in many cases these input parameters have some uncertainty associated with them. This brings up the necessity of stochastic analysis.

Suppose, without loss of generality, that the input quantity α is in fact uncertain. Assume also, for the sake of clarity, that α is a scalar. Denote by Ω_α the space of possible values that α can take. Now, Ω_α can be a set of discrete points $\{\alpha_1, \ldots, \alpha_N\}$ or it can be a continuous range of values $\alpha \in [a, b]$. To rigorously define this notion of variability, the notion of a σ-algebra is introduced. A σ-algebra over a set Ω_α is a nonempty collection $\mathcal{F}$ of subsets of Ω_α that is closed under complementation and countable unions of its members. Intuitively, a σ-algebra of a set/region is a smaller collection of subsets of the given set allowing countably infinite operations/subsets. The use of σ-algebras allows us to restrict our attention to a smaller, and usually more useful, collection of subsets of a given set. The main use of σ-algebras is in the definition of measures on

Ω_α. This is one of the cornerstones of probability theory (the interested reader is referred to [17] for a gentle introduction to σ-algebras in probability theory). The measure that we are usually interested in is the *probability measure*, $\mathcal{P}$, i.e. the probability of a particular subset in the σ-algebra occurring. That is the function/measure $\mathcal{P} : \mathcal{F} \to [0, 1]$. With these definitions, we are now ready to define the probability space in which the variations of the random input α are defined on. Let $(\Omega_\alpha, \mathcal{F}, \mathcal{P})$ be a probability space, where Ω_α is the space of basic outcomes, $\mathcal{F}$ is the minimal σ-algebra of the subsets of Ω_α. $\mathcal{P}$ is the probability measure on $\mathcal{F}$. The σ-algebra can be viewed as a collection of all possible events that can be derived from the basic outcomes in Ω_α and have a well defined probability with respect to $\mathcal{P}$. The notation ω_α will be used to refer to the basic outcomes in the sample space, i.e., $\omega_\alpha \in \Omega_\alpha$.

From a deterministic version of α we now have a probabilistic definition of $\alpha(\omega_\alpha)$. Note that $\alpha(\omega_\alpha)$ is still an abstract quantity, that lies in an abstract probability space $(\Omega_\alpha, \mathcal{F}, \mathcal{P})$. In Chapter. 3, we will look at different ways of representing this random process for straightforward utility in a computational framework. This probabilistic definition of $\alpha(\omega_\alpha)$ necessitates a redefinition of the governing equation. This can be done naturally as follows: define the evolution of $(\boldsymbol{u}, p, \theta)$ as

$$\begin{aligned} \mathcal{B}(\boldsymbol{u}, p, \theta : \boldsymbol{x}, t, \{q, \alpha(\omega_\alpha)\}) &= 0. & (1.2) \\ \equiv \mathcal{B}(\boldsymbol{u}, p, \theta : \boldsymbol{x}, t, \omega_\alpha) &= 0. & (1.3) \end{aligned}$$

Now, the dependent variable θ depends not only on $(\boldsymbol{x}, t)$ but also on the space Ω_α. The solution of the above set of equations results in functions $\boldsymbol{u} : \mathcal{D} \times \mathcal{T} \times \Omega_\alpha \to R^{nsd}$, $p : \mathcal{D} \times \mathcal{T} \times \Omega_\alpha \to R$, $\theta : \mathcal{D} \times \mathcal{T} \times \Omega_\alpha \to R$

CHAPTER 2

SOLVING STOCHASTIC PARTIAL DIFFERENTIAL EQUATIONS: A SPARSE GRID COLLOCATION APPROACH

2.1 Problem definition

The incorporation of uncertain inputs in the analysis of a system defined by a set of differential equations results in a set of stochastic differential equations

$$\mathcal{B}(\boldsymbol{u}, p, \theta : \boldsymbol{x}, t, \omega_\alpha) \quad = \quad 0. \tag{2.1}$$

defined over an abstract probability space $(\Omega_\alpha, \mathcal{F}, \mathcal{P})$. The solution methodology to solve of the above set of coupled differential equations is to first reduce the complexity of the problem by reducing the probability space into a finite dimensional space. In some cases the random field $\alpha(\boldsymbol{x}, \omega)$ can be represented/described by a finite length random vector $[\xi^1, \ldots, \xi^N] : \Omega \rightarrow R^N$. In other cases the random field can have a spatial correlation or variation. There is rich literature on techniques to extract/fit correlations for these random fields from input experimental/numerical data. This is an area of intense ongoing research [19]. In Chapter. 3, we detail some of these techniques. Using the 'finite-dimensional noise assumption' [45], the random process is decomposed into a finite set of random variables. A commonly used decomposition is via the Karhunen-Loève expansion. In the K-L expansion, the covariance kernel of the input random process is spectrally decomposed to a finite set of uncorrelated random variables. Upon decomposition and characterization of the random inputs into N random variables, $\xi^i(\omega)$ $i = 1, \ldots, N$, the solution to the coupled system of Eqs. (2.33)-(2.35) can be described by this set of random variables.

Thus we can consider the following:

$$\begin{aligned}
\boldsymbol{u}(\boldsymbol{x}, t, \omega) &= \boldsymbol{u}(\boldsymbol{x}, t, \xi^1(\omega), \ldots, \xi^N(\omega)),\\
\theta(\boldsymbol{x}, t, \omega) &= \theta(\boldsymbol{x}, t, \xi^1(\omega), \ldots, \xi^N(\omega)),\\
p(\boldsymbol{x}, t, \omega) &= p(\boldsymbol{x}, t, \xi^1(\omega), \ldots, \xi^N(\omega)).
\end{aligned}$$

It is usually assumed that $\xi^i(\omega)$ are independent random variables with probability distribution functions $\rho_i : \Gamma^i \to R$ with bounded ranges, Γ^i. The joint probability density of the N-tuple in the above equations $\boldsymbol{\xi} = (\xi^1(\omega), \ldots, \xi^N(\omega))$ is then given by

$$\rho(\boldsymbol{\xi}) = \prod_{i=1}^{N} \rho_i(\xi^i), \quad \forall\, \boldsymbol{\xi} \in \Gamma, \tag{2.2}$$

where the support $\Gamma = \prod_{i=1}^{N} \Gamma^i \subset R^N$. The outcome of the above procedure is that the set of Eqs.2.1) can now be written as a set of differential equations in $(N + nsd)$ dimensions, where N is the dimensionality of the truncated random space Γ and nsd is the dimensionality of the physical space D:

$$\mathcal{B}(\boldsymbol{u}, p, \theta : \boldsymbol{x}, t, \boldsymbol{\xi}) = 0. \tag{2.3}$$

2.2 Generalized polynomial chaos expansions

In this approach, the dependent variables $(\boldsymbol{u}, p, \theta)$ are regarded as random processes. These random fields are then expanded into a truncated series. One could use the Karhunen-Loève expansion to represent these fields, but unfortunately one does not a priori know the correlation functions for these variables. The generalized polynomial chaos expansion is used to represent the variables in terms of orthogonal polynomials in the stochastic space spanned by $\boldsymbol{\xi} \in \Gamma$.

This is written as

$$\kappa(\boldsymbol{x}, t, \omega) = \sum_{i=0}^{P} \kappa_i(\boldsymbol{x}, t)\Phi_i(\xi^i(\omega)), \tag{2.4}$$

where κ is any of the dependent variables. Here κ_i are the deterministic coefficients that can be thought of as being similar to the coefficients in a Fourier expansion of a function. Note that the possible infinite summation has been truncated to only P terms. The random trial basis functions $\{\Phi_i\}$ are chosen according to the type of random variable $\{\xi^i\}$ that has been used to describe the input random field. For example, if Gaussian random variables are chosen then the Askey based orthogonal polynomials $\{\Phi_i\}$ are chosen to be Hermite polynomials, if ξ^i are chosen to be uniform random variables, then $\{\Phi_i\}$ must be Legendre polynomials (for a complete description of the GPCE scheme, the interested reader is referred to [41]). The total number of expansions terms is determined by the stochastic dimension (N) and the highest-order (p) of the orthogonal polynomials as follows:

$$P + 1 = \frac{(N + p)!}{N!p!}. \tag{2.5}$$

The GPCE is used to expand all the dependent variables in terms of the orthogonal polynomials. Substituting these expansions into the governing equation, Eq. (2.3), gives:

$$\mathcal{B}(\sum_{i=0}^{P} \boldsymbol{u}_i\Phi_i, \sum_{i=0}^{P} p_i\Phi_i, \sum_{i=0}^{P} \theta_i\Phi_i : \boldsymbol{x}, t, \boldsymbol{\xi}) = 0. \tag{2.6}$$

Following this, a Galerkin projection of the above equation onto each polynomial basis Φ_i is conducted to ensure that the error is orthogonal to the functional space spanned by the finite dimensional basis Φ_i:

$$\langle \mathcal{B}(\sum_{i=0}^{P} \boldsymbol{u}_i\Phi_i, \sum_{i=0}^{P} p_i\Phi_i, \sum_{i=0}^{P} \theta_i\Phi_i : \boldsymbol{x}, t, \boldsymbol{\xi}), \;\; \Phi_j\rangle = 0. \tag{2.7}$$

where $\langle a, b\rangle$ is the inner product of the functions a and b over the ensemble ($\langle a, b\rangle = \int_\Omega ab d\boldsymbol{x}$). By using the orthogonality of the polynomial basis, we can obtain a set of $(P + 1)$ coupled equations for each random mode u_i, p_i, θ_i. By utilizing the polynomial chaos expansion followed by the Galerkin projection, the randomness has been transferred from the dependent variables to the basis polynomials. The resulting governing equations for the expansion coefficients are deterministic.

This methodology has been very successful in solving SPDEs [7, 11, 12, 13, 37, 39, 41, 42, 46]. We will restrict our discussion to the disadvantages of this method so as to motivate the next few sections. The coupled nature of the expansion coefficients makes the implementation of the GPCE method non-trivial. Substantial effort has to be put in to convert a validated deterministic code into a feasible stochastic one. As the number of stochastic dimensions increases, the rapidly growing number $(P + 1)$ of basis functions effectively reduces the efficiency of the method. New faster and more efficient solvers and data processing methodologies are necessary for the efficient solution of higher-dimensional problems. The major constraint for the utility of this methodology is the coupled nature of the resulting equations. This resulted in the search for a method that combined the fast convergence and error estimates of the spectral Galerkin method with the decoupled nature of the more statistical methods like the Monte-Carlo methods.

2.3 Collocation methods

In the spectral Galerkin method described in the previous section, the spatial domain is approximated using a finite element discretization and the stochastic space is also approximated using a spectral element discretization. This representation of the stochastic space causes the coupled nature of the resulting equations. Another approach is to have a finite element approximation for the spatial domain and approximate the multidimensional stochastic space using interpolating functions. The interpolating functions are mutually orthogonal and the resulting equations are decoupled. This approach is called the collocation approach, where one computes the deterministic solution at various points in the stochastic space and then builds an interpolated function that best approximates the required solution. We now detail the issues involved in constructing the stochastic solution using the collocation method. We follow the spirit of the discussion in Xiu et.al [16] to give an intuitive development of the method.

2.3.1 Fundamentals of the collocation method

The basic idea of the collocation approach is to build an interpolation function for the dependent variables using their values at particular points in the stochastic space. The Galerkin projection is then applied to find that interpolation function which minimizes the projected error of the approximated system. Denote by $\boldsymbol{\xi}$ any point in the random space $\Gamma \subset R^N$, by Π_N, the space of all N-variate polynomials and by Π_N^p, the subspace of polynomials of total degree at most p.
The problem of interpolation can be stated as follows:
Given a set of nodes $\Theta_N = \{\boldsymbol{\xi}_i\}_{i=1}^M$ in the N-dimensional random space Γ and the smooth function $f : R^N \rightarrow R$, find the polynomial $\mathcal{I}f$ such that $\mathcal{I}f(\boldsymbol{\xi}_i) = f(\boldsymbol{\xi}_i)$, $\forall\ i = 1, \ldots, M$.

The polynomial approximation $\mathcal{I}f$ can be expressed using the Lagrange interpolation polynomials as follows:

$$\mathcal{I} f(\boldsymbol{\xi}) = \sum_{k=1}^{M} f(\boldsymbol{\xi}_k) L_k(\boldsymbol{\xi}), \tag{2.8}$$

where $L_i(\boldsymbol{\xi}_j) = \delta_{ij}$. Now, once the interpolating polynomial have been generated using the nodes $\{\Theta_N\}$, the value of the function at any point $\boldsymbol{\xi} \in \Gamma$ is approximately $\mathcal{I} f(\boldsymbol{\xi})$. The Lagrange interpolated values of $(\boldsymbol{u}, p, \theta)$, denoted by $(\hat{\boldsymbol{u}}, \hat{p}, \hat{\theta})$ are as follows:

$$(\hat{\boldsymbol{u}}(\boldsymbol{\xi}), \hat{p}(\boldsymbol{\xi}), \hat{\theta}(\boldsymbol{\xi})) = (\mathcal{I}\boldsymbol{u}(\boldsymbol{\xi}), \mathcal{I} p(\boldsymbol{\xi}), \mathcal{I}\theta(\boldsymbol{\xi})) = \sum_{k=1}^{M} (\boldsymbol{u}(\boldsymbol{\xi}_k), p(\boldsymbol{\xi}_k), \theta(\boldsymbol{\xi}_k)) L_k(\boldsymbol{\xi}). \tag{2.9}$$

Substituting this into the governing equation, Eq. (2.3), gives

$$\mathcal{B}(\sum_{i=1}^{M} \boldsymbol{u}(\boldsymbol{\xi}_i) L_i(\boldsymbol{\xi}), \sum_{i=1}^{M} p(\boldsymbol{\xi}_i) L_i(\boldsymbol{\xi}), \sum_{i=1}^{M} \theta(\boldsymbol{\xi}_i) L_i(\boldsymbol{\xi}) : x, t, \boldsymbol{\xi}) = 0. \tag{2.10}$$

The interpolation form of the solution immediately leads to M decoupled deterministic systems

$$\mathcal{B}(\boldsymbol{u}(\boldsymbol{\xi}_i), p(\boldsymbol{\xi}_i), \theta(\boldsymbol{\xi}_i) : \boldsymbol{x}, t, \boldsymbol{\xi}_i) = 0, \;\; i = 1, \ldots, M. \tag{2.11}$$

The collocation method collapses the $(N + d)$-dimensional problem to solving M deterministic problems in d dimensions. The statistics of the random solution can then be obtained by

$$< z^{\alpha}(x) >= \sum_{k=1}^{M} z^{\alpha}(x, \boldsymbol{\xi}_k) \int_{\Gamma} L_k(\boldsymbol{\xi}) \rho(\boldsymbol{\xi}) d\boldsymbol{\xi}. \tag{2.12}$$

Remark 1. *Relation to the spectral Galerkin method:* Babuska and coworkers [44, 45] realized that by choosing appropriate basis functions, the so-called double orthogonal functions, the spectral stochastic Galerkin formulation can also be made decoupled. This is specific to the case when the random input is a linear functions of the input random variables. They also showed that in case the input uncertainties are multi-linear combinations of the random variables $\{\xi^i(\omega)\}$ (as would happen if one uses the K-L expansion to truncate the input random fields to a finite set of random variables), the solution obtained from the collocation procedure coincides with the stochastic Galerkin solution [15]. They argue that the collocation method can be seen as a pseudo-spectral Galerkin method with some distinct advantages.

2.3.2 Building the interpolating polynomial basis

In most problems involving input uncertainties, the final objective is usually to compute the moments of the dependent variables (Eq. 3.14) and/or generate the probability distribution functions (PDFs) at some point in the solution phase space. This is accomplished through specific quadrature and sampling operations on the interpolation function. The analysis and construction of the interpolation function is usually introduced through a univariate interpolation formula.

Let $f : [a, b] \to R$ be a function that has to be interpolated by a polynomial $\mathcal{I}_n(f)$ using a finite number of nodes $a \leq x_0 < x_1 \ldots < x_n \leq b$. There exists a (unique) polynomial $\mathcal{I}_n(f) \in \Pi_1^n$ satisfying $\mathcal{I}_n(f)(x_i) = f(x_i)$ for $i = 0, 1 \ldots, n$. This can be written in the form:

$$\mathcal{I}_n(f)(x) = \sum_{i=0}^{n} f(x_i) L_i(x), \tag{2.13}$$

where the basis polynomials are given by

$$L_i(x) = \prod_{k=0, k \neq i}^{n} \frac{x - x_k}{x_i - x_k}. \tag{2.14}$$

As the number of points n increases, the interpolation function $\mathcal{I}_n(f)$ represents the function f better. This is irrespective of how one chooses the nodes $\{x_i\}_{i=0}^{n}$.

However, uniform convergence ($||f - \mathcal{I}_n(f)||_\infty \rightarrow 0$ as $n \rightarrow \infty$) is not guaranteed for any arbitrary distribution of the nodes. Utilizing a Taylor series expansion, the interpolation error for a function $f \in C^{n+1}[a, b]$ at a point x is given by [54]

$$f(x) - \mathcal{I}_n(f)(x) = \frac{f^{n+1}(\xi)}{(n+1)!} \prod_{j=0}^{n} (x - x_j). \tag{2.15}$$

The magnitude of the $(n+1)^{th}$ derivative could outweigh the product of the nodes. But there are unique node distributions that exist where uniform convergence with the number of nodes can be proved if $f \in C^1[a, b]$.

One way of quantifying the approximating quality of the interpolating polynomial for a given node distribution (denoted by X) is to compare it with a polynomial whose nodes have been selected in an optimal way to theoretically minimize the interpolation error. This *best approximation polynomial* $p_n^*(f) \in \Pi_1^n$, is defined as the polynomial with the following property [54]:

$$||f - p_n^*(f)||_\infty \leq ||f - \mathcal{I}(f)||_\infty \ \forall \ \mathcal{I}(f) \in \Pi_1^n. \tag{2.16}$$

The distance of any interpolation polynomial $\mathcal{I}(f)$ from the best approximation polynomial is measured in terms of the Lebesgue constant $\Lambda_n(X)$ as follows [54]:

$$||f - \mathcal{I}(f)||_\infty \leq ||f - p_n^*(f)||_\infty (1 + \Lambda_n(X)), \tag{2.17}$$

where $\Lambda_n(X) = \max_{x \in [a,b]} (\sum_{i=0}^{n} |L_i(x)|)$ where X is any distribution of the nodes. It is apparent that $\Lambda_n(X)$ does not depend on the function f but in fact only depends on the distribution of the points X. Therefore it is possible to construct a priori, sets of nodes X with a small Lebesgue constant. One such type of node distribution is the interpolation based at the Chebyshev extrema [54].

Once the type of support nodes $\{X\}$ has been chosen and the Lebesgue constant for the node distribution computed, it is straightforward to arrive at error bounds for the polynomial interpolation function $\mathcal{I}^X$. For instance, the error bound for the Chebyshev node based interpolation function of the function $f \in C^k$ is given by [54],[55]

$$\|f - \mathcal{I}^X(f)\|_\infty \leq Cn^{-k}\log(n). \tag{2.18}$$

2.3.3 From univariate interpolation to multivariate interpolation

When one is dealing with multiple stochastic dimensions, it is straightforward to extend the interpolation functions developed in one dimension to multiple dimensions as simple tensor products. If $u(\boldsymbol{\xi})$ is a function that has to be approximated in N dimensional space, and $\mathbf{i} = (m_1, m_2, \ldots m_N)$ are the number of nodes used in the interpolation in N dimensions, the full-tensor product interpolation formula is given as

$$\begin{aligned} \mathcal{I}^N u(\boldsymbol{\xi}) &= (\mathcal{I}^{i_1} \otimes \ldots \otimes \mathcal{I}^{i_N})(u)(\boldsymbol{\xi}) \\ &= \sum_{j_1=1}^{m_1} \ldots \sum_{j_N=1}^{m_N} u(\xi_{j_1}^{i_1}, \ldots, \xi_{j_N}^{i_N}).(L_{j_1}^{i_1} \otimes \ldots \otimes L_{j_N}^{i_N}), \end{aligned} \tag{2.19}$$

where $\mathcal{I}^{i_k}$ are the interpolation functions in the i_k direction and $\xi_{j_m}^{i_k}$ is the ${j_m}^{th}$ point in the k^{th} coordinate. Clearly, the above formula needs $m_1 \times \ldots \times m_N$ function evaluations, at points sampled on a regular grid. In the simplest case of using only two points in each dimension, the total number of points required for a full-tensor product interpolation is $M = 2^N$. This number grows very quickly as the number of dimensions is increased. Thus one has to look at intelligent ways of sampling points in the regular grid described by the full-tensor product formula so as to reduce the number of function evaluations required. This immediately leads to sparse collocation methods that are briefly reviewed next.

2.4 Sparse grid collocation methods

For the univariate case, Gauss points and Chebechev points have least interpolation error (for polynomial approximations). In the case of multivariate interpolation, one feasible methodology that has been used is to construct interpolants and nodal points by tensor products of one-dimensional interpolants and nodal points. An obvious disadvantage of this strategy is that the number of points required increases combinatorially as the number of stochastic dimensions is increased.

The Smolyak algorithm provides a way to construct interpolation functions based on a minimal number of points in multi-dimensional space. Using Smolyak's method, univariate interpolation formulae are extended to the multivariate case by using tensor products in a special way. This provides an interpolation strategy with potentially orders of magnitude reduction in the number of support nodes required. The algorithm provides a linear combination of tensor products chosen in such a way that the interpolation property is conserved for higher dimensions.

2.4.1 Smolyak's construction of sparse sets

Smolyak's algorithm provides a means of reducing the number of support nodes from the full-tensor product formula while maintaining the approximation quality of the interpolation formula up to a logarithmic factor. Consider the one-dimensional interpolation formula

$$\mathcal{U}^m(f) = \sum_{j=1}^{m} f(x_j) L_j. \tag{2.20}$$

Let us denote the set of points used to interpolate the one-dimensional function by $\Theta^{(k)}$. For instance, $\Theta^{(3)}$ could represent the Chebyshev points that interpolate a third-order polynomial. The Smolyak algorithm constructs the sparse interpolant $A_{q,N}$ (where N is the number of stochastic dimensions and $q-N$ is the order of interpolation) using products of one-dimensional functions. $A_{q,N}$ is given as [53, 54]

$$A_{q,N}(f) = \sum_{q-N+1\leq|\mathbf{i}|\leq q} (-1)^{q-|\mathbf{i}|}.\binom{N-1}{q-\mathbf{i}}.(\mathcal{U}^{i_1} \otimes \ldots \otimes \mathcal{U}^{i_N}), \tag{2.21}$$

with $A_{N-1,N} = 0$ and where $\mathbf{i} = (i_1, \ldots, i_N)$ and $|\mathbf{i}| = i_1 + \ldots + i_N$. Here i_k can be thought of as the level of interpolation along the $k-th$ direction. The Smolyak algorithm builds the interpolation function by adding a combination of one dimensional functions of order i_k with the constraint that the sum total ($|\mathbf{i}| = i_1 + \ldots + i_N$) across all dimensions is between $q-N+1$ and q. The structure of the algorithm becomes clearer when one considers the incremental interpolant, Δ^i given by [49, 52, 53, 54]

$$\mathcal{U}^0 = 0, \;\; \Delta^i = \mathcal{U}^i - \mathcal{U}^{i-1}. \tag{2.22}$$

The Smolyak interpolation $\mathscr{A}_{q,N}$ is then given by

$$\begin{aligned} \mathscr{A}_{q,N}(f) &= \sum_{|\mathbf{i}|\leq q}(\Delta^{i_1} \otimes \ldots \otimes \Delta^{i_N})(f) \\ &= \mathscr{A}_{q-1,N}(f) + \sum_{|\mathbf{i}|=q}(\Delta^{i_1} \otimes \ldots \otimes \Delta^{i_N})(f). \end{aligned} \tag{2.23}$$

To compute the interpolant $\mathscr{A}_{q,N}(f)$ from scratch, one needs to compute the function at the nodes covered by the sparse grid $\mathcal{H}_{q,N}$

$$\mathcal{H}_{q,N} = \bigcup_{q-N+1\leq|\mathbf{i}|\leq q} (\Theta_1^{(i_1)} \times \ldots \times \Theta_1^{(i_N)}). \tag{2.24}$$

The construction of the algorithm allows one to utilize all the previous results generated to improve the interpolation (this is immediately obvious from

Eq. (2.23)). By choosing appropriate points (like the Chebyshev and Gauss-Lobatto points) for interpolating the one-dimensional function, one can ensure that the sets of points $\Theta^{(i)}$ are nested ($\Theta^{(i)} \subset \Theta^{(i+1)}$). To extend the interpolation from level i to $i+1$, one only has to evaluate the function at the grid points that are unique to $\Theta^{(i+1)}$, that is, at $\Theta^{i}_{\Delta} = \Theta^{i} \backslash \Theta^{i-1}$. Thus, to go from an order $q-1$ interpolation to an order q interpolation in N dimensions, one only needs to evaluate the function at the differential nodes $\Delta\mathcal{H}_{q,N}$ given by

$$\Delta\mathcal{H}_{q,N} = \bigcup_{|\mathbf{i}|=q} (\Theta^{i_1}_{\Delta} \otimes \ldots \otimes \Theta^{i_N}_{\Delta}). \tag{2.25}$$

2.4.2 Interpolation error

As a matter of notation, the interpolation function used will be denoted $A_{N+k,N}$, where k is called the level of the Smolyak construction. The interpolation error using the Smolyak algorithm to construct multidimensional functions (using the piecewise multilinear basis) is [53, 54]

$$||f - A_{q,N}(f)|| = \mathcal{O}(M^{-2}|log_2 M|^{3(N-1)}), \tag{2.26}$$

where $M = dim(\mathcal{H}(q,N))$ is the number of interpolation points. On the other hand, the construction of multidimensional functions using polynomial basis functions gives an interpolation error of [53, 54]

$$||f - A_{q,N}(f)|| = \mathcal{O}(M^{-k}|log_2 M|^{(k+2)(N+1)+1}), \tag{2.27}$$

assuming that the function $f \in F^k_d$, that is, it has continuous derivatives up to order k.

2.4.3 Solution strategy

The final solution strategy is as follows: A stochastic collocation method in $\Gamma \subset R^N$ along with a finite element discretization in the physical space $D \subset R^d$ is used. Given a particular level of interpolation of the Smolyak algorithm in N-dimensional random space, we define the set of collocation nodes $\{\boldsymbol{\xi}_k\}_{k=1}^M$ on which the interpolation function is constructed. Given a piecewise FEM mesh X_d^h , find, for $k = 1, \ldots, M$, solutions

$$(\boldsymbol{u}_k^h(x), p_k^h(x), \theta_k^h(x)) = (\boldsymbol{u}^h(x, \boldsymbol{\xi}_k), p^h(x, \boldsymbol{\xi}_k), \theta^h(x, \boldsymbol{\xi}_k)), \tag{2.28}$$

such that

$$\mathcal{B}(\boldsymbol{u}^h(\boldsymbol{\xi}_i), p^h(\boldsymbol{\xi}_i), \theta^h(\boldsymbol{\xi}_i) : \boldsymbol{\xi}_i, x, t) = 0, \;\; i = 1, .., M. \tag{2.29}$$

The final numerical solution takes the form

$$z(x, \boldsymbol{\xi}) = \sum_{k=1}^{M} z_k(x) \hat{L}_k(\boldsymbol{\xi}), \tag{2.30}$$

where z is one of $\boldsymbol{u}^h$, p^h, θ^h, and $\hat{L}_k$ are the multidimensional interpolation functions constructed using the Smolyak algorithm.

Recently, rigorous error estimates for the collocation based stochastic methodology have been developed in [16] and [56]. The error is basically split into a superposition of errors: the error due to the discretization of the deterministic solution, ε_D, and the error due to the interpolation of the solution in stochastic space, ε_I. This error can be written as $\varepsilon \leq (C_1 \varepsilon_D^2 + C_2 \varepsilon_I^2)^{1/2}$, where C1 and C2 are constants independent of the discretizations in physical space and stochastic space.

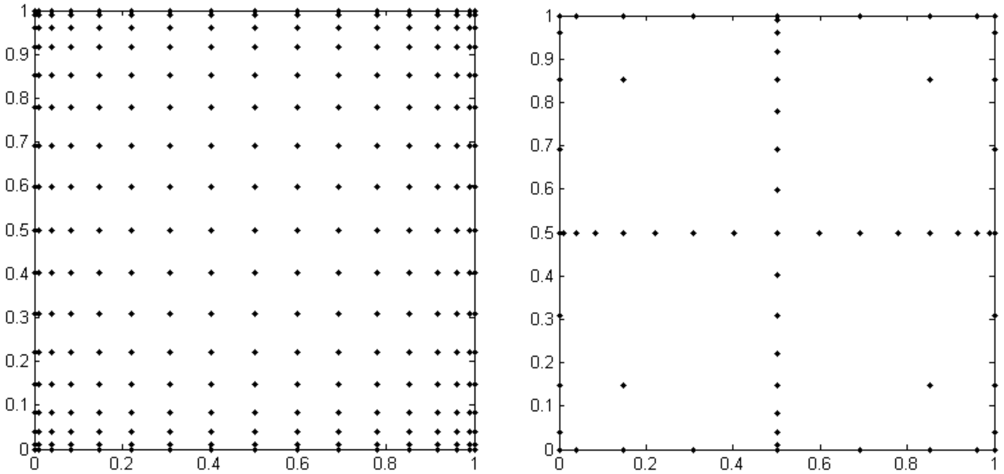

Figure 2.1: Collocation nodes for a two-dimensional problem in a level 4 full (left) and sparse grid (right). Both the grids are constructed from the same level of one-dimensional interpolation functions. The sparse grid offers marginally worse interpolation properties with huge improvements in the number of points sampled.

2.4.4 Numerical illustrations

In this subsection, we illustrate the sparse grid interpolation method with a few examples which will also serve as a motivation for the development of the adaptive sparse grid methodology.

Grid sizes

Fig. 2.1 shows the two-dimensional interpolation nodes for the sparse grid along with the two-dimensional tensor product grid based on the same one-dimensional interpolation nodes. As the number of dimensions or the level of interpolation increases, the number of points to construct interpolants with similar errors using the sparse grid collocation method reduces appreciably as compared to the full-tensor product collocation method.

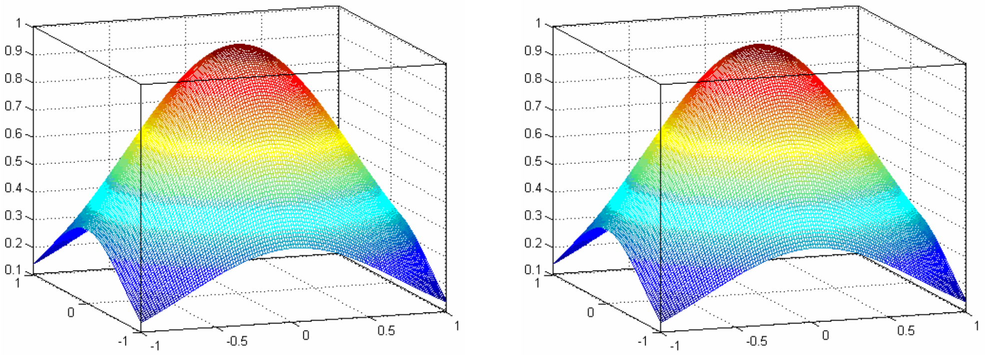

Figure 2.2: Comparison of the exact (left) and interpolant (right) functions.

Interpolating smooth functions

The sparse grid collocation method requires function evaluations at a finite number of discrete points Θ. These function evaluations are usually finite element simulations of the deterministic problem at each stochastic point Θ_i. To illustrate the methodology, we will instead assume that certain analytical functions are the inputs at specific nodal points. Consider the function $f = e^{-x^2-\varrho y^2}$, where ϱ is a positive number. This function is analytically smooth. For $\varrho = 1$, the function is isotropically smooth. The computational domain is $[-1,1] \times [-1,1]$. Fig. 2.2 compares the actual function and the interpolated function. The absolute error $\max |f - \mathcal{A}_{q,2}(f)|$ is 3×10^{-5} when considering 3329 points. This corresponds to building the sparse interpolant using one-dimensional interpolating functions up to order 9. To achieve a similar interpolation error using the full-tensor product grid would require 263169 points.

Now we gradually change the value of ϱ to make the function more anisotropic. The interpolation error versus the number of nodes in the sparse grid is plotted in Fig. 2.3 for ϱ varying from 1 to 10000. Notice that as the anisotropy increases, the variation of the function along one direction becomes

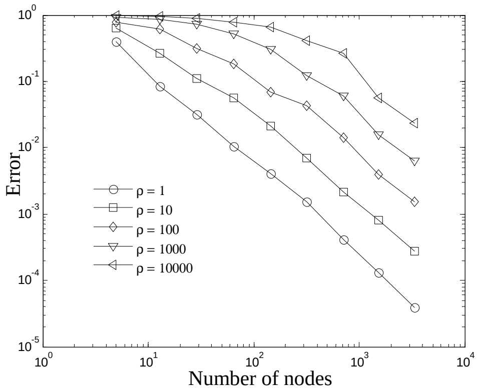

Figure 2.3: Interpolation error for anisotropic functions: As ϱ increases, the function becomes steeper (Fig. 2.4). More points are required to accurately interpolate the function.

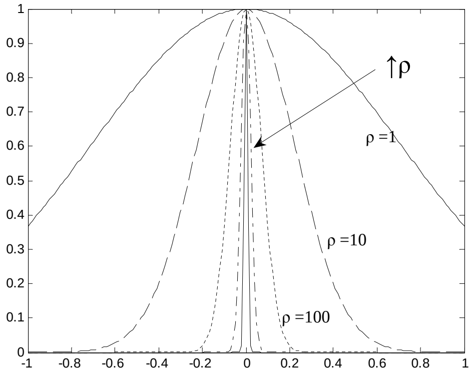

Figure 2.4: Slice of the function in the x plane. The arrow shows the direction of increasing ϱ.

progressively steeper (see Fig. 2.4). Thus, more support nodes are required to accurately interpolate the function. To reach an accuracy of 2×10^{-2} the number of points required are 65, 145, 321, 705, 1537 and 3329, for ρ = 1, 10, 100, 1000 and 10000, respectively.

The critical point to note here is that even though only one dimension of the function is very steep (as ϱ increases), the sparse grid increases the node allocation in all directions. This suggests that one can further reduce the number of function evaluations if we can detect the directions in which the function varies more smoothly than the others.

Interpolating discontinuous functions

In many physical systems governed by SPDEs, one is primarily interested in analyzing mode jumps and equilibrium shifts that occur due to small variations in the random variables. One extreme case is when there is a sharp (finite) discontinuity in the solution across a particular random variable. We are interested in the performance of the sparse grid collocation method in capturing this discontinuity.

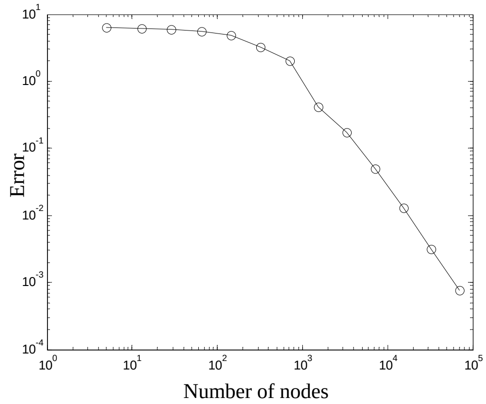

Figure 2.5: Interpolation error for a discontinuous function.

Consider a function $f = e^{-x^2+2\text{sign}(y)}$ in the domain $[-1, 1] \times [-1, 1]$. Here sign is the signum function: 1, when y is positive and -1, otherwise. The function f has a sharp discontinuity along the $y = 0$ plane. On the other hand, the function is very smooth in the x direction. That is, the function $f(x, c)$, for a constant c is an exponentially decaying function. The sparse grid method is used to build the interpolation for this function. Fig. 2.5 plots the error as a function of the number of support nodes used by the algorithm. Notice that the error reduction is sub-linear during the first few interpolation levels. This is because of the error

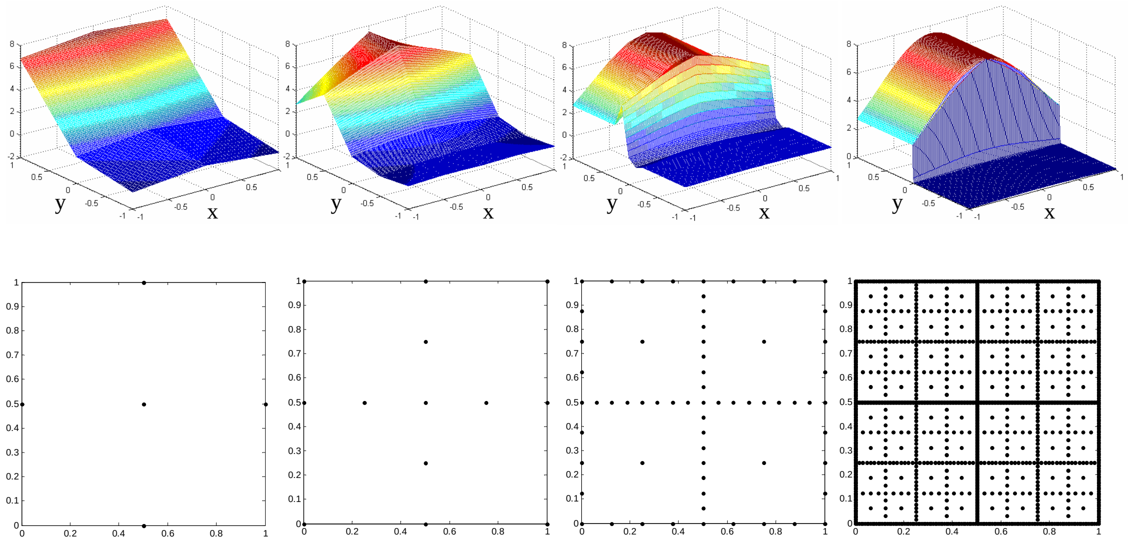

Figure 2.6: Top row: Interpolated function at different levels of interpolation, Bottom row: The corresponding sparse grids used.

caused by the jump across the x axis.

Fig. 2.6 plots the 'evolution' of the interpolation function as the number of support nodes increases. The first row shows a plot of the interpolated function while the second row shows the corresponding support nodes required to build that particular interpolation function. To construct a polynomial interpolation for the function f with an error in the range of 2×10^{-3} required 32769 support nodes. But notice that the sparse grid adds points equally in both dimensions, even when the function varies very smoothly in one dimension.

The two examples discussed above illustrate the possibility of further reducing the number of needed function evaluations for cases in which (i) the functional dependence on the stochastic variables is additive or nearly additive, (ii) the function is anisotropic in the stochastic dimensions. and (iii) when discontinuities exist in the function in certain dimensions.

The choice of support nodes now depends implicitly on the function that one is interpolating. Therefore, one must decide which nodes to sample on-the-fly for minimizing the number of function evaluations. This naturally leads to the idea of adaptive sparse grid collocation, which is discussed in the next section.

2.5 Adaptive sparse grid collocation methods

As stated earlier, in the standard sparse grid approach, all the stochastic dimensions are treated equally. By treated equally, we mean that the number of grid points in each direction is equal. In most physical problems that one deals with, there usually exists some structure (additive, nearly-additive, anisotropic, discontinuous) that can be taken advantage of, to reduce the number of function evaluations. However, the specific kind of structure that the particular solution exhibits is not known a priori. Thus one must construct an approach that automatically detects which dimensions require more nodal points.

The basic proposition of the adaptive sparse grid collocation method is to assess the stochastic dimensions differently, according to the error of interpolation in that dimension. We closely follow the dimension adaptive quadrature approach developed by Gerstner and Griebel [51] and further developed by Klimke [54]. The reason all dimensions are sampled equally in the standard sparse grid method is apparent by revisiting Eq. (2.23). The multi-index $|\mathbf{i}| = i_1 + \ldots + i_N$ that determines the number of sampling points in each dimension i_k is sampled from the simplex $|\mathbf{i}| \leq q$. This ensures that if $(n_1, n_2, \ldots, n_N)$ is a valid index, then $(n_2, n_1, \ldots, n_N)$ is also a valid index and so on. One simple approach to extend the conventional sparse grid to sample differently important dimensions is to consider a weighted simplex $\mathbf{a} \cdot \mathbf{i} \leq q$ (this simple extension is in fact not feasible [51]). Another approach is to allow any general index set satisfying certain conditions. The problem essentially boils down to choosing index sets from the set of conventional sparse grid points. One can heuristically improve the performance of the interpolant in directions where the function is varying rapidly.

2.5.1 Generalized sparse grid construction

The conventional Smolyak algorithm imposes a strict admissibility criterion on the index sets ($|\mathbf{i}| \leq q$). The incorporation of heuristically choosing the most important dimensions/directions/regions can be achieved by relaxing this strict admissibility criterion. The so-called generalized sparse grids [51] are obtained by relaxing this admissibility criteria.

An index set S is called admissible if for all indices $\mathbf{k} \in$ S [51]

$$\mathbf{k} - \mathbf{e}_j \in \mathrm{S} \text{ for } 1 \leq j \leq N,\ k_j > 1, \tag{2.31}$$

where $\mathbf{e}_j$ is the j-th unit vector. This means that an admissible set contains for every index $\mathbf{k}$ all indices which have smaller entries than $\mathbf{k}$. The generalized sparse grid includes both the conventional sparse grids as well as the classical product formulae within it. This criterion still ensures the telescopic property of the differential interpolant $\Delta^i = \mathcal{U}^i - \mathcal{U}^{i-1}$. This means that one can construct a better interpolant starting from a coarse interpolant by just sampling on the unique nodes of the finer interpolant, see Eq. (2.23). Denote the space of all admissible indices by $\mathcal{F}$. The generalized sparse grid construction is then [51]

$$\mathcal{A}_S(f) = \sum_{\mathbf{i}\in S} (\Delta^{i_1} \otimes \ldots \otimes \Delta^{i_1})(f), \tag{2.32}$$

for an admissible set $S \in \mathcal{F}$. By carefully constructing the index sets, it is possible to construct polynomials at least as good as the case of the conventional sparse grids.

2.5.2 Interpolation procedure

To construct interpolation polynomials of increasing accuracy by increasing the number of indices, one uses nested sequence of index sets (as in the case of the conventional sparse grid method). The construction starts with the one element index set $\mathbf{1} = (1, \ldots, 1)$. Indices are added successively such that two criteria are satisfied: the resulting index sets all remain admissible and a large reduction in the interpolation error is achieved. To achieve the second criterion, an error estimator has to be defined that quantifies the error reduction. Once a suitable error indicator is determined, the corresponding error indicators are computed in all the stochastic dimensions.

One starts the interpolation construction with the smallest index $\mathbf{1}$ and adds the indices $(2, \ldots, 1), \ldots, (1, \ldots, 2)$. One then obtains an initial set of error indicators. The index set is partitioned into two sets, the active indices $\mathcal{A}$ and the old indices $\mathcal{O}$ [51]. Newly added indices are denoted as active indices. The error indicators of the forward neighbors of active indices have not yet been computed. All other indices are denoted as old indices.

At each step, the forward neighborhood of the index set with the largest error indicator is considered, and the corresponding error indicators computed. The forward neighborhood of an index $\mathbf{i}$ are the N indices $\{\mathbf{i} + \mathbf{e}_j \mid j = 1, \ldots, N\}$. These new sets are added to the active index sets. Then the index set with the largest error indicator is considered and so on. The error indicator is chosen to be the deviation of the computed value of a particular point from its expected point (from the interpolation polynomial built at this level). This is just the differential interpolation operator $\sum \Delta^{i-1}(f)$ (see Eq. (2.23)) i.e. it is the difference between the computed value of the function at an active index and the interpolated value of the function using all the old indices.

In this way, the algorithm adaptively samples the regions of the conventional sparse grid support region where the error is maximized. The following subsection illustrates the effectiveness of this methodology with some sample examples.

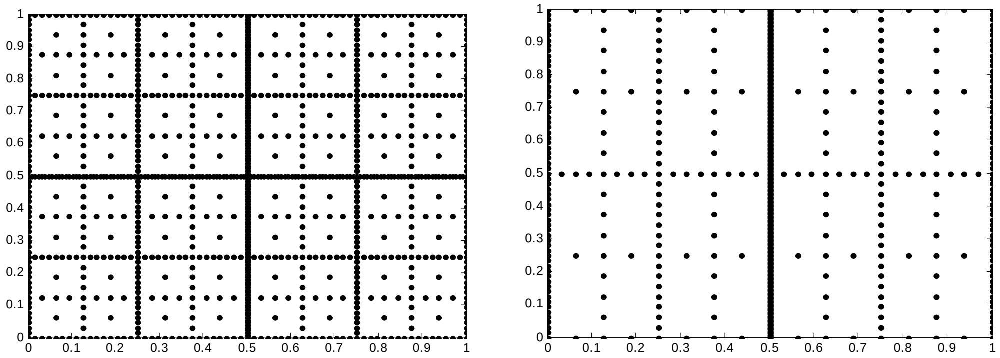

Figure 2.7: The adaptive grid used for $\rho = 1$ (left) and $\rho = 1000$ (right). Notice the increased node points in the y direction for the second case.

2.5.3 Numerical illustrations

Interpolating anisotropic functions

We revisit the first problem in the sparse grid collocation section. Briefly, consider the function $f = e^{-x^2 - \varrho y^2}$, where ϱ is a positive number. This function is analytically smooth. For $\varrho = 1$, the function is isotropically smooth. The computational domain is $[-1, 1] \times [-1, 1]$. We look at the problem for increasing ϱ. As the anisotropy increases the adaptive procedure must sample more points in that direction where the error is maximum (the y direction in this particular case). Fig. 2.7 plots the adaptive grids used for the two particular cases of ϱ. Fig. 2.8 plots the error reduction with the number of support nodes. Compare this with the case of using the conventional sparse grids (Fig. 2.6). The number of nodes required to achieve the same interpolation error of 5×10^{-2} for the case of $\rho = 1000$ is 577 using the adaptive sparse grid method as compared to 1537 using the conventional sparse grid method. As the anisotropy of the problem increases, the adaptive sparse grid method selectively improves the function in the y direction, until the same level of accuracy is reached in both directions.

Interpolating discontinuous functions

We revisit the second problem discussed in the previous section. Briefly, consider a function $f = e^{-x^2 + 2\text{sign}(y)}$ in the domain $[-1, 1] \times [-1, 1]$, where sign is the signum function. The function f has a sharp discontinuity along the $y = 0$ plane. Fig. 2.9 shows the adaptive sparse grid used to compute the interpolation function for this discontinuous function. Notice the large bias towards the y direction, which is to be expected from an adaptive algorithm. Fig. 2.9 also plots

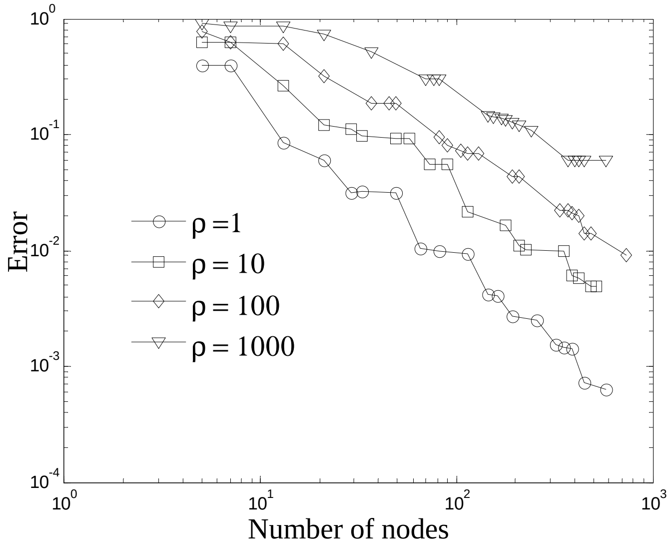

Figure 2.8: Error versus the number of nodes using the adaptive sparse grid method for interpolating anisotropic functions. Compare with the error plot using the conventional sparse grid method shown in Fig. 2.3.

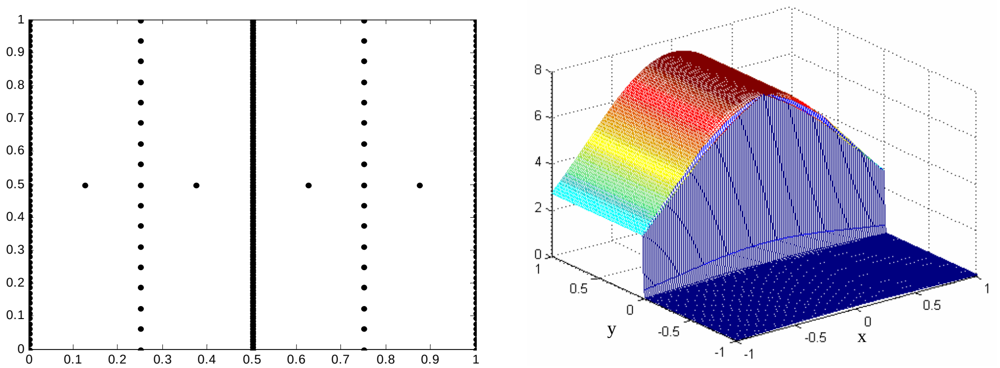

Figure 2.9: Left: Adaptive mesh for the discontinuous problem, Right: Interpolated discontinuous functions.

the interpolated function. The error after using just 553 nodal points is 1×10^{-1}. To achieve the same level of error using the conventional sparse grid method (see Fig. 2.5) 3300 points have to be sampled.

The adaptive sparse grid collocation strategy at worst samples as many points as the conventional sparse grid collocation strategy. This is for problems where every stochastic dimension is equally important. In most physical problems encountered, the solutions exhibit some level of dissimilarity along various directions or have some structure that can be easily exploited using the adaptive sparse grid collocation method. Furthermore, there is very little overhead in computing the error indicator function (since the error indicators are just the incremental interpolation function at the new indices (Eqn. 2.22), [54])

2.6 Ingredients for an adaptive sparse grid collocation implementation

In this section, we outline an approach to perform stochastic analysis of partial differential equations by non-intrusively using an existing deterministic code. The solution procedure can be broadly divided into three distinct operations:

- A subroutine for computing deterministic solutions.
- A subroutine for building the interpolation functions.
- A subroutine for computing moments and other post-processing operations.

2.6.1 Deterministic code

The concept of the collocation method lies in effectively decoupling the physical domain computation from the computations in the stochastic dimensions. The deterministic codes used in the present work took in as input, the sparse grid coordinates. For example, consider the case of two stochastic dimensions (ξ_1, ξ_2), that determine the input random process ω. The range of (ξ_1, ξ_2) is assumed to be $[0,\ 1] \times [0,\ 1]$ without loss of generality. The deterministic executable must be able to take in the different sampled two-tuples (ξ_1^i, ξ_2^i) and output logically named result files R_i*.out*.

2.6.2 Interpolation functions

In the present work, we use a simple MATLAB wrapper program that first initializes the stochastic dimensions and constructs the sparse grid coordinates. In the case of the conventional sparse grid collocation method, all the sampled nodes are known a priori. Hence in this case, the deterministic code is run and the appropriately named result files are available. The wrapper program then reads the input data and constructs the interpolation function. For the rapid construction of the interpolation functions, we utilize the sparse grid interpolation toolbox developed by Klimle [57, 58]. In the case of the adaptive sparse grid collocation method, the wrapper program builds the input files for the deterministic code, calls the executable of the deterministic program and reads in the corresponding result at each step of the process.

2.6.3 Post-processing

Postprocessing usually involves computing the moments of the stochastic solution across the whole domain. This is essentially a cubature of the interpolating function across the stochastic space. In the case of conventional sparse grid collocation, the integration is very straightforward because the weights corresponding to the known nodal positions are computed a priori. A data set containing the weights for each nodal position, for different dimensions and different interpolation depths was first created. Then the cubature over the stochastic space for simultaneously computing moments of various fields becomes simple scalar-matrix products. In the case of the adaptive sparse grid collocation method, the number of collocation points is not known a priori and hence the weights for each point are computed on the fly. That is at each level (or if a particular error tolerance has been reached), the interpolation functions are numerically integrated to get the corresponding weights associated with each nodal point. This results in significantly larger post processing time for higher-dimensional integrations.

2.7 Numerical examples

In this section, we showcase the collocation based strategy to solving stochastic natural convection problems. In all the examples discussed in this work, we construct the interpolation functions based on Clenshaw-Curtis points [54]. The Clenshaw-Curtis type grid has been shown to outperform other types of grids in numerical tests [53, 54]. In all the numerical examples, the global error computed is the maximum of the absolute variation of the interpolated value from the actual value at the newly computed sparse grid points ($\sup_i(\Delta^i)$). That is, at each level, the function is evaluated at some points. The error is defined as the difference between the interpolated value (using the interpolation function at the previous level) and the actual function value at these points. The global error reported is the maximum of these errors.

The main focus of this work is to investigate the effects of input uncertainties in natural convection problems. Consider a d-dimensional bounded domain $D \subset R^d$ with a boundary $\partial D_d \bigcup \partial D_n$. Dirichlet boundary conditions are applied on ∂D_d, while Neumann boundary conditions are applied on ∂D_n. Natural convection sets in due to the thermal differential maintained across ∂D_d. Consider also a complete probability space $(\Omega, \mathcal{F}, \mathcal{P})$, where Ω is the event space, $\mathcal{F} \subset 2^\Omega$ the σ-algebra, and $\mathcal{P} : \mathcal{F} \to [0, 1]$ is the probability measure. In the problems that we consider, the input uncertainties occur due to the following random fields $f(\boldsymbol{x}, \omega)$:

- Variations in the Dirichlet boundary conditions: $\theta(\boldsymbol{x}) = f_1(\boldsymbol{x}, \omega)$, where $\boldsymbol{x} \in \partial D_d$ and $\omega \in \Omega$.
- Variations in the boundary topology (roughness): $\partial D_d = f_2(\boldsymbol{x}, \omega)$, where $\boldsymbol{x} \in \partial D_d$ and $\omega \in \Omega$.
- Variations in material properties (viscosity, porosity): $\varrho(\boldsymbol{x}) = f_3(\boldsymbol{x}, \omega)$,where $\boldsymbol{x} \in D$ and $\omega \in \Omega$.

Under these conditions the problem is to find stochastic functions that describe the velocity $\boldsymbol{u} \equiv \boldsymbol{u}(\boldsymbol{x}, t, \omega) : D \times [0, T] \times \Omega \to R^d$, the pressure $p \equiv p(\boldsymbol{x}, t, \omega) : D \times [0, T] \times \Omega \to R$ and the temperature $\theta \equiv \theta(\boldsymbol{x}, t, \omega) : D \times [0, T] \times \Omega \to R$, such that for $\mathcal{P}$ – almost everywhere $\omega \in \Omega$, the following equations are satisfied:

$$\nabla \cdot \boldsymbol{u} = 0, \tag{2.33}$$

$$\frac{\partial \boldsymbol{u}}{\partial t} + \boldsymbol{u} \cdot \nabla \boldsymbol{u} = -\nabla p + Pr \nabla^2 \boldsymbol{u} + F(\boldsymbol{u}, \theta), \tag{2.34}$$

$$\frac{\partial \theta}{\partial t} + \boldsymbol{u} \cdot \nabla \theta = \nabla^2 \theta, \tag{2.35}$$

where $F(\boldsymbol{u}, \theta)$ is the forcing function in the Navier-Stokes equations and Pr is the Prandtl number of the fluid. In the problems considered later, $F(\boldsymbol{u}, \theta)$ will usually be the Bousinnessq approximated buoyant force term $-RaPr\theta\boldsymbol{e}_g$, where Ra is the thermal Rayleigh number and $\boldsymbol{e}_g$ is the gravity vector.

2.7.1 Natural convection with random boundary conditions

In the following example, a natural convection problem in a square domain $[-0.5, 0.5] \times [-0.5, 0.5]$ is considered. The schematic of the problem is shown in Fig. 2.10. The left wall is maintained at a higher temperature of 0.5. The right wall is maintained at a lower mean temperature of -0.5. The temperature at different points on the right hand side boundary is correlated. This is physically feasible through, say, a resistance heater, where the mean temperature remains constant, but material variations cause local fluctuations from this mean temperature. We assume this correlation to be a simple exponential correlation function, $C(y_1, y_2) = \exp(-c \cdot |y_1 - y_2|)$. Here, c is the inverse of the correlation length that is taken as 1. For ease of analysis, we consider a non-dimensionalized form of the governing equations. The Prandtl number is set to 1.0 and the thermal Rayleigh number is set to 5000. The upper and lower boundaries are thermally insulated. No slip boundary conditions are enforced on all four walls.

Following the solution procedure in [7], the Karhunen-Loève expansion of the exponential correlation for the input uncertainty is performed. Truncating the infinite dimensional representation of the boundary temperature to a finite dimensional approximation gives

$$T(y, \boldsymbol{\xi}) = -0.5 + \sum_{i=0}^{M} \xi_i \sqrt{\lambda_i} f_i(y), \tag{2.36}$$

where ξ_i are normally distributed ($N(0, 1)$). The eigenvalues of the correlation function decay very rapidly. The two largest eigenvalues contribute to 95% of

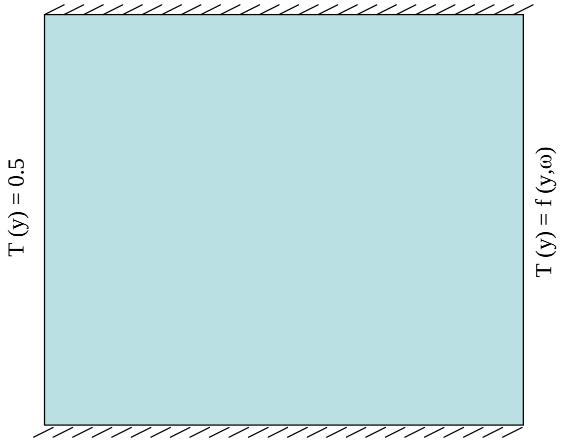

Figure 2.10: Schematic of a natural convection problem with random boundary temperature conditions.

the energy of the spectrum. To showcase the sparse grid collocation method, three cases, where the Karhunen-Loève expansion is truncated at 2, 4 and 8 terms, are considered.

The physical domain is discretized into 50 × 50 uniform quadrilateral elements. Each deterministic simulation is performed until steady-state is reached. This was around 600 time steps with a time interval of $\Delta t = 1 \times 10^{-3}$.

Convergence with increasing number of nodes

Fig. 2.11 plots the variation in the error with increasing number of support points for both the conventional isotropic sparse grid and the adaptive sparse grid methods. In the case of the isotropic sparse grid method, the level of interpolation is increased linearly for the three problems of dimensions 2, 4 and 8, respectively. For the two-dimensional case, the adaptive sparse grid collocation (ASGC) is marginally better than the conventional sparse grid collocation (CSGC) technique. The same level of accuracy is achieved in 137 function eval-

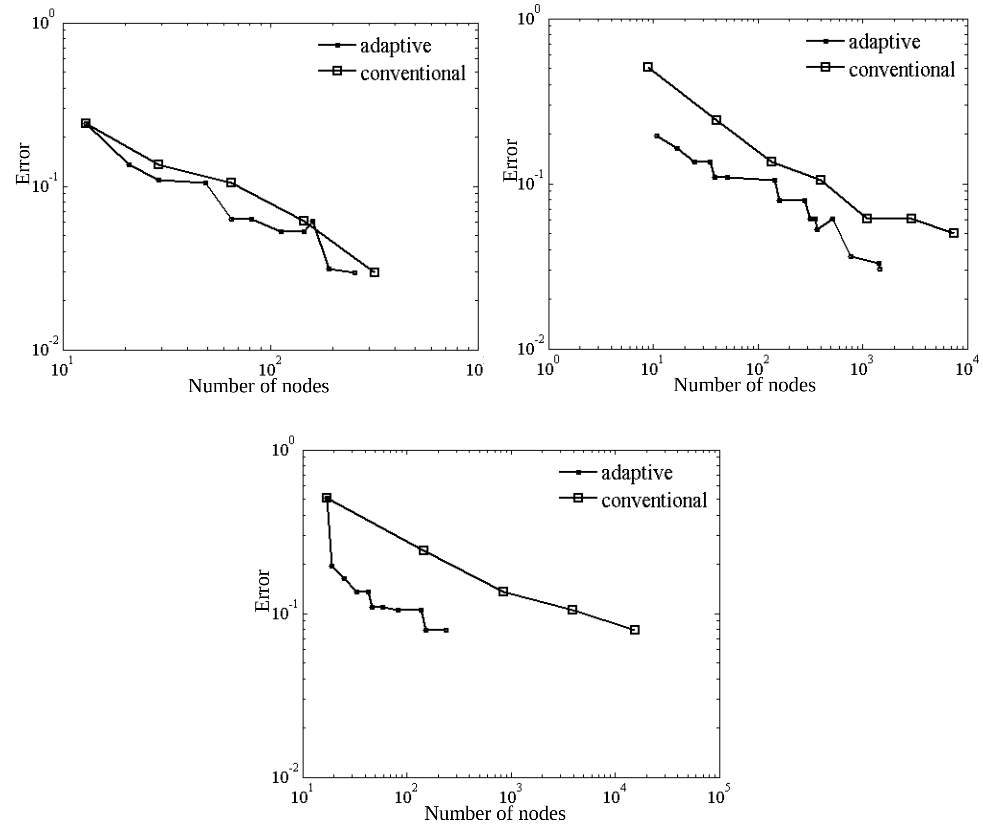

Figure 2.11: Error reduction with increased number of support nodes for 2, 4 (top figures) and 8 (bottom figure) dimensions.

uations as compared to the 321 required in the CSGC method. As the number of stochastic dimensions is increased, the ASGC method provides orders of magnitude reduction in the number of functional evaluations. For the same magnitude of error ($\sim 4 \times 10^{-2}$), in 4 dimensions the ASGC required 751 function evaluations compared to the 7537 that the CSGC required (see Fig. 2.11). This is illustrated clearly in the case of 8 stochastic dimensions where a 65 times reduction in the number of function evaluation is seen going from the CSGC to ASCG methods (15713 to 241). What has to be noted is that this dramatic reduction in the number of functional evaluations is mainly due to the structure of the solution. While the adaptive strategy neglects the last four dimensions and quickly converges to an accurate solution, the isotropic sparse grid method

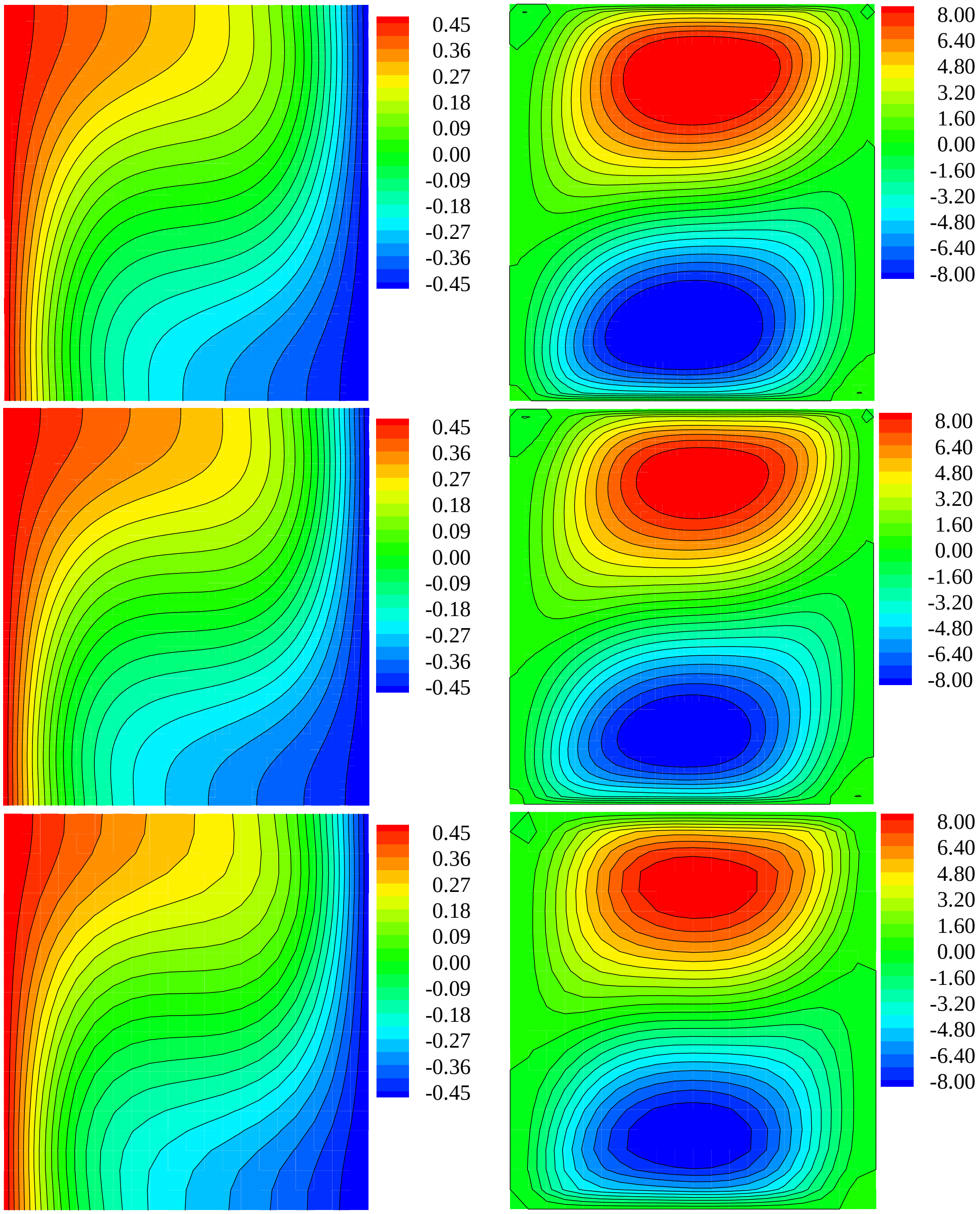

Figure 2.12: Mean Temperature and u velocity contours from different solution strategies. Top row: A level 6 collocation method, Middle row: Monte-Carlo sampling over 65000 points, Bottom row: Second-order GPCE expansion.

takes many more functional evaluations to do the same because it treats all dimensions equally. As the number of dimensions (i.e more terms in the KL expansion are taken into account) increases, the isotropic method treats these dimensions equally, even though the higher dimension have a negligible effect on the stochastic solution. On the other hand, the adaptive method takes this structure into account and preferentially samples the dimensions with the larger eigen values.

Comparison with Monte-Carlo simulations and GPCE

In the case of the conventional sparse grid collocation method for the problem truncated to two-dimensions, a level 6 interpolation scheme was used in the sparse grid interpolation method. This resulted in solving the deterministic problem at 321 different realizations. In the case of the adaptive sparse grid collocation method, 137 realizations were required. The sparse grid points correspond to the Clenshaw-Curtis cubature points in two-dimensions. The solution procedure is embarrassingly parallel. The complete simulation was performed independently on 16 nodes (32 processors) of the $V3$ cluster at the Cornell Theory Center. The total simulation time was about 8 minutes. To compare the results with other available methods, we performed Monte-Carlo simulations of the same process. 65000 samples from the two-dimensional phase space were generated. A second order polynomial chaos expansion of the above problem was also performed. The mean and standard deviation values of the three methodologies match very closely as seen in Fig. 2.12 and Fig. 2.13, respectively. The total computational time for the GPCE problem was 235 minutes. Table. 1 shows representative times for the natural convection problem solved

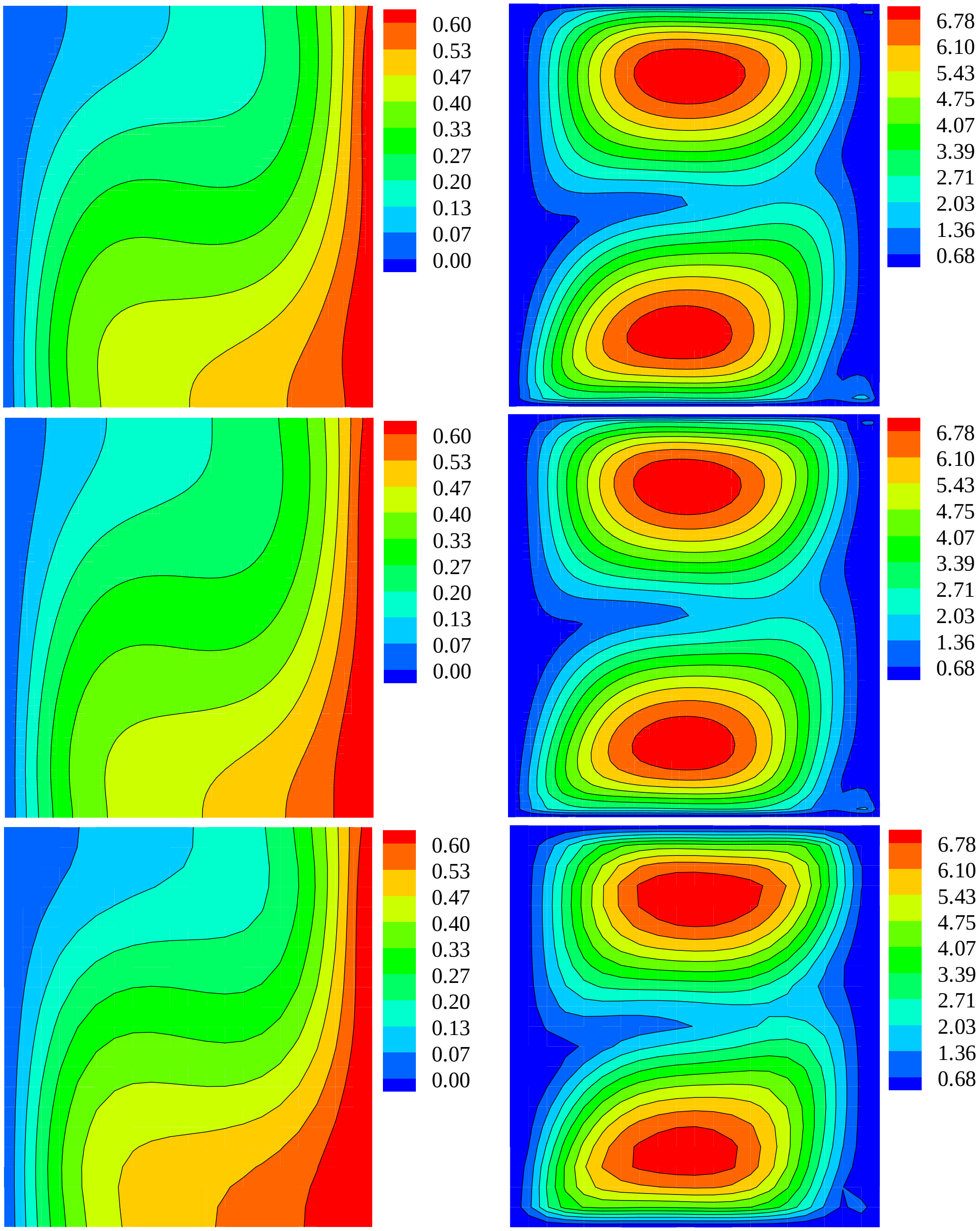

Figure 2.13: Standard deviation of Temperature and u velocity contours from different solution strategies. Top row: A level 6 collocation method, Middle row: Monte-Carlo sampling over 65000 points, Bottom row: Second-order GPCE expansion.

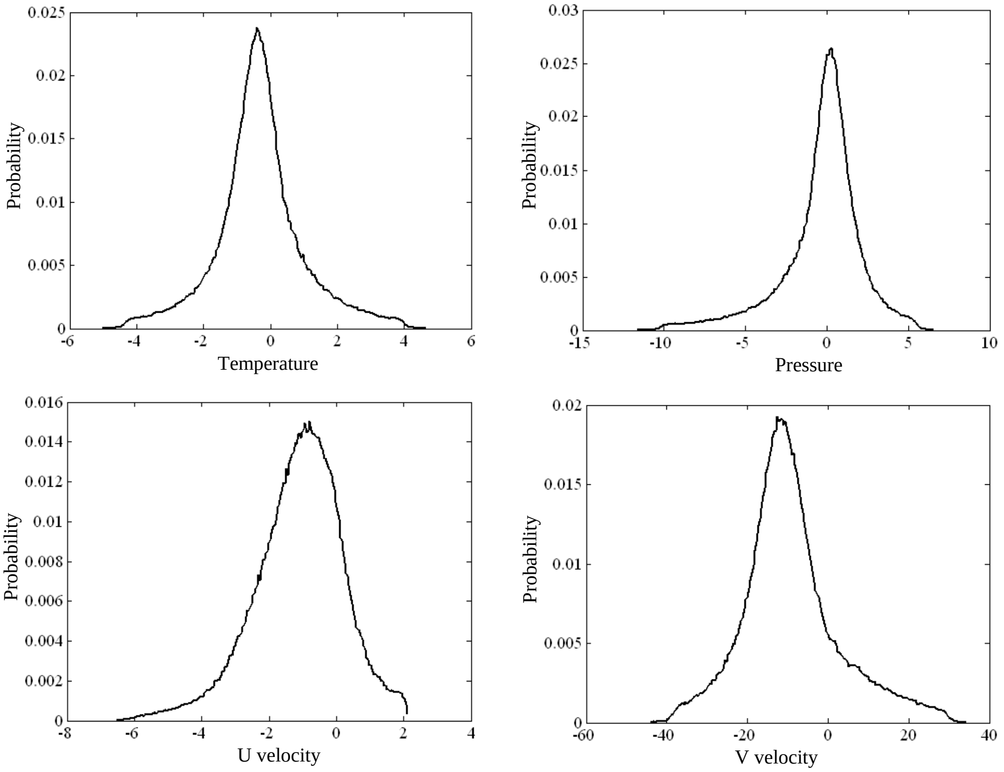

Figure 2.14: Probability distribution functions for the dependent variables at point (0.34, 0). Top row: Temperature and pressure, Bottom row: u and v velocity components.

Table 2.1: Solution times (minutes)

N (stochastic dims)	GPCE	Conventional SC	Adaptive SC
2	235	8	3.4
4	5340	187	19
8	1585	391	8

using GPCE and collocation based methods. The dimension 2 and 4 problems were solved using a second-order polynomial chaos representation, while the problem in 8 dimensions was solved using a first-order polynomial chaos representation. All problems were solved on 16 nodes (32 processors) of the $V3$ cluster at the Cornell Theory Center. Notice that as the number of dimensions increases, the performance of the collocation method improves.

Higher-order moments and PDFs

Once the interpolant has been constructed, it is relatively straightforward to extract higher-order statistics from the stochastic solution. The effect of the uncertain boundary conditions is to change the convection patterns in the domain. At the extreme ranges, the direction of the convective roll actually reverses. It is informative to look at the probability distribution of the velocity at the points of high standard deviation. This provides a clue towards the existence of equilibrium jumps and discontinuities in the field. The point (0.34, 0.0) is one such point of high-deviation (see Fig. 2.13). The velocity at that point was sampled randomly 500000 times from the 2 dimensional stochastic space and the corresponding PDF from its histogram distribution was computed. The probability distribution functions for the temperature, pressure and velocities at this spatial point are plotted in Fig. 2.14. The applied random temperature boundary conditions results in some realizations having temperatures (along the right wall) both higher and lower than the left wall. This leads to instances where there is a complete reversal in the direction of circulation. Furthermore, as seen from Fig. 2.12, most of the flow in the horizontal direction is concentrated in two regions. Consequently, the u velocity in these regions experiences a large variation due to the imposed boundary conditions. This results in the tailing of the u velocity distribution seen in PDF for u velocity in Fig. 2.14. Since pressure can be considered to enter the physics as a means of imposing continuity, the PDF for the pressure also exhibits a similar tailing.

2.7.2 Natural convection with random boundary topology

In the previous problem, we modelled the uncertainty due to the randomness in the boundary conditions. In the present problem, we investigate the effects of surface roughness on the thermal evolution of the fluid heated from below. The surface of any material is usually characterized broadly into two aspects: waviness and roughness. Waviness refers to the large scale fluctuations in the surface. Roughness is the small scale perturbations of the surface. Roughness is described by two components: the probability of the point being z above/below the datum (PDF), and the correlation between two points on the surface (ACF). The type of surface treatment that resulted in the surface can be directly concluded from the auto-correlation function. For example, if the surface has been shot-peened, its ACF would have a larger correlation distance that if the surface had been milled. Usually the PDF of the position of a particular point is well represented by a Gaussian like distribution. To a degree, the ACF can be approximated by an exponential correlation kernel with a specified correlation length. Surface roughness has been shown to play an important role in many systems, particularly those involving turbulent flow [60]. A recent work of Tartakovsky and Xiu [61] deals with this problem in a spectral stochastic framework.

A natural convection problem in a rectangular domain $[-1.0, 1.0] \times [-0.5, 0.5]$ is considered. The schematic of the problem is shown in Fig. 2.15. The upper wall is smooth while the lower wall is rough. The ACF of the surface roughness of the lower wall is approximated to be an exponential function. The correlation length is set to 0.10. The mean roughness (absolute average deviation from a smooth surface) is taken to be $\frac{1}{100}^{th}$ of the characteristic length ($L = 1.0$). The first eight eigenvalues are considered to completely represent the surface random-

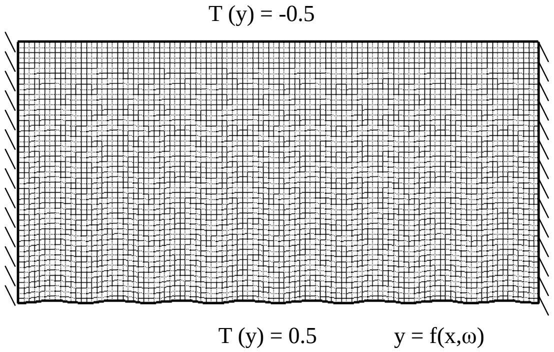

Figure 2.15: Schematic of natural convection with random boundary topology (surface roughness).

ness. The problem is solved in eight dimensional stochastic space. The bottom wall is maintained at a higher temperature of 0.5. The top wall is maintained at a lower temperature of -0.5. The side walls are thermally insulated. The Prandtl number is set to 6.4 (corresponding to water) and the thermal Rayleigh number is set to 5000. No slip boundary conditions are enforced on all four walls.

The physical domain is discretized into 100×50 uniform quadrilateral elements. Each deterministic simulation is performed until steady-state is reached. This was around 400 time steps with a time interval of $\Delta t = 1 \times 10^{-2}$.

Each deterministic simulation represents one realization of the random (rough) lower wall sampled at different $\boldsymbol{\xi} = (\xi_1, .., \xi_8)$. The lower wall is characterized by the truncated KL expansion, $y(x) = \sum_{i=1}^{8} \sqrt{\lambda_i}\xi_i f_i(x)$, where λ_i and $f_i(x)$ are the eigenvalues and eigenvectors of the ACF. A reference domain ($[-1.0, 1.0] \times [-0.5, 0.5]$) and grid ($100 \times 50$ uniform quadrilateral elements) are considered and the nodes on the bottom boundary are transformed according to the above formula to get each realization of the random boundary. The Jacobian of the transformation from the reference grid to the new grid can be easily computed (It is just the ratio of the elemental areas before and after the transfor-

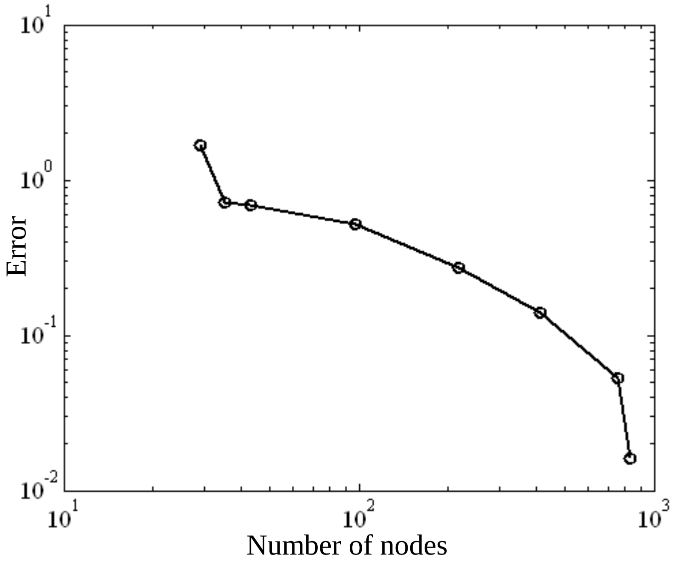

Figure 2.16: Error reduction using the adaptive sparse grid methodology.

mation). The deterministic solutions at each collocation point in stochastic space is computed on the reference grid. This allows the subsequent computation of the ensemble averages naturally.

In the case of the conventional sparse grid collocation method, a level 4 sparse interpolation grid was utilized for discretizing the stochastic space. 3937 collocation points were used to discretize the eight dimensional stochastic space using the conventional sparse grid collocation method (CSCG) while the adaptive sparse grid collocation method (ASGC) method required 820 realizations to construct the interpolation function. 8 nodes on the Velocity-3 cluster at the Cornell Theory Center took 500 minutes for simulating the problem at all the collocation points. Fig. 2.16 plots the reduction in the error with the number of nodal supports used.

Fig. 2.17 shows some sample realizations of the temperature and velocity contours. The first row of figures is the case when the roughness is minimal. The temperature and velocity contours closely resemble those of Rayleigh-Bénard

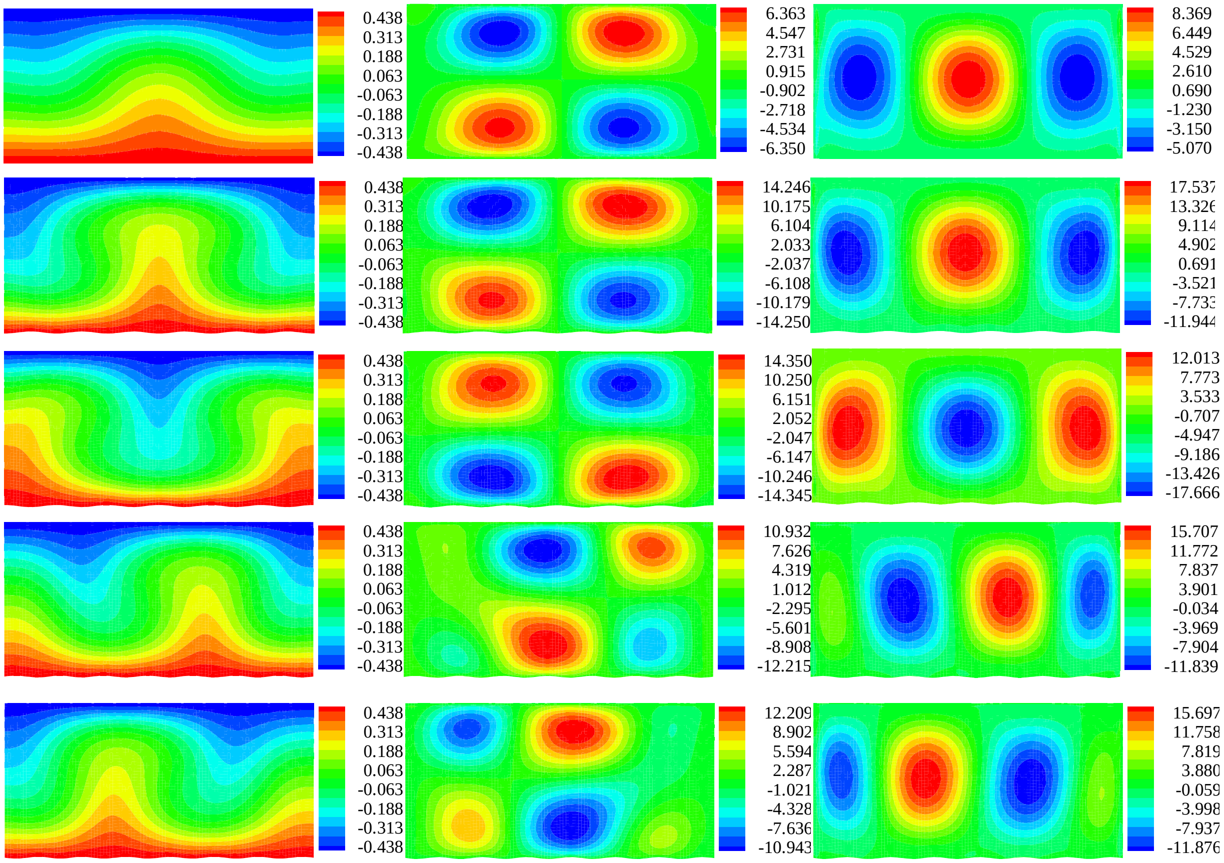

Figure 2.17: Realizations of the problem: Temperature, u velocity and v velocity components.

convection with smooth boundaries. The next 4 rows of figures show extremal values of the surface roughness. The thermal plume changes position according to the local surface geometry. Also note that the flow field has been substantially enhanced due to roughness. Experiments have shown that surface roughness results in the emission of thermal plumes (at high Rayleigh number) and generally causes enhanced heat transport and improved flow circulation [60].

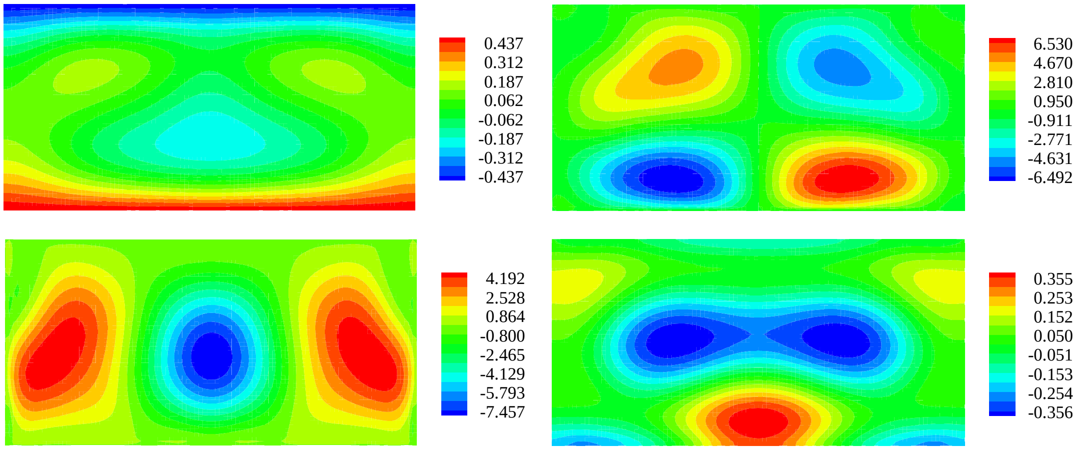

Figure 2.18: Mean values of the variables: Top left: Temperature, Top right: u velocity component, Bottom left: v velocity component, Bottom right: pressure.

Moments and probability distribution functions

Fig. 2.18 plots the mean values of the temperature, velocity and pressure. The rough lower surface causes the mean temperature to be much more homogenized. The mean velocity is larger than the case with smooth lower surface. In the case of smooth lower surfaces, the u velocity shows symmetry about the horizontal centerline. Notice that this is lost when the lower surface is made rough. The rougher surface enhances the circulation patterns in the lower half of the system. Fig. 2.19 plots the mean velocity vectors and some streamline contours. The top corners of the system consist of recirculating rolls which result in reduced heat transfer at the edges as can be seen in the mean temperature contour plot.

Fig. 2.20 plots the second moment of the temperature, velocity and pressure variables. The standard deviation of the velocity is of the order of the mean velocity. This suggests that there are multiple modes at which the system exists

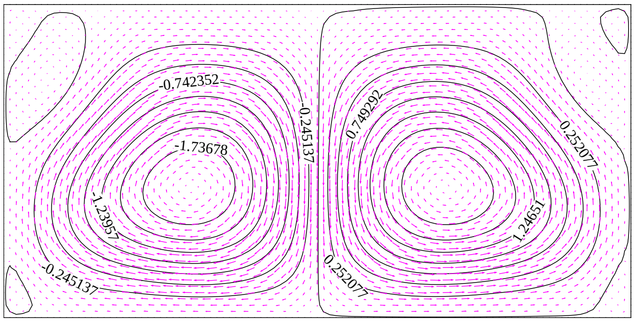

Figure 2.19: Mean velocity vectors and streamlines.

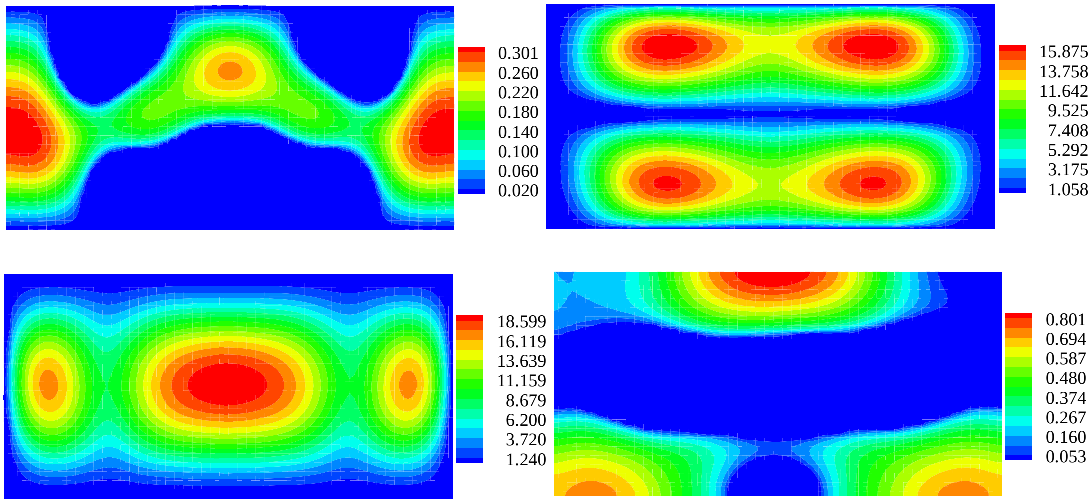

Figure 2.20: Standard deviation of the variables: Top left: Temperature, Top right: u velocity component, Bottom left: v velocity component, Bottom right: pressure.

and the variation of the random variables across the stochastic space causes the system to move from one stable state to another. If the state changes abruptly as the random variable moves across a threshold value, a mode shift is said to have occurred. The existence of multiple patterns in the region of parameters considered here is well known [62].

Mode shifts and equilibrium jumps

One way to identify multiplicity of stable states is through visualizing the probability distribution functions of the dependent variables at a physically relevant point. Small changes in the roughness causes the central thermal plume in the case of smooth surface Rayleigh-Bénard instability to change positions. This can cause reversal of the direction of the fluid flow in parts of the domain (compare rows 2 and 3 in Fig. 2.17). We choose one such point, $(0, 0.25)$ which has a large deviation in the temperature to plot the PDFs. The PDFs were computed from 500000 Monte-Carlo realizations of the dependent variables. Fig. 2.21 plots the corresponding distribution functions. Notice that there exist two peaks in the distribution functions for the temperature pressure and the v velocity. This confirms the existence of two stable states. We assert that these shifts also occur due to the non-linearities introduced by the surface roughness. To verify if this is indeed the case, Fig. 2.22 shows the temperature and v velocity variations at a specific point ($[0.0, 0.25]$, chosen because of its large temperature and v velocity second moment) plotted over the first two random variables. Notice the abrupt jump in the temperature and v velocity as the random variables cross 0. Fig. 2.23 shows the projection of the variation onto a single dimension. The mode shift is apparent in the abrupt change of the dependent variables as the random variable crosses over zero.

Below the critical Rayleigh number

As an extension to the previous problem, we investigate the possible mode shifts from a conduction based state to a convection based (Rayleigh-Bénard flow) thermal pattern caused by the effect of surface roughness. A sub-critical

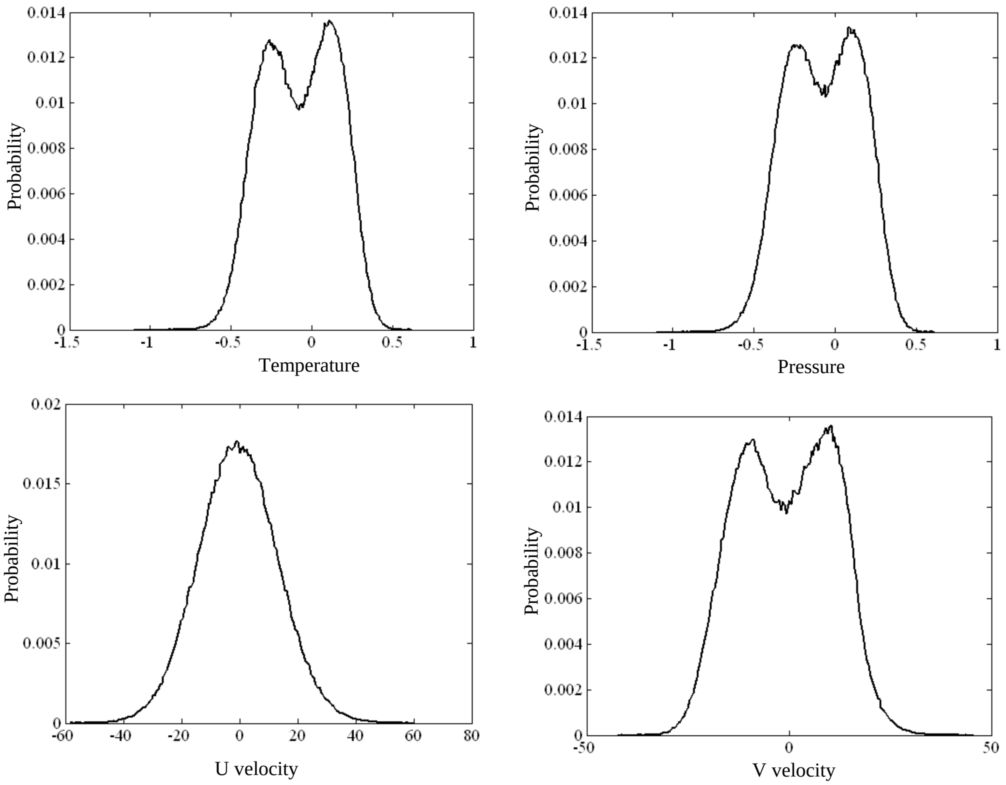

Figure 2.21: Probability distribution functions for the dependent variables at point $(0.25, 0)$. Top row: Temperature and pressure, Bottom row: u and v velocity components.

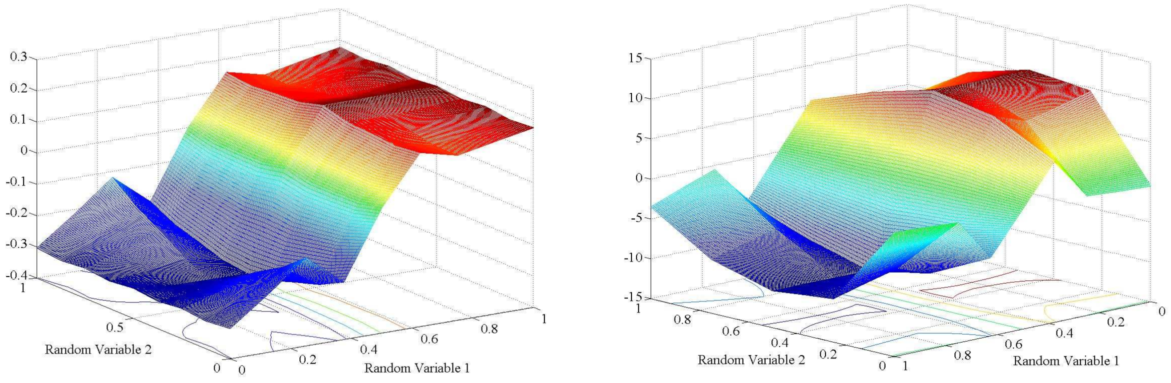

Figure 2.22: Mode shift: Left: Temperature, Right: v velocity component.

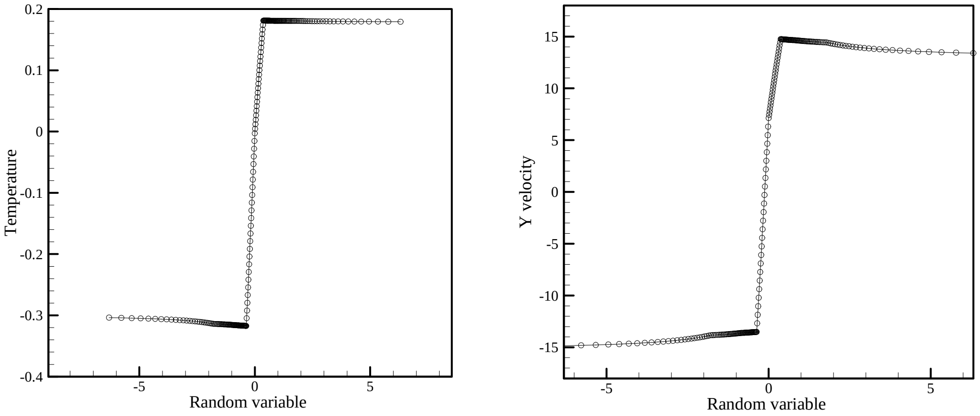

Figure 2.23: Mode shift: Left: Temperature, Right: v velocity component.

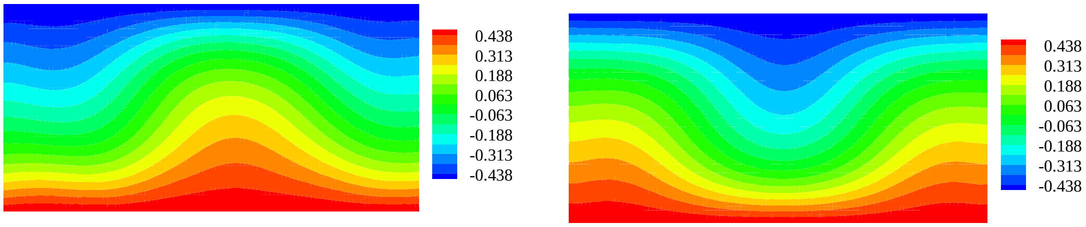

Figure 2.24: Extreme realizations of temperature.

Rayleigh number of 1700 is chosen. This is just below the critical Rayleigh number of 1708. The other system and domain specifications are the same as the previous problem. We study the problem in four stochastic dimensions.

The critical Rayleigh number of 1708 is computed for a infinitely long, flat layer of fluid. The variations in the lower surface coupled with the fact that we are in fact only considering a finite sized domain causes the onset of convection in some of the stochastic space. Fig. 2.24 shows two such extreme realizations of temperature at two different collocation points. Notice that the two patterns almost mirror images of each other. But the behavior of the mean temperature is along expected lines. Fig. 2.25 plots the mean and the standard deviation of the temperature contours. The temperature evolution is predominantly conductive.

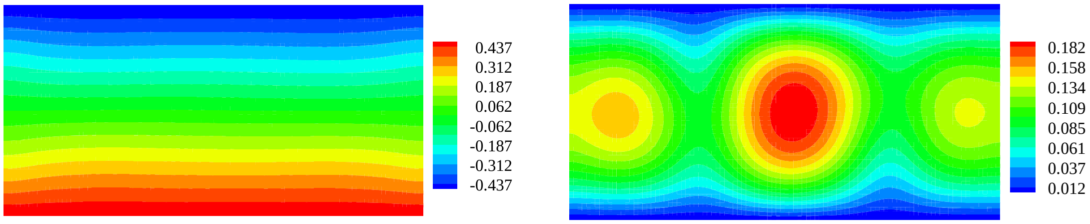

Figure 2.25: Mean and standard deviations of temperature.

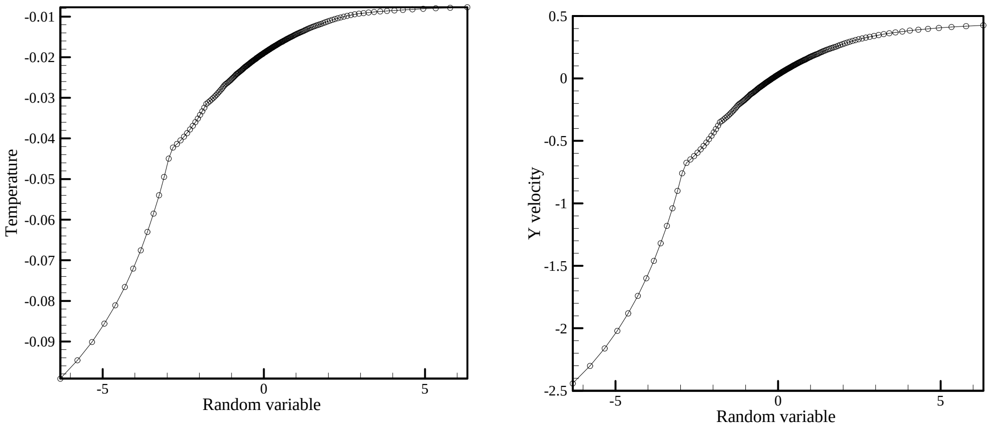

Figure 2.26: Mode shift: Left: Temperature, Right: v velocity component.

To further verify that no mode shift occurs as the stochastic phase space is sampled, Fig. 2.26 plots the projection of the temperature and y velocity variations onto one dimension at a specific point ($[0.0, 0.0]$). The v velocity variation is smooth with small gradients (compare with Fig. 2.23) while the temperature variation is negligible.

2.7.3 Natural convection with random boundary topology: Large dimensions

In the previous problem, we concentrated on qualitatively predicting mode shifts caused due to surface roughness of the lower wall in a Rayleigh-Bénard

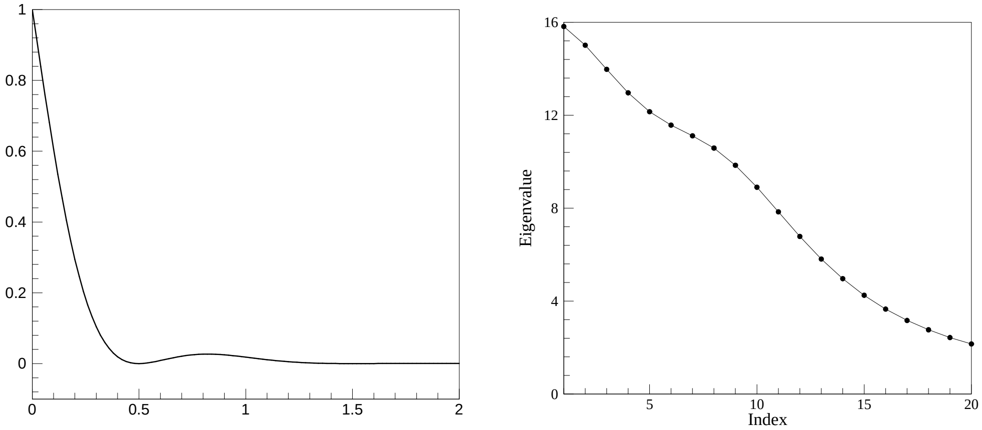

Figure 2.27: Left: ACF of the surface roughness, Right: Eigen-spectrum of the correlation.

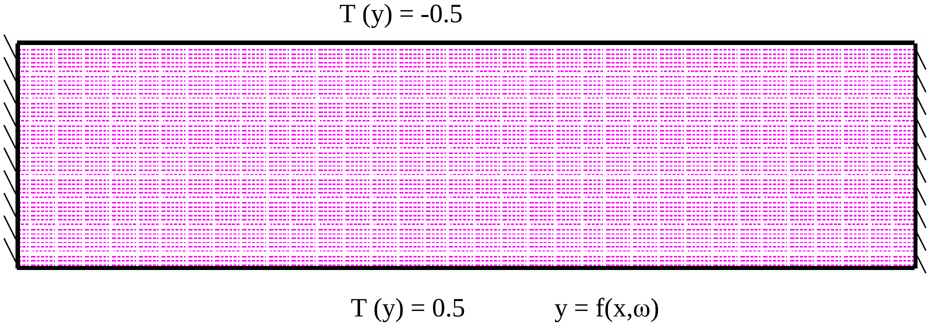

Figure 2.28: Schematic of natural convection with wall surface roughness computed from experiments.

type simulation. To represent the surface roughness, the ACF was considered to be an exponential function. In this problem, we consider realistic ACF from experimental data. The surface roughness correlation function is given in Fig. 2.27 (taken from [72]). The corresponding eigen-spectrum is given in Fig. 2.27. The first 20 eigenvalues correspond > 99% of the spectrum.

A natural convection problem in an enlarged rectangular domain $[-2.0, 2.0] \times [-0.5, 0.5]$ is considered. The schematic of the problem is shown in Fig. 2.28.

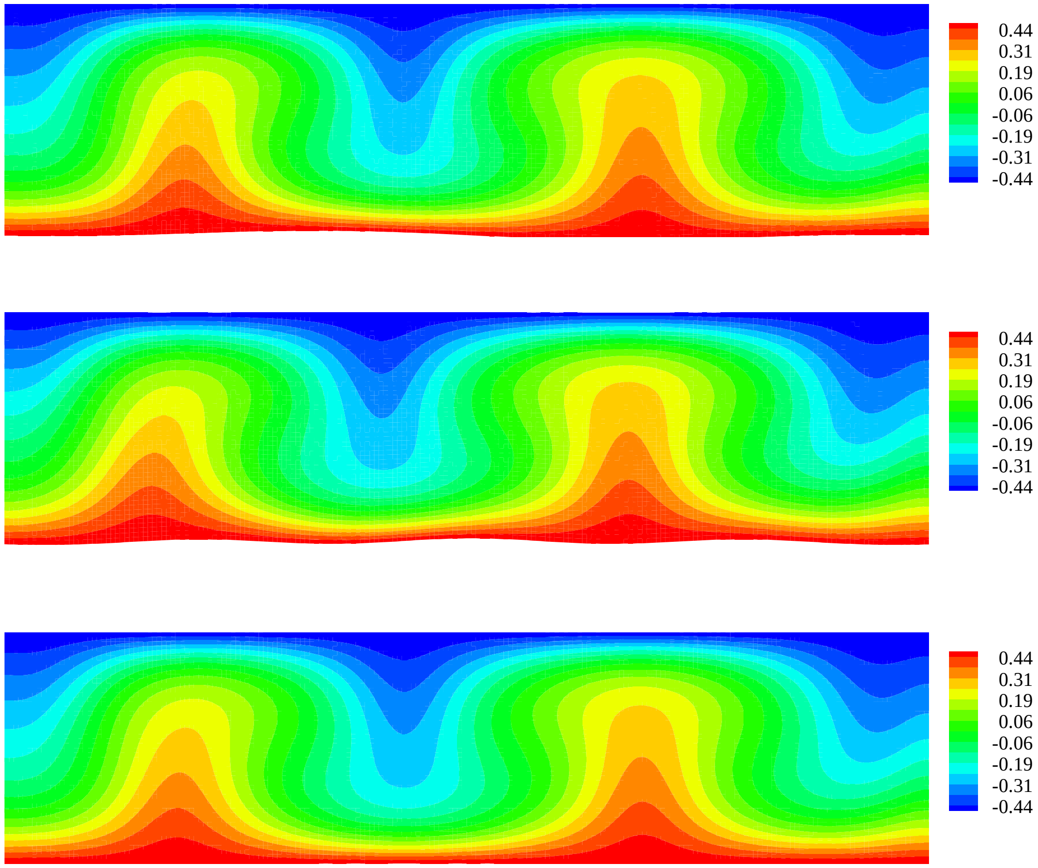

Figure 2.29: Realizations of temperature.

The upper wall is smooth while the lower wall is rough. The mean roughness (absolute average deviation from a smooth surface) is taken to be $\frac{1}{200}^{th}$ of the characteristic length ($L = 1.0$). The first twenty eigenvalues are considered to completely represent the surface randomness. The bottom wall is maintained at a higher temperature of 0.5. The top wall is maintained at a lower temperature of -0.5. The side walls are thermally insulated. The Prandtl number is set to 6.4 (corresponding to water) and the thermal Rayleigh number is set to 10000. No slip boundary conditions are enforced on all four walls.

A level 3 interpolatory sparse grid is considered in 20 dimensional stochastic space. This corresponds to 11561 collocation points. The complete simulation

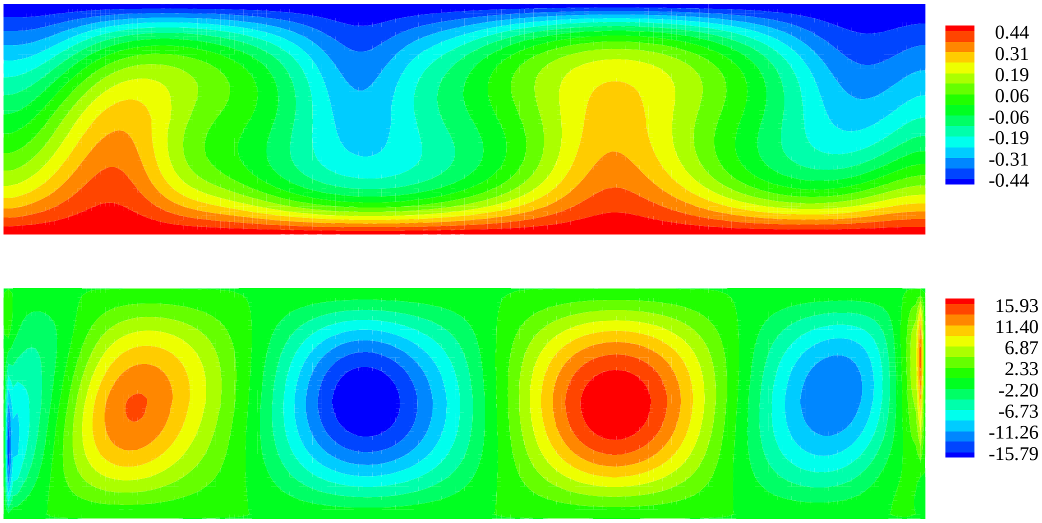

Figure 2.30: Mean values of temperature and *v* velocity component.

took about 1400 minutes on 48 nodes of the Velocity-3 cluster at the Cornell Theory Center. Fig. 2.29 shows temperature contours at some of the collocation points in 20 dimensional stochastic space. Fig. 2.30 shows the mean values of the temperature and the *v* velocity. Fig. 2.31 plots the mean velocity vectors and some streamlines. The standard deviations of the temperature and the *v* velocity are shown in Fig. 2.32. Notice that the surface roughness causes thermal plumes to form, which are seen in the variations in the temperature and the *v* velocity. These plumes caused by the non-uniformities in the lower surface result in improved heat transfer across the domain. This concept can be further extended to the design of the ACF of the surface roughness to achieve enhanced heat transfer characteristics. This will showcased in one of our forthcoming publications.

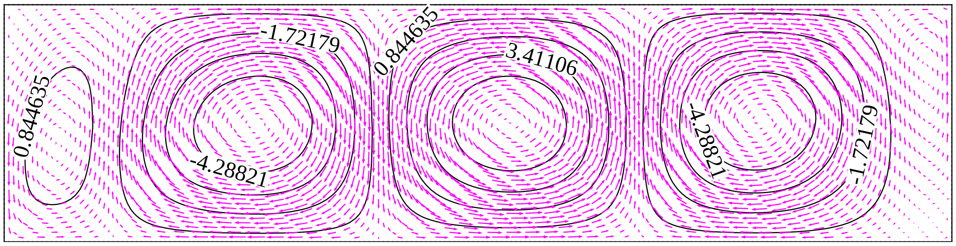

Figure 2.31: Mean velocity vectors and streamlines.

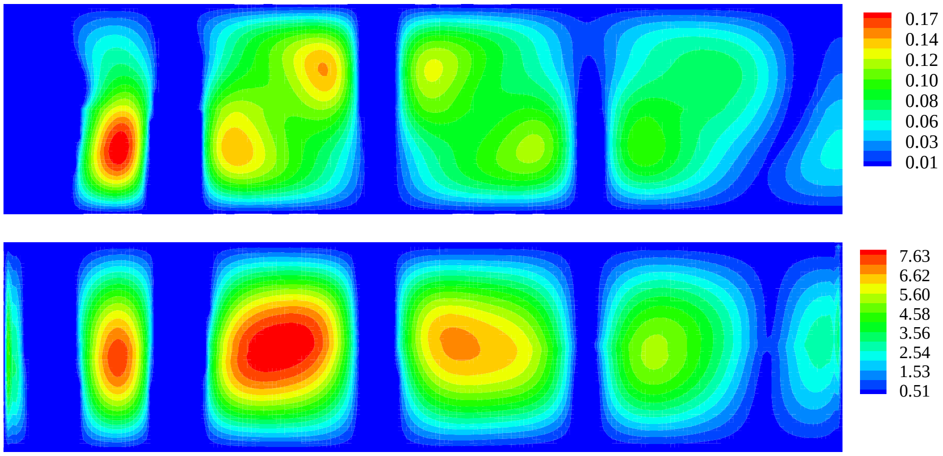

Figure 2.32: Standard deviations of temperature and v velocity component.

2.7.4 Convection in heterogeneous porous media

Fluid flow through porous media is an ubiquitous process occurring in various scales ranging from the large scale :- geothermal energy systems, oil recovery, to much smaller scales :- flow of liquid metal through dendritic growth in alloy solidification and flow through fluidized beds. The analysis of flow through a medium with deterministic variable porosity has been well studied [63]. But in most cases of heterogeneous porous media, the porosity either varies across multiple length scales or cannot be represented deterministically. In the following example, we focus on the case when the porosity is described as a random

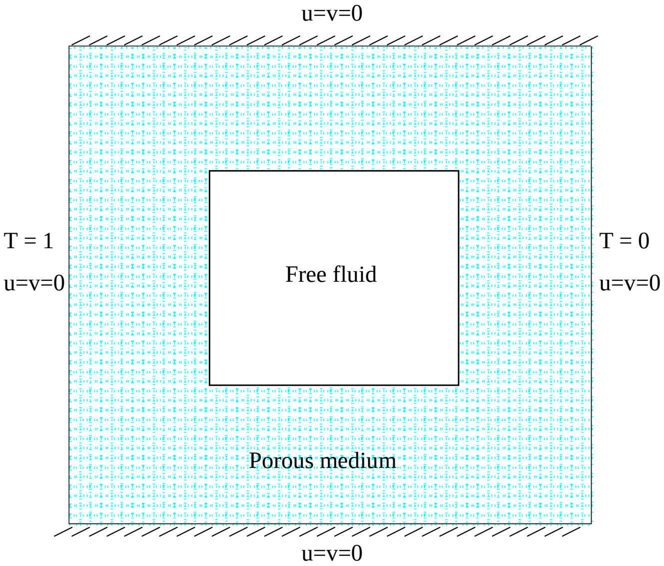

Figure 2.33: Schematic of convection in a medium with random porosity.

field. The usual descriptor of the porosity is its correlation function and the mean porosity.

A schematic of the problem is shown in Fig. 2.33. This problem has been investigated by Nithiarasu et al. [63]. A square domain of dimensions $[-0.5, 0.5] \times [-0.5, 0.5]$ is considered. The inner half of the square is considered to be free fluid. The rest of the domain is filled with a porous material. The porous material is assumed to be Fontainebleau sandstone, whose experimental correlation function is taken from [64]. The correlation function and a cross-sectional image of the sandstone is shown in Fig. 2.34.

The governing equation for the fluid flow in the variable porosity medium is given by (see Nithiarasu et. al[63] and Samanta and Zabaras [65]):

$$\begin{aligned}\frac{\partial v}{\partial t} + v \cdot \nabla(\frac{v}{\epsilon}) = -\frac{Pr}{Da}\frac{(1-\epsilon)^2}{\epsilon^2}v \quad &- \quad \frac{1.75 \parallel v \parallel (1-\epsilon)}{(150Da)^{1/2}\epsilon^2}v + Pr\nabla^2 v - \\ \epsilon\nabla p \quad &- \quad \epsilon PrRaT\mathbf{e}_g \qquad (2.37)\end{aligned}$$

where ϵ is the volume fraction of the fluid and Da is the Darcy number. Nat-

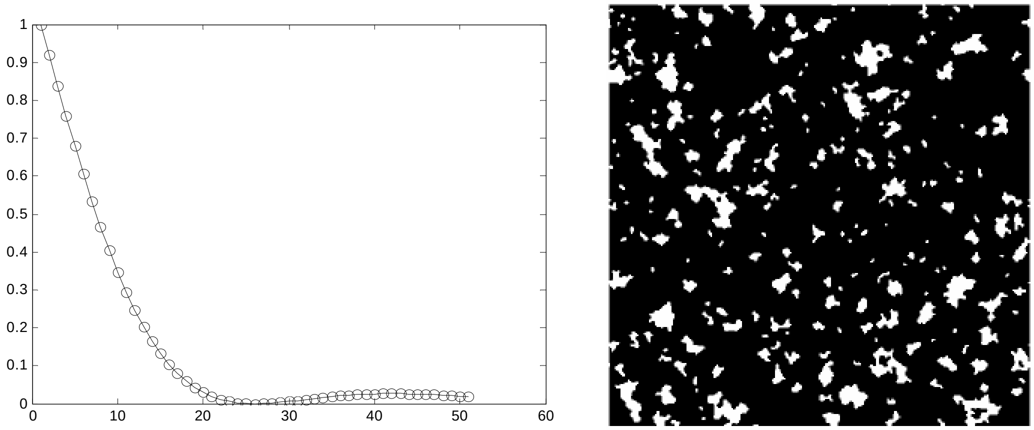

Figure 2.34: Fontainebleau sandstone: Correlation function and cross-sectional image.

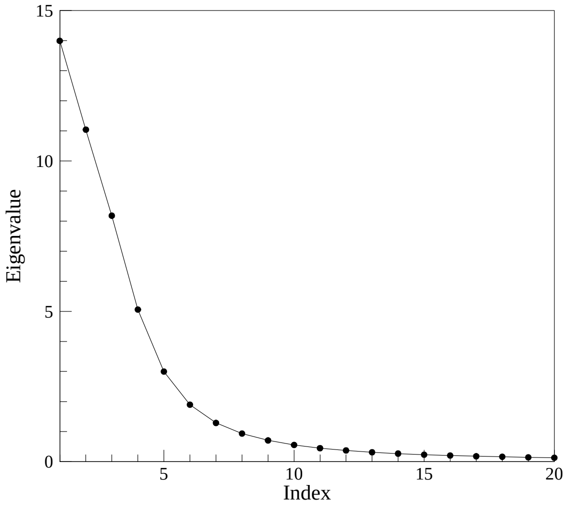

Figure 2.35: Eigen spectrum of the correlation kernel.

ural convection in the system is considered. The left wall is maintained at a dimension-less temperature 1.0, while the right wall is maintained at 0.0. The other walls are insulated. No slip conditions are enforced on all four walls. The Rayleigh number is 10000 and the wall Darcy number is 1.185×10^{-7}. The wall porosity is $\epsilon = 0.8$ and the porosity of the free fluid in the interior of the domain is 1.0.

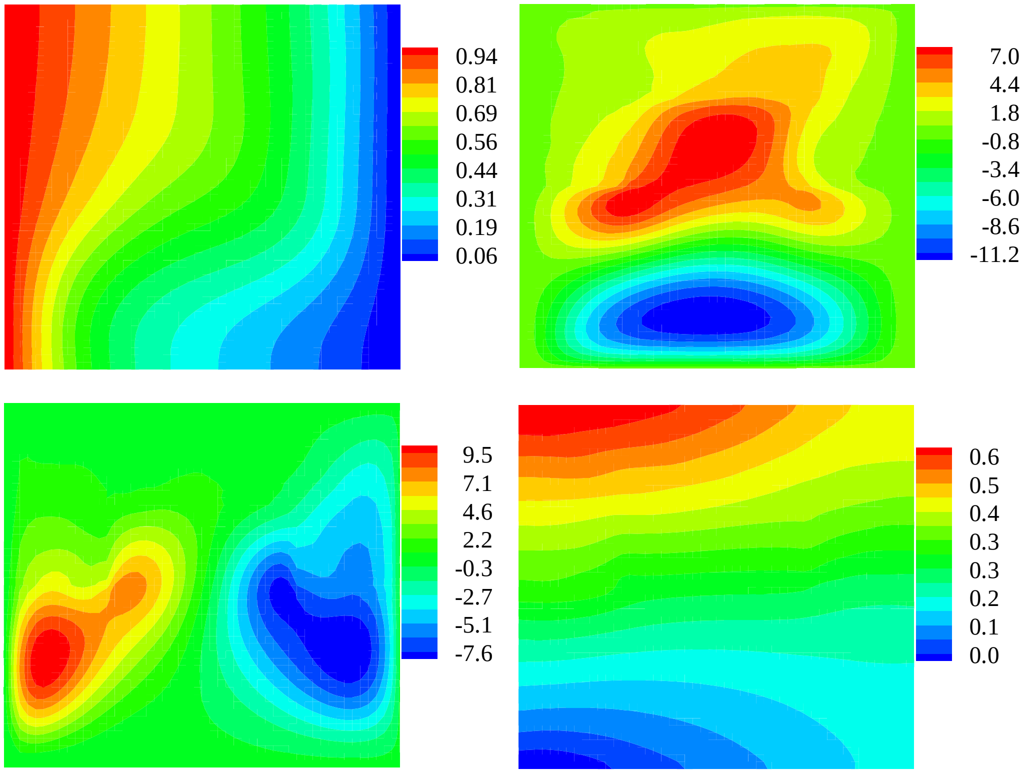

Figure 2.36: Mean values of the variables: Top left: Temperature, Top right: u velocity component, Bottom left: v velocity component, Bottom right: pressure.

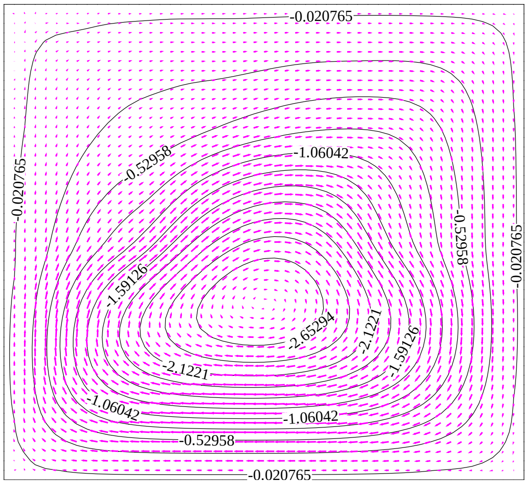

Figure 2.37: Mean velocity vectors and streamlines.

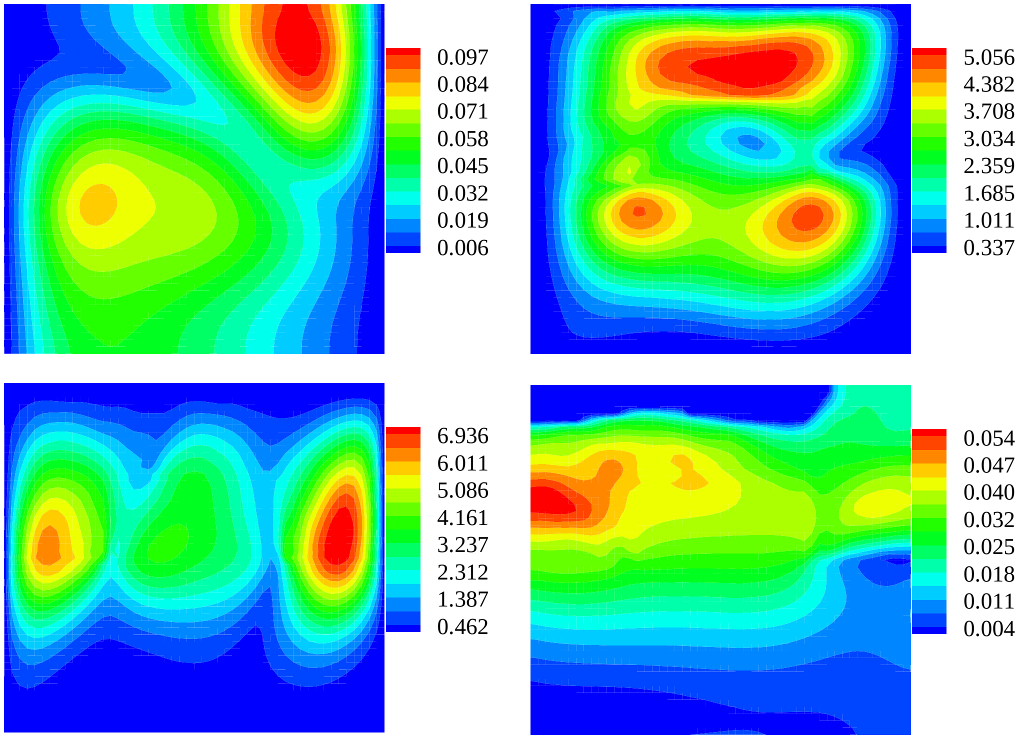

Figure 2.38: Standard deviation of the variables: Top left: Temperature, Top right: u velocity component, Bottom left: v velocity component, Bottom right: pressure.

The numerically computed eigenvalues of the correlation are shown in Fig. 2.34. The first eight eigenvalues correspond to 94% of the spectrum. We consider the porosity to described in a 8 dimensional stochastic space. The mean porosity is 0.8. A level 4 interpolatory sparse grid with 3937 collocation points was utilized for the stochastic simulation. A fractional time step method based on the work of Nithiarasu et al. [63] is used in the simulation of the deterministic problem. Fig. 2.36 plots the mean temperature, velocity and pressure contours. Fig. 2.37 shows the mean velocity vectors and some streamlines. The standard deviation of the dependent variables is shown in Fig. 2.38.

2.8 Conclusions

The generalized polynomial chaos approach and its derivatives have been extensively utilized to solve thermal and fluid flow problems involving random inputs and boundary conditions. The GPCE is restrictive in the sense that it becomes computationally infeasible to solve problems involving lareg number of expansion terms due to the coupled nature of the governing equations.In this context collocation based approaches are considered. We have attempted to provide a natural development of collocation based approaches starting from the drawbacks of the spectral stochastic methodology. We show that this leads naturally to the tensor product collocation method [15] and the sparse grid collocation method [16]. An extension of the sparse grid collocation method to adaptively sample regions/dimensions of high function variations is presented. The methodology can also efficiently detect additive and nearly additive structures in the solution. The adaptive sparse grid collocation methodology provides at least an order of magnitude improvement in the number of function evaluations required to construct comparable interpolation functions as compared to the conventional sparse grid method. The collocation methodology results in the solution of completely decoupled deterministic problems. The embarrassingly parallel nature of these problems is exploited to construct fast and efficient solution strategies to problems in high stochastic dimensions.

Using the adaptive sparse grid collocation method, it is relatively straightforward to convert any deterministic code into a code that solves the corresponding stochastic problem. We provide a detailed road-map, description of the necessary changes in the deterministic code and the required sub-routines for pre- and post-processing to easily accomplish this change.

We have attempted to showcase the utility of the sparse grid collocation method to solve large stochastic dimensional heat transfer problems. We have solved realistic natural convection problems in rough surfaces with stochastic dimensions up to $d = 20$ as well as natural convection problems through heterogeneous porous media. We further looked at the shifts in equilibrium that occur due to slight variations in the boundary conditions and successfully captured these equilibrium jumps.

CHAPTER 3

DATA-DRIVEN APPROACHES TO CONSTRUCTING STOCHASTIC INPUT MODELS

3.1 Representing input randomness

The first step towards solving Eq. (2.1) is some form of numerical representation of the input random processes. A finite dimensional representation of the abstract probability space is a necessary prerequisite for developing any viable framework to solve Eq. (2.1). In this chapter, we discuss various techniques that can be utilized to represent the input uncertainties, with an emphasis on utilizing experimental data to construct these representations. Note that the input parameters to Eq. (2.1) can be either be scalars or functions.

3.1.1 Input parameters as random variables

Consider the case when the input parameter, α is a scalar. The problem of interest is now to represent the uncertainty of α in a numerically feasible way that utilizes experimental data. Experimental data, in this case, refers to a set of realizations of α, $\{\alpha_1, \ldots, \alpha_M\}$. The most straightforward, intuitive way to represent this variability is to construct a histogram of the variability and associate a random variable, ξ_α, with a PDF proportional to the histogram. Thus, each input parameter is represented using a random variable. The governing stochastic differential equation now becomes

$$\mathcal{B}(\boldsymbol{u}, p, \theta : \boldsymbol{x}, t, \xi_\alpha) = 0, \tag{3.1}$$

where ξ_α is the random variable which represents the variability in the input parameter α. In case there are multiple (uncertain) scalar parameters $\{q, \alpha\}$, each of these input parameters should be represented as appropriate random variables $\{\xi_q, \xi_\alpha\}$. Assume that there are $n = 2$ scalar input parameters, the governing stochastic differential equation now becomes

$$\mathcal{B}(\boldsymbol{u}, p, \theta : \boldsymbol{x}, t, \xi_q, \xi_\alpha) = 0. \tag{3.2}$$

Thus, from a deterministic dependant variable, θ, defined in *nsd*+1 (*nsd* space dimensions and 1 dimension representing time) dimensions, we now have to solve for the stochastic dependant variable, θ, defined in $nsd + 1 + n$ (*nsd* space dimensions, 1 dimension representing time and *n* stochastic dimensions representing the variability in the input parameters)

3.1.2 Random field as a collection of random variables

In some cases, the input parameters are functions showing variability in space. This could be, for instance, imposed boundary conditions or property variability in heterogeneous media. Assume (for clarity), that $q(\boldsymbol{x})$ is one such input parameter that is uncertain. One simple way of representing the uncertainty of this spatially varying random process (also called a random field) is to consider $q(\boldsymbol{x})$ as a collection of scalar values at different spatial locations. That is, the function $q(\boldsymbol{x})$ is approximated as a collection of points $q' = \{q(\boldsymbol{x}_1), q(\boldsymbol{x}_2), \ldots, q(\boldsymbol{x}_k)\}$. Each of these individual parameters $q(\boldsymbol{x}_i)$ show some uncertainty and hence can be represented as appropriate random variables. Note that the representation of the random field $q(\boldsymbol{x}),\ \boldsymbol{x} \in \mathcal{D}$ as a vector of points $q' = \{q(\boldsymbol{x}_1), q(\boldsymbol{x}_2), \ldots, q(\boldsymbol{x}_k)\}$ is an approximation that is equivalent to $q(\boldsymbol{x})$ in the limit as $k \to \infty$. For some finite value of k, the above procedure of approximating a random field as a set of independent random variables results in a $nsd + 1 + k$ dimensional stochastic differential equation for the evolution of the dependent variable θ. The governing stochastic differential equation is written as:

$$\mathcal{B}(\boldsymbol{u}, p, \theta : \boldsymbol{x}, t, \xi_{q^1}, \ldots, \xi_{q^k}) = 0. \tag{3.3}$$

One problem with the above strategy is that the number of random variables (the stochastic dimensionality) quickly becomes very large and can pose significant computational problems.

3.1.3 The Karhunen-Loève expansion

An alternate approach to representing random fields is to recognize that such fields usually have some amount of spatial correlation. There is rich literature on techniques to extract/fit correlations for these random fields from input experimental/numerical data. This is an area of intense ongoing research [19]. The assumption of the existence of some correlation structure of the random field provides a elegant way of representing the random field as a finite set of uncorrelated random variables. This technique is called the Karhunen-Loève expansion.

The Karhunen-Loève expansion is essentially founded on the idea that the space of all second-order random processes (i.e. processes with a finite second moment) can be defined as a Hilbert space equipped with the mean-square norm. Denote this Hilbert space as $L_2(\Omega, \mathcal{F}, \mathcal{P})$. Since this space is complete, any random process $q(\boldsymbol{x}, \omega) \in L_2(\Omega, \mathcal{F}, \mathcal{P})$ can be expressed as a summation

$$q(\boldsymbol{x}, \omega) = \sum_{i=1}^{\infty} q_i(\boldsymbol{x})\zeta_i(\omega), \tag{3.4}$$

where $\{\zeta_i(\omega)\}_{i=0}^{\infty}$ forms a basis of the space and $\{q_i\}_{i=0}^{\infty}$ are the projections of the field onto the basis. Eq. (3.4) involves an infinite summation and hence is computationally intractable. The Karhunen-Loève expansion (KLE) considers finite-dimensional subspaces of $L_2(\Omega, \mathcal{F}, \mathcal{P})$ that best represent the uncertainty in $q(\boldsymbol{x}, \omega)$. The KLE for a stochastic process $q(\boldsymbol{x}, t, \omega)$ is based on the spectral decomposition of its covariance function $R_{hh}(y_1, y_2)$. Here, y_1 and y_2 denote the spatio-temporal coordinates $(\boldsymbol{x}_1, t_1)$ and $(\boldsymbol{x}_2, t_2)$, respectively. By definition, the covariance function is symmetric and positive definite and has real positive eigenvalues. Further, all its eigenfunctions are orthogonal and span the space to which $q(\boldsymbol{x}, t, \omega)$ belongs. The KL expansion can be written as

$$q(\boldsymbol{x}, t, \omega) = E(q(\boldsymbol{x}, t, \omega)) + \sum_{i=0}^{\infty} \sqrt{\lambda_i} f_i(\boldsymbol{x}, t)\xi_i(\omega), \tag{3.5}$$

where $E(q(\boldsymbol{x}, t, \omega))$ denotes the mean of the process and $\{\xi_i(\omega)\}_{i=0}^{\infty}$ forms a set of uncorrelated random variables whose distribution has to be determined [18]. $(\lambda_i,\, f_i(\boldsymbol{x}, t))_{i=0}^{\infty}$ form the eigenpairs of the covariance function:

$$\int_{\mathcal{D}\times\mathcal{T}} R_{hh}(y_1, y_2) f_i(y_2) dy_2 = \lambda f_1(y_1). \tag{3.6}$$

The chief characteristic of the KLE is that the spatio-temporal randomness has been decomposed into a set of deterministic functions multiplying random variables. These deterministic functions can also be thought of as representing the scales of fluctuations of the process. The KLE is mean-square convergent to the original process $q(\boldsymbol{x}, t, \omega)$. More interestingly, the first few terms of this expansion represents most of the process with arbitrary accuracy. The expansion in Eq. (5.5) is typically truncated to a finite number of summation terms, k. Using this technique, the representation becomes

$$\mathcal{B}(\boldsymbol{u}, p, \theta : \boldsymbol{x}, t, \xi_{q^1}, \ldots, \xi_{q^k}) = 0. \tag{3.7}$$

3.1.4 Model reduction as a tool for constructing input models

In many cases, one can only obtain limited experimental information about the variation in a particular property/conditions that is essential to analyzing a particular system. This is particularly apparent when one is dealing with systems that involve heterogeneous or anisotropic media or forcing conditions. Examples of these systems include (but are not limited to) polycrystalline materials, functionally-graded composites, heterogeneous porous media, multiphase composites, structural materials like cement and mortar. The thermal-mechanical (and chemical) properties of these media/materials depend on the local distribution of materials. In such analysis, the only information that is usually available experimentally to quantify these variations are statistical correlations (like the mean distribution of material, some snapshots of the structure at a few locations or some higher order correlation functions, Fig. 3.1). This leads to an analysis of the problem assuming that the properties are random fields satisfying some experimentally determined statistics. In the context of a computational framework to perform such analysis, one needs to construct a stochastic input model that encodes this limited information.

Physically meaningful/useful solutions can be realized only if property statistics are experimentally obtained and used in generating the stochastic model. Usually, experimental data regarding statistics and correlations of the property (or microstructure) are known (in the following, for the sake of con-

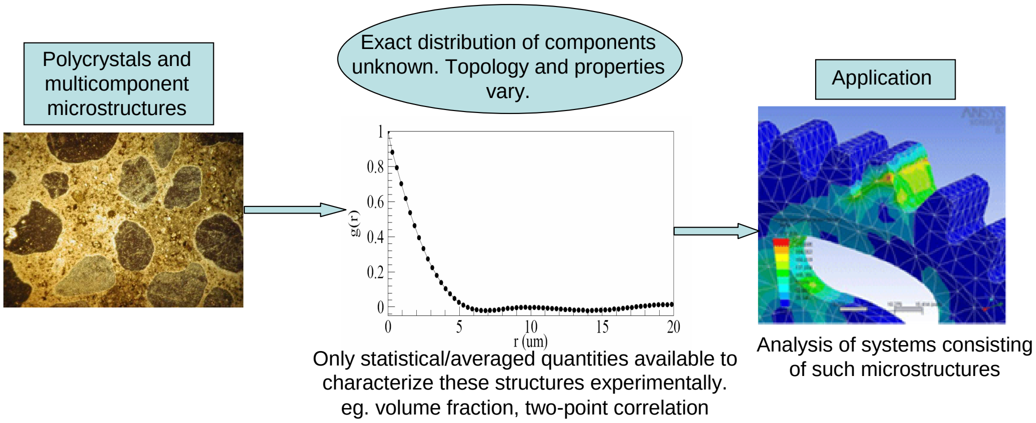

Figure 3.1: Limited information about important input quantities necessitates construction of stochastic input models

sistency, we will use microstructure and property interchangeably). There may be infinitely many microstructures (or property maps) that satisfy these relations. Consequently, any of these microstructures are equally probable to be the microstructure under consideration. Hence we have to consider the variation of the properties (resulting from the possible variation in topology/microstructures) as a random field. The first step to including the effect of these random fields is to estimate a reliable descriptor of the same. For this descriptor to be useful in a computational framework, it must be a finite-dimensional function. The objective is then to construct low-dimensional functions that approximate this property variation. By sampling over this approximate space, we are essentially sampling over all possible, plausible microstructures (or any other property variations).

In our recent work in this area [20], a general framework to construct a low-dimensional stochastic model to describe the variation in spatially varying quantities (based on limited statistical information) was developed. The methodology relies on a limited number of snapshots of possible property maps (or microstructures). These snapshots are either experimentally obtained or reconstructed using the experimental statistical information available. A model reduction scheme (based on Principle Component Analysis (PCA)) was formulated to represent this set of snapshots/property maps (which is a large-dimensional space) as a low-dimensional approximation of the space. A *subspace reduction strategy* (see [20]) based on constraints that enforce the experimental statistics was used to construct the smallest low-dimensional representation of the variability. This basic idea is illustrated using the example of polycrystalline materials (this general concept can be applied to *any* property variation) in Fig. 3.1 using a trivial two-dimensional model. The image on the left shows a reduced-order model (the plane) that captures the variation in polycrystalline microstructures that satisfy an experimentally determined grain boundary distribution [20]. Each point on the linear manifold shown corresponds to a microstructure with a unique grain distribution. By sampling over this space, one essentially samples over the space of all allowable microstructures. The figure on the right shows a similar orientation distribution model. This methodology proved to be extremely effective in analyzing the effect of thermal property variations in two phase microstructures.

Following this, in [21], a more flexible non-linear method to encode the microstructural variability was developed. This framework is based on concepts borrowed from psychology [22, 23], cognitive sciences [24, 25], differential geometry [26, 27, 28] and graph theory [29, 30]. The key mathematical concept on which the framework is constructed on is the so-called principle of 'manifold learning': Given a finite set of unordered data points in high dimensional space, construct a low dimensional parametrization of this dataset. The finite set of unordered data points correspond to various (experimental or reconstructed) plausible realizations of the property map. In [21], we show that this set of unordered points (satisfying some experimental statistics) lies on a manifold embedded in a high dimensional space. That is, all the possible variations of the quantity of interest (*given a limited set of information about its variability, in terms of say, some experimentally determined correlation statistics*) lie on a curve in some high-dimensional space. An isometric transformation of the manifold into a low-dimensional, convex connected set is performed. It is shown that this isometric transformation preserves the underlying geometry of the manifold. The isometric transformation of the manifold is constructed using ideas from graph theory, specifically by generating graph approximations to the geodesic distance on embedded manifolds [21]. Given only a finite amount of information about the property variability, this methodology recovers the geometry of the curve and its corresponding low-dimensional representation. Rigorous error bounds and convergence estimates of this parametric representation of the property variability are constructed [21]. This parametric space serves as an *accurate, low-dimensional, data-driven representation* of the property variation. The framework was shown to work exceedingly well in constructing models of various property variations. This methodology was used to construct low-dimensional input stochastic models of property variations for the analysis of two-phase microstructures [21].

Given limited information about the variability of a spatially varying parameter, the techniques discussed above construct a low dimensional stochastic model, $\mathcal{G}$, representing the variability as:

$$\alpha(\boldsymbol{x}, \omega) = \mathcal{G}(\xi_1, \dots, \xi_k). \tag{3.8}$$

The corresponding governing stochastic differential equation is

$$\mathcal{B}(\boldsymbol{u}, p, \theta : \boldsymbol{x}, t, \xi_{q^1}, \ldots, \xi_{q^k}) = 0. \tag{3.9}$$

We detail the non-linear model reduction strategy in the rest of the chapter:

3.2 Problem definition

The focused application of the developed framework is to analyze transport phenomena in heterogeneous random media. In this work, we are particularly interested in investigating thermal diffusion in two-phase heterogeneous media. In such problems, the topology of the heterogeneous structure (the microstructure) is only known in terms of a few statistical correlations. Denote this set of statistical correlations by $S = \{S_1, \ldots, S_p\}$. Any material structure that satisfies these statistical correlations is a valid realization of the microstructure. Consequently, the microstructural topology should be considered as a random field (satisfying some statistical correlations) and the microstructure in any arbitrary specimen as a realization of this field. The thermal diffusivity of the material obviously depends on the topology of the microstructure. We assume that the thermal diffusivity of the material is uniquely defined by its microstructure (e.g. each point in a realization of a two-phase medium is assumed to be uniquely occupied by one of the two phases (0 or 1) and that each phase has a given diffusivity). That is, for a microstructure specified as a distribution of two phases in a domain, the thermal diffusivity distribution is given by simply replacing the phase description (0 or 1) at each point on the domain by its corresponding thermal diffusivity (α_0 or α_1). From this simple scaling, for each realization of the microstructure, we can compute the corresponding realization of the diffusivity, α ($\alpha = k/\rho C_p$).

Let $\mathcal{M}_S$ be the space of all microstructures that satisfy the statistical properties S. This is our event space. Every point in this space is equiprobable. Consequently, we can define a σ-algebra $\mathcal{G}$ and a corresponding probability measure $\mathcal{P} : \mathcal{G} \rightarrow [0, 1]$ to construct a complete probability space $(\mathcal{M}_S, \mathcal{G}, \mathcal{P})$ of allowable microstructures. Corresponding to a microstructure realization $\omega \in \mathcal{M}_S$, we can associate a thermal diffusivity distribution $\alpha(\boldsymbol{x}, \omega)$. That is, the thermal diffusivity of the random heterogeneous medium is represented as

$$\alpha(\boldsymbol{x}) = \alpha(\boldsymbol{x}, \omega), \quad \boldsymbol{x} \in D, \quad \omega \in \mathcal{M}_S, \tag{3.10}$$

where $D \subset R^{n_{sd}}$ is the n_{sd}-dimensional bounded domain that is associated with this medium. The governing equation for thermal diffusion in this medium can be written as:

$$\frac{\partial u(\boldsymbol{x}, t, \omega)}{\partial t} = \nabla \cdot [\alpha(\boldsymbol{x}, \omega) \nabla u(\boldsymbol{x}, t, \omega)] + f(\boldsymbol{x}, t), \ \boldsymbol{x} \in D, \ t \in [0, T_f], \ \omega \in \mathcal{M}_S, \tag{3.11}$$

where u is the temperature. Here, f is the thermal source/sink and is assumed to be deterministic without loss of generality.

The solution methodology is to first reduce the complexity of the problem by reducing the probability space into a finite-dimensional space [45]. In the present case, the random topology satisfies certain statistical correlation functions $S = \{S_1, \ldots, S_p\}$ (from now on referred to as the 'experimental statistics'). We utilize nonlinear model reduction techniques (see Section 3.3) to decompose the random topology field into a finite set of uncorrelated random variables. Upon decomposition and characterization of the random inputs into d random variables, $\xi_i(\omega)$, $i = 1, \ldots, d$, the solution to the SPDE Eq. (3.11) can be written as

$$u(\boldsymbol{x}, t, \omega) = u(\boldsymbol{x}, t, \boldsymbol{\xi}), \quad \boldsymbol{\xi} = (\xi_1, \ldots, \xi_d), \tag{3.12}$$

where $\boldsymbol{\xi}$ is the d-tuple of the random variables. The domain of definition of $\boldsymbol{\xi}$ is denoted by Γ. Eq. (3.11) can now be written as a $(d + n_{sd})$-dimensional problem as follows:

$$\frac{\partial u(\boldsymbol{x}, t, \boldsymbol{\xi})}{\partial t} = \nabla \cdot [\alpha(\boldsymbol{x}, \boldsymbol{\xi}) \nabla u(\boldsymbol{x}, t, \boldsymbol{\xi})] + f(\boldsymbol{x}, t), \ \boldsymbol{x} \in D, \ t \in [0, T_f], \ \boldsymbol{\xi} \in \Gamma. \tag{3.13}$$

For the sake of brevity, we will denote the system of equations consisting of Eq. (3.13) and appropriate initial and boundary conditions (here for simplicity assumed to be deterministic) as $\mathcal{B}(u : \boldsymbol{x}, t, \boldsymbol{\xi}) = 0$.

We utilize a sparse grid collocation framework (based on the Smolyak algorithm) that results in a set of decoupled deterministic equations [14]. In this collocation approach, a finite element approximation is used for the spatial domain and the multidimensional stochastic space is approximated using interpolating functions. One computes the deterministic solution at various points in the stochastic space and then builds an interpolated function that best approximates the required solution [14]. The collocation method collapses the $(d + n_{sd})$-dimensional problem to solving M (where, M is the number of collocation points, $\boldsymbol{\xi}_k, k = 1, \ldots, M$) deterministic problems in n_{sd}-space dimensions. The q-th order statistics (for $q \geq 1$) of the random solution can be obtained through simple quadrature operations on the interpolated function $u(\boldsymbol{x}, \boldsymbol{\xi}) = \sum_{k=1}^{M} u(\boldsymbol{x}, \boldsymbol{\xi}_k) L_k(\boldsymbol{\xi})$ (where L_k are the sparse grid interpolation functions) as:

$$< u^q(x) >= \sum_{k=1}^{M} u^q(x, \boldsymbol{\xi}_k) \int_{\Gamma} L_k(\boldsymbol{\xi}) \rho(\boldsymbol{\xi}) d\boldsymbol{\xi}, \tag{3.14}$$

where $\rho(\boldsymbol{\xi}) : \Gamma \to R$ is the joint probability distribution function for the set of random variables $\{\xi_1, \ldots, \xi_d\}$. In the following sections, we describe the non-linear model reduction framework for computing $\alpha(\boldsymbol{x}, \boldsymbol{\xi})$. Details of the implementation of the Smolyak algorithm for Eq. (3.13) can be found in [20].

3.3 Nonlinear model reduction: Its necessity and some basic ideas

In our recent work [20], a linear model reduction strategy was developed to convert experimental statistics into a plausible low-dimensional representation of two-phase microstructures. The first step in that formulation was the conversion of the statistical information into a set of plausible 3D realizations. This feature of first converting the given experimental statistics into a data set of plausible 3D microstructures is continued in the developments featured here. This is motivated by the fact that there exists a variety of mature mathematical and numerical techniques that convert experimental data and statistics into multiple plausible 3D reconstructions of the topology and thus property variations. For instance, the GeoStatistical Modelling Library [73] (GSLIB) converts experimental statistics of the permeability (semi-variograms, correlations, etc.) into plausible 3D models of permeability variations. Similarly, there have been various techniques that have been developed [20, 74, 75, 76, 77], to convert experimental statistics into a plausible 3D reconstructions of two-phase composite microstructures as well as polycrystalline materials.

3.3.1 Linear model reduction: where does it fail?

The PCA based linear model reduction technique that we had formulated [20] has some drawbacks. The most critical of these is that any PCA based approach can only identify the closest linear subspace to the actual space (which is possibly non-linear) in which the data reside. This directly translates into the fact that PCA tends to consistently over-estimate the actual dimensionality of the space. This is illustrated in Fig. 3.2 which shows a plot of the number of eigenvectors (using PCA) required to represent 80% of the information content of a set of images, as the number of such sample images are increased. Each image is a 3D two-phase microstructure that satisfies a specific volume-fraction and two-point correlation. Notice that as the number of samples increases, the number of eigenvectors required for a moderately accurate representation of the data monotonically increases.

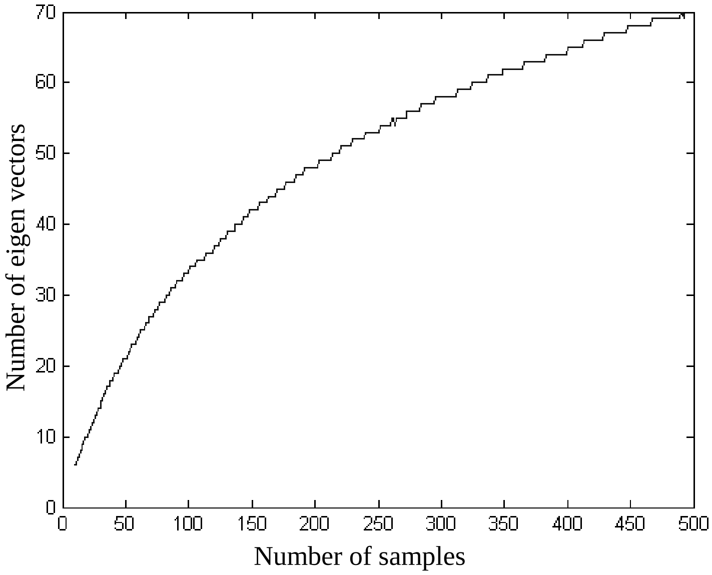

Figure 3.2: Plot of the number of samples versus the number of eigenvectors required to represent 80% of the 'energy' spectrum contained in the samples.

The issue brought out in the discussion above can be understood in a more intuitive way by looking at the simple surface shown in Fig. 3.3(a). The set of points shown in Fig. 3.3(a) all lie on a spiral in 3D space. The global coordinates of any point on the spiral is represented as a 3-tuple. Any PCA based model tries to fit a linear surface such that the reconstruction error is minimized. This is shown by the green plane which is a 2D representation of the data. This clearly results in a bad representation of the original data. On the other hand, knowledge of the geometry of the 3D curve results in representing the global position of any point of the curve on a 2D plane, which is obtained by unravelling the spiral into a plane (Fig. 3.3 (b)). This is essentially the intuitive concept of non-linear model reduction techniques: i.e. they try to unravel and smoothen curves lying in high-dimensional spaces, so that a low-dimensional representation naturally arises. Thus, while PCA based methods would require a 3D representation to accurately describe the spiral shown in Fig. 3.3, a non-linear model reduction method would identify the geometry of the curve, unravel it and provide a simple 2D representation of the data.

3.3.2 Non-linear model reduction: preliminary ideas

The essential idea of nonlinear model reduction finds its roots in image compression and related digital signal processing principles. Figure 3.4(a) shows multiple images of the same object taken at different left-right and up-down poses. Each image is a 64×64 gray-scale picture. Even though each image shown in the figure is defined using $64 \times 64 = 4096$ dimensional vector, each image is in fact uniquely parameterized by just two values, the right-left pose and the up-down pose. It follows that the curve (we will henceforth refer to this

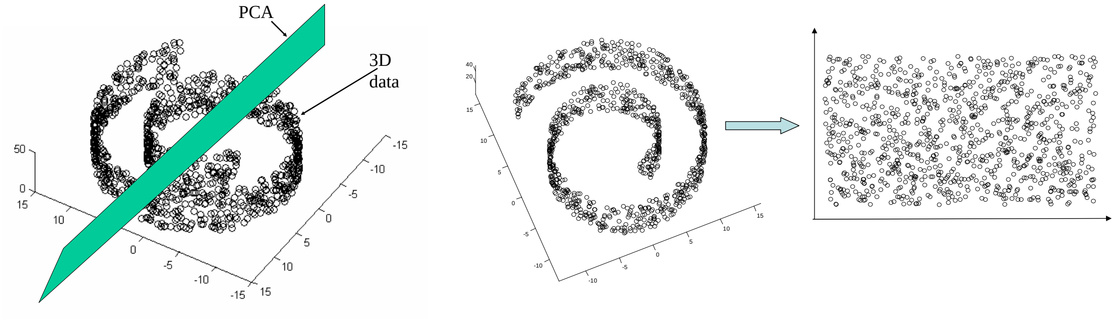

(a) (b)

Figure 3.3: A set of points lying on a spiral in 3D space. The global coordinates of any point on the spiral is represented as a 3-tuple. The figure on the left (a) shows the reduced-order model resulting from a linear PCA based reduction. The figure on the right (b) depicts a non-linear strategy that results in an accurate representation of the 3D spiral (data taken from [78]) that works by "unravelling and smoothing" the 3D spiral into a 2D sheet.

curve as the manifold) representing all possible pictures of this object is embedded in R^{4096} but is parameterized by a region in R^2. The identification of the (small set of) parameters that uniquely define a manifold embedded in a high-dimensional space is called the 'manifold learning problem' [22, 24, 23]. This problem of estimating the low-dimensional representation of unordered high-dimensional data sets is a critical problem arising in studies in vision, speech, motor control and data compression.

Analogous to the problem defined above (using Fig. 3.4 (a)), we define a problem based on the images in Fig. 3.4 (b). Fig. 3.4 (b) shows multiple microstructures that satisfy experimentally determined two-point correlation and volume-fraction. Each microstructure is a $65 \times 65 \times 65$ binary image. Each microstructure that satisfies the given experimental statistics is a point that lies on a curve (manifold) embedded in $65 \times 65 \times 65 = 274625$ dimensional space. The problem of 'manifold learning' or parameter estimation as applied to this

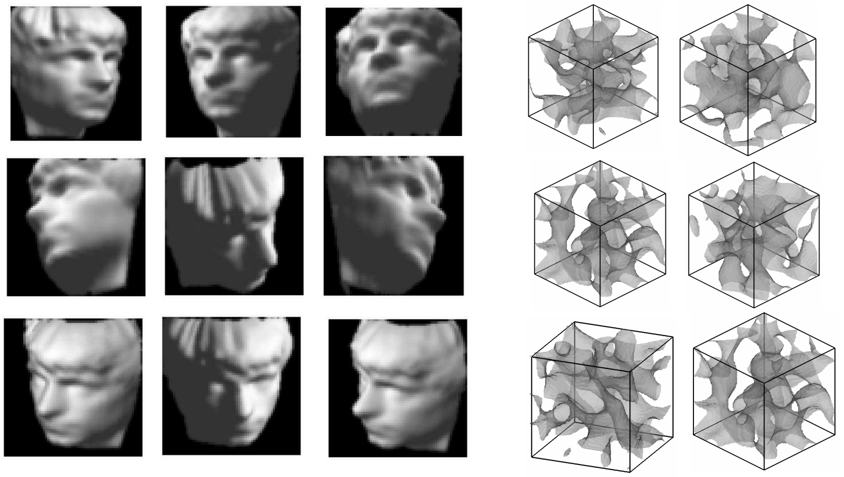

(a) (b)

Figure 3.4: Figure (a) on the left shows images of the same object (from [78]) taken at various poses (left-right and up-down) while Figure (b) on the right shows various two-phase microstructures that satisfy a specific volume-fraction and two-point correlation.

situation is as follows:

Problem statement A: Given a set of N-unordered points belonging to a manifold $\mathcal{M}$ *embedded in a high-dimensional space* R^n*, find a low-dimensional region* $\mathcal{A} \subset R^d$ *that parameterizes* $\mathcal{M}$*, where* $d \ll n$*.*

Classical methods in manifold learning have been methods like the Principle Component Analysis (PCA), Karhunun-Loève expansion (KLE) and multi-dimensional scaling (MDS) [79]. These methods have been shown to extract optimal mappings when the manifold is embedded linearly or almost linearly in the input space. Recently two new approaches have been developed that combine the computational advantages of PCA with the ability to extract the geometric structure of nonlinear manifolds. One set of methods preserve the local geometry of the data. They aim to map nearby points on the manifold to nearby points in the low-dimensional representation. Such methods, Locally Linear Embedding (LLE) [22], Laplacian Eigen Maps, Hessian Eigen maps, essentially construct a homeomorphic mapping between local sets in the manifold to an open ball in a low-dimensional space. The complete mapping is a union of these local maps. An alternate set of approaches towards nonlinear model reduction take a top-down approach. Such global approaches, like the Isomap and its numerous variants, attempt to preserve the geometry at *all scales* [24]. They ensure that nearby points on the manifold (with distance defined via a suitable metric) map to nearby points in the low-dimensional space and faraway points map to faraway points in the low-dimensional space. Though both approaches are viable, we focus our attention to global methods of non-linear dimension reduction. The global approach has been shown to provide a faithful representation of the global structure of the data. Furthermore, based on our developments, it is possible to prove tight error bounds and convergence estimates of the model reduction strategy using global methods. Finally, recent advances in such global approaches have made these strategies computationally very efficient.

The basic premise of the global methods (particularly the Isomap [23] algorithm) is that 'only geodesic distances reflect the true low-dimensional geometry of the manifold'. The geodesic distance (between two-points) on a manifold can be intuitively understood to be the shortest distance between the two-points *along the manifold*. Subsequent to the construction of the geodesic distance between the sample points ($\boldsymbol{x}$) in the high-dimensional space, the global methods construct the low-dimensional parametrization simply as a set of points ($\boldsymbol{y}$) lying in a low-dimensional space that most accurately preserve the geodesic distance. For example, the Isomap algorithm is an isometric transformation of the high-dimensional data into low-dimensional points. The global based methods solve the following version of the problem statement:

Problem statement B: Given a set of N-unordered points belonging to a manifold $\mathcal{M}$ *embedded in a high-dimensional space* R^n*, find a low-dimensional region* $\mathcal{A} \in R^d$ *which is isometric to* $\mathcal{M}$*, with* $d \ll n$*.*

The above discussion provides a basic, intuitive picture of the non-linear model reduction strategy. There are several features – the properties that the manifold satisfies, the notion of distances in the high-dimensional space, the optimality of the low-dimensional parametrization and the accuracy of this parametrization – that require a rigorous mathematical footing. We proceed to develop these in the next section.

3.4 Mathematical formulation

This section is divided into five parts. We first introduce some mathematical preliminaries and define an appropriate distance function $\mathcal{D}$ between two points in $\mathcal{M}_S$. For the straightforward construction of a transformation $\mathcal{F} : \mathcal{M}_S \to \mathcal{A}$ we ensure that $\mathcal{M}_S$ is topologically well-behaved, i.e. it is smooth and has no holes. This can be ensured by showing that $\mathcal{M}_S$ is compact (Section 3.4.1). The next step in the construction of the transformation is the estimation of the pair-wise geodesic distance between all the data points. The geodesic distance reflects the true geometry of the manifold embedded in the high-dimensional space. We utilize developments in the graph approximations to geodesics to do the same (Section 3.4.2). Following this, techniques for estimating the optimal dimensionality of the reduced-order model are developed (Section 3.4.3).

Section 3.4.4 details the application of the Isomap algorithm (along with the estimate of the optimal dimensionality from Section 3.4.3) to construct the low-dimensional parametrization of the input data. Finally Section 3.4.5 details a non-parametric mapping that serves as the reduced-order, data-driven model of the material topology and thus thermal diffusivity variation.

3.4.1 Some definitions and the compactness of the manifold $\mathcal{M}$

We provide a few definitions to make the subsequent presentation clear. Detailed proofs of the lemmas stated here can be found in the Appendix.

Definition 4.1: *By a microstructure* $\boldsymbol{x}$*, we mean a pixelized representation of a 3D topology. Without loss of generality, we assume that the number of pixels representing the microstructure is* $n = q \times q \times q$*.*

Definition 4.2: *Let* $\mathcal{M}_{\mathrm{S}}$ *denote the set of microstructures* $\{\boldsymbol{x}_i\}$ *satisfying a set of statistical correlations* $\mathrm{S} = \{S_1, \ldots, S_p\}$, i.e.

$$\mathcal{M}_{\mathrm{S}} = \{\boldsymbol{x} \in R^n | \ \boldsymbol{x} \ \text{ satisfies } \ \{S_1, \ldots, S_p\}\}. \tag{3.15}$$

Note that these correlations have an increasing hierarchy of information content. That is, the two-point correlation contains more information about the material topology and property distribution than, say, the volume fraction.

Definition 4.3: *We denote as 'upper-correlation function',* S_{upper}*, the statistical correlation function which has a higher-information content than* $\{S_1, \ldots, S_p\}$.

For instance, if $\mathcal{M}_{\mathrm{S}}$ is the set of all microstructures satisfying a first-order constraint S_1 (volume fraction), the *upper-correlation function* for $\mathcal{M}_{\mathrm{S}}$ is the two-point correlation function.

Remark 4.1: In most realistic systems, it is possible to experimentally determine first-order (mean) and second-order (two-point correlation) statistics fairly easily [80]. Higher-order statistics, though feasible, are expensive to experimentally determine. Since we are particularly interested in converting these experimental statistics into viable stochastic models, we will henceforth limit our discussion to the set of two-phase microstructures that satisfy given first- and second-order statistical correlations. Nevertheless, the developments detailed below are in no way limited to second-order statistics and in fact can be extended to include higher-order statistics in a very straightforward manner.

For clarity of presentation, we restrict our analysis to the set of two-phase microstructures satisfying some volume-fraction and two-point correlation. Each microstructure $\boldsymbol{x}$ is represented as a $n = q \times q \times q$ pixelized binary image. Each pixel can take values of 0 or 1, representing one of the two phases constituting the two-phase microstructure. We denote the set of microstructures satisfying the given first- and second-order statistics $S = \{S_1, S_2\}$ by $\mathcal{M}_{S_2}$. The *upper-correlation function* for $\mathcal{M}_{S_2}$ is the three-point correlation function S_3. That is, $S_3(a, b, c)$ is the probability of finding three points, forming a triangle with sides a, b, c that all belong to the same phase. Since the microstructure is discretized/pixelated, a, b, c take integer values. Also, since the microstructure is finite (defined on $q \times q \times q$ pixels), the number of such integer sets (a, b, c) is finite. Using various reconstruction techniques [81, 68], it is possible to generate a set of samples $\boldsymbol{x}_i \in \mathcal{M}_{S_2}$. The aim of the present work is to utilize these realizations to construct a low-dimensional model for the set $\mathcal{M}_{S_2}$.

Definition 4.4: *The function* $\mathcal{D} : \mathcal{M}_{S_2} \times \mathcal{M}_{S_2} \to [0, \infty)$ *is defined for every* $\boldsymbol{x}_1, \boldsymbol{x}_2 \in$

$\mathcal{M}_{S_2}$ *as*

$$\mathcal{D}(\boldsymbol{x}_1, \boldsymbol{x}_2) = |S_{upper}(\boldsymbol{x}_1) - S_{upper}(\boldsymbol{x}_2)|. \tag{3.16}$$

Based on Remark 4.1, $\mathcal{D}$ is defined as

$$\mathcal{D}(\boldsymbol{x}_1, \boldsymbol{x}_2) = \sum_{(a,b,c)} |S_3(a,b,c)(\boldsymbol{x}_1) - S_3(a,b,c)(\boldsymbol{x}_2)|, \tag{3.17}$$

over all possible combinations of a, b, c.

Lemma 4.1: $(\mathcal{M}_{S_2}, \mathcal{D})$ is a metric space.

Remark 4.2: *Notion of distance and equivalence between two microstructures*: The function $\mathcal{D}(\boldsymbol{x}_1, \boldsymbol{x}_2)$ provides a notion of distance between two microstructures $\boldsymbol{x}_1, \boldsymbol{x}_2 \in \mathcal{M}_{S_2}$. Since $\boldsymbol{x}_1, \boldsymbol{x}_2$ belong to $\mathcal{M}_{S_2}$, both have identical volume fraction, S_1 and two-point correlation S_2. We naturally denote them as equivalent if they have the same *upper-correlation function*, S_3. Since we are dealing with statistically reconstructed microstructures, this definition of equivalence ensures that two microstructures are identical if their higher-order topological characterization is identical.

Remark 4.3: Any other mapping that satisfies the three properties of a metric [82] can be used as a measure of equivalence and distance. Since we are dealing with correlation statistics (that inherently result in limited information about the topology), using the upper-correlation function is a natural way of utilizing this limited information towards quantifying the difference between two points (microstructures) in $\mathcal{M}_{S_2}$. An alternate idea of representing the distance between microstructures is to compute the pixel-wise difference between the two microstructures, i.e. $\mathcal{D}(\boldsymbol{x}_1, \boldsymbol{x}_2) = \sqrt{\sum_{i,j,k=1}^{q} (\boldsymbol{x}_1(i,j,k) - \boldsymbol{x}_2(i,j,k))^2}$.

Lemma 4.2: The metric space $(\mathcal{M}_{S_2}, \mathcal{D})$ is totally bounded.

Lemma 4.3: The metric space $(\mathcal{M}_{S_2}, \mathcal{D})$ is dense.

Lemma 4.4: The metric space $(\mathcal{M}_{S_2}, \mathcal{D})$ is complete.

Theorem 4.1: The metric space $(\mathcal{M}_{S_2}, \mathcal{D})$ is compact.

Proof: Follows from Lemma 4.2 and Lemma 4.4 (see Theorem 45.1 in [26]).

3.4.2 Estimating the pair-wise geodesic distances: graph approximations

The Isomap algorithm attempts to find a low-dimensional representation, $\{\boldsymbol{y}_i\}$ of the points $\{\boldsymbol{x}_i\}$ such that $\{\boldsymbol{y}_i\}$ is isometric to $\{\boldsymbol{x}_i\}$ based on the geodesic distances between the points. It is therefore necessary to compute the pair-wise geodesic distance between all the input data points $\{\boldsymbol{x}_i\}$.

Definition 4.5: Denote the intrinsic geodesic distance between points in $\mathcal{M}_{S_2}$ by $\mathcal{D}_M$. $\mathcal{D}_M$ is defined as

$$\mathcal{D}_M(\boldsymbol{x}_1, \boldsymbol{x}_2) = \inf_{\gamma}\{\text{length}(\gamma)\}, \tag{3.18}$$

where γ varies over the set of smooth arcs connecting $\boldsymbol{x}_1$ and $\boldsymbol{x}_2$. We wish to remind the reader that length of the arcs in the equation above are defined using the distance metric $\mathcal{D}$.

It is important to appreciate the fact that we start off with no knowledge of the geometry of the manifold. We are only given N unordered samples $\{\boldsymbol{x}_i\}$ lying in $\mathcal{M}_{S_2}$. Hence, the Definition 4.5 of the geodesic distance is not particularly useful in numerically computing the distance between two-points. An approximation of the geodesic distance is required to proceed further. Such an approximation is provided via the concept of graph distance. We subsequently show that this approximation asymptotically matches the actual geodesic distance (Eq. (3.18)) as the number of samples, N, increases (see Theorem 4.2 below).

The unknown geodesic distances in $\mathcal{M}_{S_2}$ between the data points are approximated in terms of a *graph distance* with respect to a graph G constructed on the data points. This neighborhood graph G is very simple to construct [23]. Two points share an edge on the graph if they are neighbors. The neighborhood information is estimated in terms of the distance metric $\mathcal{D}$. $\boldsymbol{x}_1$ and $\boldsymbol{x}_2$ are neighbors if $\mathcal{D}(\boldsymbol{x}_1, \boldsymbol{x}_2) = min_{j=1,\ldots,N}(\mathcal{D}(\boldsymbol{x}_1, \boldsymbol{x}_j))$. These neighborhood relations are subsequently represented as a weighted graph G over all the data points. The edges are given weights corresponding to the distance $\mathcal{D}(\boldsymbol{x}_i, \mathbf{x}_j)$ between points.

For points close to each other, the geodesic distance is well approximated by the distance metric $\mathcal{D}$. This is because the curve can be locally approximated to be a linear patch, and the distance between two points on this patch is the straight line distance between them. This straight line distance is given by the distance metric $\mathcal{D}$, which is just the edge length between the points on the graph, G. On the other hand, for points positioned faraway from each other, the geodesic distance is approximated by adding up a sequence of short hops between neighboring points [23]. These short hops can be computed easily from the neighborhood graph G. Denote the shortest path distance between two-points $\boldsymbol{x}_1$ and $\boldsymbol{x}_2$ on the graph G as $\mathcal{D}_G$. The key to constructing the low-dimensional representation is to approximate $\mathcal{D}_M$ as $\mathcal{D}_G$. As the number of input data points increases, the graph distance approximation approaches the intrinsic geodesic distance. The asymptotic convergence of the graph distance to the geodesic distance is rigorously stated in Theorem 4.2. This theorem utilizes some parameters for the quantification of the geometry of the manifold, particularly the minimal radius of curvature, r_o and the minimal branch separation s_o. For the sake of completeness, we state the theorem below. For the sake of brevity, we leave out the definitions of these abstract parameters (the interested reader is referred to [23, 26] for discussion of these terms).

Theorem 4.2: *Let* $\mathcal{M}_{S_2}$ *be a compact manifold of* R^n *isometrically equivalent to a convex domain* $\mathcal{A} \subset R^d$. *Let* $0 < \lambda_1, \lambda_2 < 1$ *and* $0 < \mu < 1$ *be given, and let* $\epsilon > 0$ *be chosen such that* $\epsilon < s_o$ *and* $\epsilon \leq \frac{2}{\pi} r_o \sqrt{24\lambda_1}$. *A finite sample set* $\{\mathbf{x}_i\}$, $i = 1, \ldots, N$ *is chosen randomly from* $\mathcal{M}_{S_2}$ *with a density* α, *with* $\alpha > \frac{log(\frac{V}{\mu\eta_d(\lambda_2\epsilon/16)^d})}{\eta_d(\lambda_2\epsilon/8)^d}$, *where* V *is the volume of* $\mathcal{M}_{S_2}$ *and* η_d *is the volume of the unit ball in* R^d. *The neighborhood graph* G *is constructed on* $\{\mathbf{x}_i\}$. *Then, with probability at least* $1 - \mu$, *the following inequalities hold for all* $\mathbf{x}, \mathbf{y}$ *in* $\mathcal{M}_{S_2}$:

$$(1 - \lambda_1)\mathcal{D}_M(\mathbf{x}, \mathbf{y}) \leq \mathcal{D}_G(\mathbf{x}, \mathbf{y}) \leq (1 + \lambda_2)\mathcal{D}_M(\mathbf{x}, \mathbf{y}).$$

Proof: Follows from Theorem B in [25].

3.4.3 Estimating the optimal dimension, d, of the low-dimensional representation

$\mathcal{M}_{S_2}$ is intrinsically parameterized by a low-dimensional set $\mathcal{A} \subset R^d$. As a first step towards constructing $\mathcal{A}$, the pair-wise geodesic distances, $\mathcal{D}_G$, are constructed from the neighborhood graph G. Before we can proceed further, the intrinsic dimensionality of this low-dimensional space, d has to be estimated.

We draw from the recent work in [27, 28], where the intrinsic dimension of an embedded manifold is estimated using a novel geometrical probability approach. This work is based on a powerful result in geometric probability - the Breadwood-Halton-Hammersley [83] theorem where d is linked to the rate of convergence of the length-functional of the minimal spanning tree of the geodesic distance matrix of the unordered data points in the high-dimensional space. Consistent estimates of the intrinsic dimension d of the sample set are obtained using a very simple procedure.

The sequel utilizes concepts from graph theory. We provide some of the essential definitions below. For a detailed discussion of graphs, trees and related constructs, the interested reader is referred to [29]. Consider a set of k points (vertices) and a graph defined on this set. A graph consists of two types of elements, namely vertices and edges. Every edge has two endpoints in the set of vertices, and is said to connect or join the two endpoints.

- A weighted graph associates a weight (here, this weight is the distance between the vertices) with every edge in the graph.
- A tree is a graph in which any two vertices are connected by exactly one path.
- A spanning tree of a graph (with k vertices) is a subset of $k - 1$ edges that form a tree.
- The minimum spanning tree of a weighted graph is a set of edges of minimum total weight which form a spanning tree of the graph.

Definition 4.7: The geodesic minimal spanning tree (GMST) is the minimal spanning tree of the graph G. The length functional, $L(\{\boldsymbol{x}\})$ of the GMST is defined as $L(\{\boldsymbol{x}\}) = \min_{T \in T_N} \sum_{e \in T} |e|$, where T_N is the set of all spanning trees of the graph G and e are the edge-weights of the graph. This is in fact, simply the total weight of the tree.

The mean length of the GMST is linked to the intrinsic dimension d of a manifold $\mathcal{M}_{S_2}$ embedded in a high-dimensional space R^n through the following theorem:

Theorem 4.3: *Let $\mathcal{M}_{S_2}$ be a smooth d-dimensional manifold embedded in R^n through a map $\mathcal{F}^{-1} : R^d \to \mathcal{M}_{S_2}$. Let $2 \leq d \leq n$. Suppose that $\{\boldsymbol{x}_i\}$, $i = 1, \ldots, N$ are random vectors in $\mathcal{M}_{S_2}$. Assume that each of the edge lengths $|e_{ij}|_M$ computed from the graph* G *converge to $|\mathcal{F}(\boldsymbol{x}_i) - \mathcal{F}(\boldsymbol{x}_j)|_2$ as $N \to \infty$ (i.e. the graph distance converges to the true manifold distance - This is guaranteed by Theorem 4.2). Then the length functional, $L(\{\boldsymbol{x}\})$ of the GMST satisfies*:

$$\lim_{N\to\infty} L(\{\boldsymbol{x}\})/N^{(d'-1)/d'} = \begin{cases} \infty & \text{if } d' < d, \\ \beta_m C & \text{if } d' = d, \\ 0 & \text{if } d' > d, \end{cases} \tag{3.19}$$

where β_m is a constant, and C is a non-zero function defined in $\mathcal{M}_{S_2}$.
Proof: Follows from Theorem 2 in [30].

Theorem 4.3, particularly the asymptotic limit given in Eq. (3.19) for the length functional of the GMST provides a means of estimating the intrinsic dimension of the manifold. It is clearly seen that the rate of convergence of $L(\{\boldsymbol{x}\})$ is strongly dependent on d. Following [30], we use this strong rate dependence to compute d. Defining $l_N = log(L(\{\boldsymbol{x}\}))$, gives the following approximation for l_N (from Eq. (3.19))

$$l_N = a \log(N) + b + \epsilon_N, \tag{3.20}$$

where

$$
\begin{aligned}
a &= \frac{d-1}{d}, & (3.21)\\
b &= \log(\beta_m C), & (3.22)
\end{aligned}
$$

and ϵ_N is an error residual that goes to zero as $N \to \infty$ [27, 28, 30]. The intrinsic dimensionality, d can be estimated by finding the length functional for different number of samples N and subsequently finding the best fit for (a, b) in Eq. (3.20).

3.4.4 Constructing the low-dimensional parametrization, $\mathcal{A}$

Section 3.4.2 presented the construction of the geodesic distance between all pairs of input points, while Section 3.4.3 provided an estimation of the dimensionality, d, of the low-dimensional representation. Denote as **M**, the pair-wise distance matrix (based on the geodesic distance), with elements $d_{ij} = \mathcal{D}_G(\boldsymbol{x}_i, \boldsymbol{x}_j)$ where $i, j = 1, \ldots, N$. Multi-dimensional scaling [79, 84] (MDS) arguments are used to compute the set of low-dimensional points that are isometric to these high-dimensional images. The objective of MDS is: *Given a matrix,* **M**, *of pairwise distances between N (high-dimensional) points, find a configuration of points in a low-dimensional space such that the coordinates of these N points yield a Euclidean distance matrix whose elements are identical to the elements of the given distance matrix* **M**.

$$
\begin{aligned}
&\texttt{Given } \mathbf{M}, \texttt{ find } \{\boldsymbol{y}_i\}\ i = 1, \ldots, N \texttt{ such that } \boldsymbol{y}_i \in R^d \texttt{ and}\\
&\qquad\qquad \sum_{k=1}^{d} (y_{ik} - y_{jk})^2 = d_{ij}^2, \texttt{ for all } i, j. \qquad (3.23)
\end{aligned}
$$

This is called 'coordinate recovery or parametrization': finding a set of points given only the pair-wise distance between the points.

Define the $N \times N$ symmetric matrix **A** with elements $a_{ij} = -\frac{1}{2} d_{ij}^2$. Define the

$N \times N$ centering matrix [79, 84], $\mathbf{H} = \mathbf{I} - \frac{1}{N}\mathbf{1}\mathbf{1}'$ with elements $h_{ij} = \delta_{ij} - 1/N$. Define the $N \times d$ matrix of points $\mathbf{Y} = (\boldsymbol{y}_1, \ldots, \boldsymbol{y}_N)^T$. Assume without loss of generality that the centroid of the set of points is the origin ($\sum_{i=1}^{N} \boldsymbol{y}_i = \mathbf{0}$). Define the $N \times N$ matrix $\mathbf{B}$ whose components are the scalar products $\boldsymbol{y}_i^T \cdot \boldsymbol{y}_j$.

$$b_{ij} = \sum_{k=1}^{d} y_{ik} y_{jk} = \boldsymbol{y}_i^T \cdot \boldsymbol{y}_j. \tag{3.24}$$

The problem at hand is to estimate the coordinates $\boldsymbol{y}_i$, given $\mathbf{M}$. We relate these points $\{\boldsymbol{y}_i\}$ to $\mathbf{B}$. $\mathbf{B}$ in turn can be represented in terms of the known distances $\mathbf{M} = \{d_{ij}\}$. It can easily be shown that [79, 84]

$$\mathbf{B} = \mathbf{HAH}. \tag{3.25}$$

$\mathbf{B}$ is a positive definite matrix that can be decomposed as follows [84]:

$$\mathbf{B} = \mathbf{\Gamma \Lambda \Gamma}. \tag{3.26}$$

Here, $\mathbf{\Lambda} = \mathrm{diag}(\lambda_1, \ldots, \lambda_N)$ is the diagonal matrix of the positive eigenvalues of $\mathbf{B}$ and $\mathbf{\Gamma} = (\gamma_1, \ldots, \gamma_N)^T$ the matrix of the corresponding eigenvectors. Note that $\mathbf{B}$ will have a decaying eigen-spectrum. The required set of points $\boldsymbol{y}_1, \ldots, \boldsymbol{y}_N$ is related to the d largest eigenvalues/eigenvectors of $\mathbf{B}$. $\mathbf{B}$ is by definition (see Eq. (3.24), the scalar product matrix)

$$\mathbf{B} = \mathbf{Y}\mathbf{Y}^T. \tag{3.27}$$

From Eq. (3.26) and Eq. (3.27), an estimate of $\mathbf{Y}$ in terms of the largest d eigenvectors of $\mathbf{B}$ follows: $\mathbf{Y} = \mathbf{\Gamma}_d \mathbf{\Lambda_d}^{\frac{1}{2}}$, where $\mathbf{\Lambda}_d$ is the diagonal ($d \times d$) matrix of the largest d eigenvalues of $\mathbf{B}$ and $\mathbf{\Gamma}_d$ is the $N \times d$ matrix of the corresponding eigenvectors.

The knowledge of the optimal dimensionality, d, (from Section 3.4.3) is quite useful in truncating the eigen values of the $N \times N$ matrix $\mathbf{B}$. In contrast, classical

PCA based techniques truncate the expansion based on representing some percentage of the eigen-spectrum i.e. choose the largest d eigenvalues that account for, say, 95% of the eigen-spectrum. ($\frac{\sum_{i=1}^{d} \lambda_i}{\sum_{i=1}^{N} \lambda_i} > 0.95$).

We have converted a finite set of data points $\{\boldsymbol{x}_i\}$, $i = 1, \ldots, N$ from $\mathcal{M}_{\mathrm{S}_2} \subset R^n$ to points $\{\boldsymbol{y}_i\}$, $i = 1, \ldots, N$ in R^d. These points belong to a connected convex subset $\mathcal{A} \subset R^d$ (Theorem 4.2). This convex region can be numerically estimated as the convex hull of the set of points $\{\boldsymbol{y}_i\}$, $i = 1, \ldots, N$. Hence the low-dimensional parametrization of $\mathcal{M}_{\mathrm{S}_2}$ is given by

$$\mathcal{A} = \{\boldsymbol{\xi} \in R^d \mid \boldsymbol{\xi} \in \text{ConvexHull}(\{\boldsymbol{y}_1, \ldots, \boldsymbol{y}_N\})\}. \tag{3.28}$$

The stochastic collocation procedure for the solution of SPDEs involves computing the solution at various sample points, $\boldsymbol{\xi}$, from this space, $\mathcal{A}$.

3.4.5 Construction of a non-parametric mapping $\mathcal{F}^{-1} : \mathcal{A} \rightarrow \mathcal{M}_{\mathrm{S}_2}$

Given a set of samples $\{\boldsymbol{x}_i\}$, $i = 1, \ldots, N$ in $\mathcal{M}_{\mathrm{S}_2}$, the nonlinear dimension reduction strategy (Section 3.4.2) coupled with the dimension estimation method (Section 3.4.3) convert these points into a set of points $\{\boldsymbol{y}_i\}$, $i = 1, \ldots, N$ belonging to a convex set $\mathcal{A}$. *This convex region $\mathcal{A} \subset R^d$, defines the reduced representation of the space of microstructures, $\mathcal{M}_{\mathrm{S}_2}$, satisfying the given statistical correlations* S_2. $\mathcal{A}$ can be considered to be a surrogate space to $\mathcal{M}_{\mathrm{S}_2}$. One can access the complete variability in the topology and property distribution of microstructures in $\mathcal{M}_{\mathrm{S}_2}$ by simply sampling over the region $\mathcal{A}$. In the collocation based solution strategy for solving SPDEs, one constructs the statistics of the dependant variable by sampling over a discrete set of microstructures. Since we propose to utilize $\mathcal{A}$ as a reduced representation of $\mathcal{M}_{\mathrm{S}_2}$, we sample over a discrete set of points $\boldsymbol{\xi} \in \mathcal{A}$ instead. But we have no knowledge of the image of a random point $\boldsymbol{\xi} \in \mathcal{A}$ in the microstructural space $\mathcal{M}_{\mathrm{S}_2}$ (we only know that the points $\{\boldsymbol{y}_i\}$ for $i = 1, \ldots, N$ map to the microstructures $\{\boldsymbol{x}_i\}$ for $i = 1, \ldots, N$). *For a usable reduced-order model of the microstructure space, an explicit mapping $\mathcal{F}^{-1}$ from $\mathcal{A}$ to $\mathcal{M}_{\mathrm{S}_2}$ has to be constructed.*

There are numerous ways of constructing parametric as well as non-parametric mappings between two sets of objects. For instance, neural networks can be trained using the sample points $(\{\boldsymbol{y}_i\}, \{\boldsymbol{x}_i\})$, $i = 1, \ldots, N$ to construct a non-parametric mapping $\mathcal{F}^{-1}$. There have been recent reports of variants of the Isomap algorithm that along with constructing the reduced-order representation of the samples also construct an explicit mapping between the two sets [85]. But there are two significant issues that have to be considered when one utilizes such mapping strategies: 1) Most of these explicit mapping strategies are essentially some form of interpolation rule that utilize the sample set of values $(\{\boldsymbol{y}\}, \{\boldsymbol{x}\})$. One has to make sure that the interpolated result, $\boldsymbol{x}$ ($\boldsymbol{x} = \mathcal{F}^{-1}(\boldsymbol{\xi})$) for some arbitrary point $\boldsymbol{\xi} \in \mathcal{A}$ actually *belongs* to $\mathcal{M}_{\mathrm{S}_2}$. 2) Care must be taken to formulate the explicit mapping in a way that results in a computationally simple methodology of finding the images of points. This is very significant considering the fact that we will potentially deal with *very large* pixel sized images (pixelized microstructures or property maps) with pixel counts of the order of $128 \times 128 \times 128$. Any strategy that involves performing non-trivial operations on large data sets of (high resolution) property maps would make the complete process very inefficient. We propose several strategies of constructing computationally simple mappings between the two spaces $\mathcal{M}_{\mathrm{S}_2}$ and $\mathcal{A}$ keeping in mind the issues raised above.

Method 1: Nearest neighbor map

This is the simplest map (illustrated schematically in Fig. 3.5) that sets the image of an arbitrary point in the region $\mathcal{A}$ to the image of the nearest sampled point. The nearest point is the point that is the smallest Euclidean distance from the given arbitrary point. This method is particularly useful when the sampling density (α as defined in Theorem 4.5) is large, i.e. this method results in a reliable mapping when the number of microstructure samples $\{\boldsymbol{x}_i\}$, $i = 1, \ldots, N$ is large.

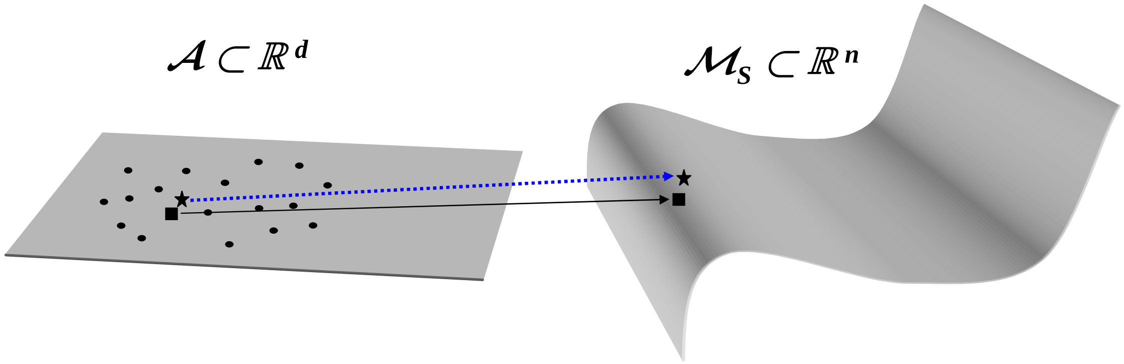

Figure 3.5: The figure above illustrates the simplest possible mapping between the low-dimensional region $\mathcal{A}$ and the high-dimensional microstructural space $\mathcal{M}_{S_2}$. Given an arbitrary point $\boldsymbol{\xi} \in \mathcal{A}$, find the point $\boldsymbol{y}_k$ closest to $\boldsymbol{\xi}$ from the sampled points $\{\boldsymbol{y}_i\}$, $i = 1, \ldots, N$. Assign the image value of $\boldsymbol{y}_k$ i.e. $\boldsymbol{x}_k$ to the image of $\boldsymbol{\xi}$.

It is simple to construct error estimates for this mapping. Given an arbitrary point $\boldsymbol{\xi} \in \mathcal{A}$, approximating it by its closest neighbor results in an error, $e_{\mathcal{A}}$, given by $e_{\mathcal{A}} = \min_{i=1,\ldots,N} \sqrt{\sum_{k=1}^{d} (\xi_k - y_{ik})^2}$. From isometry, the error between the actual image and the mapped image is given by $e = e_{\mathcal{A}}$. This error can be made arbitrarily small by increasing N.

Method 2: Local linear interpolation

A simple non-parametric mapping based on the k-nearest neighbors of a point is defined (Fig. 3.6) as follows: Given any point $\boldsymbol{\xi} \in \mathcal{A}$, find the k-nearest neighbors, $\hat{\boldsymbol{y}}_i$, $i = 1, \ldots, k$ (k defined a priori) to $\boldsymbol{\xi}$ from the set $\{\boldsymbol{y}_i\}$. Compute the (Euclidean) distance $l_i = \sqrt{\sum_{p=1}^{d}(\xi_p - \hat{y}_{ip})^2}$ of $\boldsymbol{\xi}$ from $\hat{\boldsymbol{y}}_i$ $i = 1, \ldots, k$. The point $\boldsymbol{\xi}$ can be represented as a weighted sum of its k-nearest neighbors as

$$\boldsymbol{\xi} = \frac{\sum_{i=1}^{k} \frac{\hat{\boldsymbol{y}}_i}{l_i}}{\sum_{i=1}^{k} \frac{1}{l_i}}. \tag{3.29}$$

Utilizing the fact that the isometric embedding that generated the points $\boldsymbol{y}_i$ from $\boldsymbol{x}_i$ conserves distances, the image of $\boldsymbol{\xi}$ is then given by

$$\boldsymbol{x} = \frac{\sum_{i=1}^{k} \frac{\hat{\boldsymbol{x}}_i}{l_i}}{\sum_{i=1}^{k} \frac{1}{l_i}}. \tag{3.30}$$

That is, the image of $\boldsymbol{\xi}$ is the weighted sum of the images of the k-nearest neighbors of $\boldsymbol{\xi}$ (where the nearest neighbors are taken from the N-sampled points).

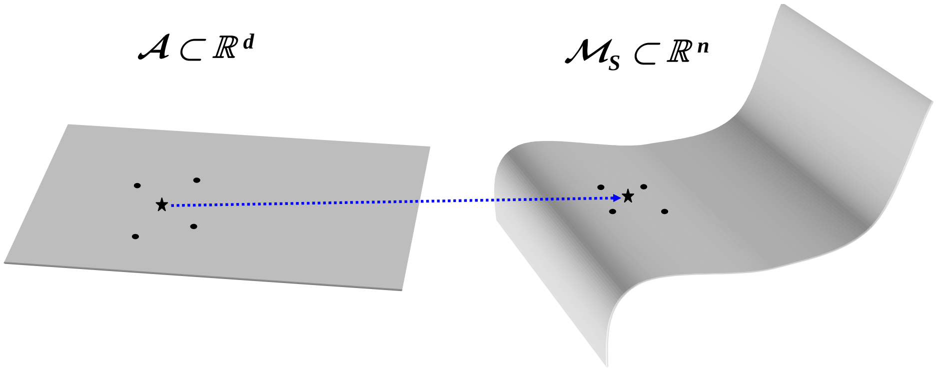

Figure 3.6: The figure above illustrates a local linear (k-neighbor) interpolation mapping between the low-dimensional region $\mathcal{A}$ and the high-dimensional microstructural space $\mathcal{M}_{S_2}$.

The linear interpolation procedure is based on the principle that a small region in a highly-curved manifold can be well approximated as a linear patch.

This is in fact one of the central concepts that result in local strategies of non-linear dimension reduction [22, 24] (see Section 3.3 for a discussion of global versus local strategies of non-linear dimension reduction). This linear patch is constructed using the k-nearest neighbors of a point $\boldsymbol{\xi}$. As the sampling density (the number of sample points, N) used to perform the nonlinear dimension reduction increases, the mean radius of the k-neighborhood of a point approaches zero ($\lim_{N\rightarrow\infty} \max_{i=1,\ldots,k} \|\boldsymbol{\xi} - \hat{\boldsymbol{y}}_i\|_2 \rightarrow 0$), ensuring that the linear patch represents the actual curved manifold arbitrarily well.

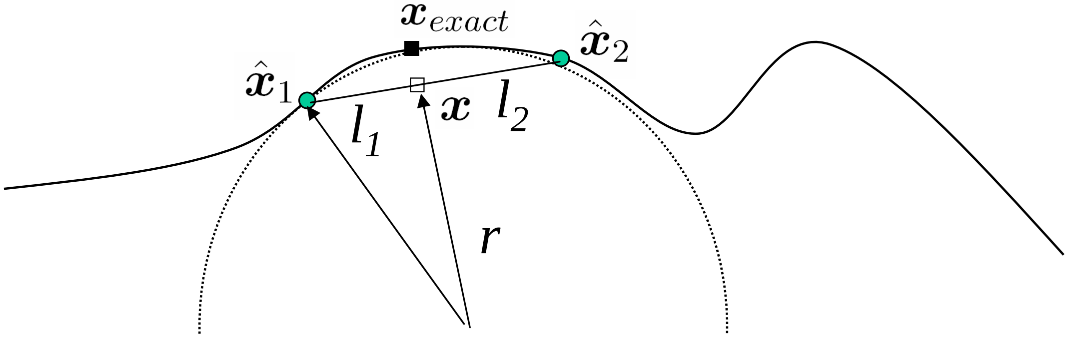

Figure 3.7: Simple estimate for the interpolation error in Method 2: Let r denote the local radius of curvature of the function near the point $\boldsymbol{x}_{exact}$ (the filled square). We approximate the curve by a linear patch, resulting in some error. This error is the distance between the approximate linear image, $\boldsymbol{x}$ (the unfilled square) and the actual point, $\boldsymbol{x}_{exact}$ (the filled square). This distance can be approximated from simple geometry as a function of r and the local geodesic distance between the points.

It is possible to estimate approximate error bounds by computing the local curvature of the manifold. Denote by $\boldsymbol{x}$, the image of the point $\boldsymbol{\xi}$. As before, let the k-nearest neighbors of $\boldsymbol{\xi}$ be $\hat{\boldsymbol{y}}_i$ and their corresponding images in $\mathcal{M}_{S_2}$ be $\hat{\boldsymbol{x}}_i$. The local curvature of the manifold in the neighborhood of $\boldsymbol{x}$ can be approximated from the geodesic distances between the points. Let r denote the radius of curvature of the manifold at $\boldsymbol{x}$. The error in the interpolation based representation is caused by considering the space to be locally linear, when it is curved (see Fig. 3.7). This error is approximated from simple geometry as $e = \max_{i=1,\ldots,k}(r - \sqrt{r^2 - l_i^2})$.

Method 3: Local linear interpolation with projection

The local linear interpolation method (Method 2) can be made exact by simply projecting the image obtained after interpolation onto the manifold (shown schematically in Fig. 3.8). This ensures that the image lies on the manifold $\mathcal{M}_{S_2}$.

The projection is numerically computed as follows: Denote the microstructure obtained after the interpolation step as $\hat{\boldsymbol{x}}$. The locally linear interpolation provides a good approximation of the exact image, $\hat{\boldsymbol{x}} \approx \boldsymbol{x}_{exact}$, where $\boldsymbol{x}_{exact}$ is that microstructure on $\mathcal{M}_{S_2}$ whose geodesic distances from each of the k microstructures $\boldsymbol{x}_i,\ i = 1, \ldots, k$ is l_i. The errors in this approximation are due to the fact that the approximation $\hat{\boldsymbol{x}}$ does not *usually lie on the manifold* (as seen in Fig. 3.8). That is, $\hat{\boldsymbol{x}}$ does not satisfy the statistical correlations $S = \{S_1, \ldots, S_p\}$ that all points on the manifold satisfy.

The projection operation essentially modifies the point $\hat{\boldsymbol{x}}$ to satisfy these correlations. This can be achieved computationally by performing a stochastic optimization problem starting from $\hat{\boldsymbol{x}}$ [76, 80, 86]. Since $\hat{\boldsymbol{x}}$ is very close to $\boldsymbol{x}_{exact}$, these algorithms are guaranteed to reach the local minima defined by $\boldsymbol{x}_{exact}$. In the context of the numerical examples presented in this work, using two-phase microstructures (see Section 3.6), the stochastic optimization is done as follows: Starting from the approximate microstructure $\hat{\boldsymbol{x}}$, compute the volume fraction and two-point correlation of this image. Change the pixel values of t sites in this

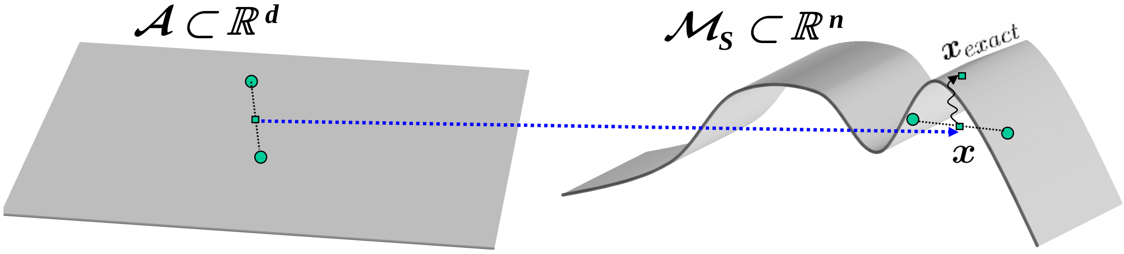

Figure 3.8: The local linear interpolation method can be made exact by simply projecting the image obtained after interpolation onto the manifold. This is illustrated in the figure above, where the botted blue line represents the linear interpolation and the curved line represents the projection operator that constructs the image lying on the manifold.

microstructure such that the volume-fraction matches the experimental volume fraction. Following this, randomly swap pixel values in the microstructure (accepting a move only if the error in the two-point correlation decreases), until the two-point correlation matches the experimental value. This can be considered as a version of simulated annealing, with the starting point, $\hat{\boldsymbol{x}}$ being close to the optimal point, $\boldsymbol{x}_{exact}$.

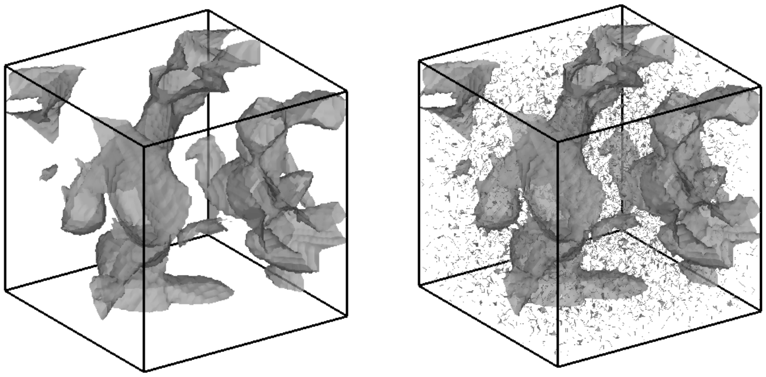

Figure 3.9: Sample illustration of the projection step: The figure on the left is a microstructure after interpolation. Projecting it onto the manifold yields the microstructure on the right. There is negligible change in the three point correlation between the micorstructures.

One question that arises from this mapping strategy is the following: The initial goal of the mapping was to construct a microstructure (lying on the manifold) that was a distance (geodesically) l_i from $\boldsymbol{x}_i$. The interpolation step ensures this distance (but the microstructure does not lie on the manifold). How much deviation from this distance does the projection operator cause? By swapping the pixels in the microstructure during the stochastic optimization step, the three-point correlation is being changed (which is a measure of distance). But in all of our numerical experiments, this optimization converged within 1000 such pixel flips, thus negligibly affecting the three-point correlation (since the three-point correlation is computed by sampling over $65 \times 65 \times 65 \sim 300,000$ points, changing 0.3% of the pixels is negligibly small). This is illustrated pictorially using a sample example shown in Fig. 3.9. The number of neighbors used for the local-linear interpolation map is $k = 10$.

In all three methods detailed above, we only utilize the given input data $\{\boldsymbol{x}_i\}$ to construct the mapping for an arbitrary point $\boldsymbol{\xi} \in \mathcal{A}$. The mapped microstructure, $\mathcal{F}^{-1}(\boldsymbol{\xi})$ is constructed solely based on the available input microstructures and not based on direct reconstruction from moments. In case of the projection operation used in method 3, the mapped microstructure is moved onto the manifold $\mathcal{M}_{S_2}$. This operation changes less that 0.3% of the microstructure having negligible effect on the thermal behavior of the microstructure.

In potential applications where such projection techniques are infeasible, there are two possible solution strategies that can be pursued: one can use an alternate definition of the distance between the images (see Remark 4.3) or one can utilize more computationally demanding reconstruction [81] or training frameworks [85] to construct the mapping $\mathcal{F}^{-1} : \mathcal{A} \rightarrow \mathcal{M}_{S_2}$.

3.4.6 The low-dimensional stochastic input model $\mathcal{F}^{-1} : \mathcal{A} \rightarrow \mathcal{M}_{S_2}$

$\mathcal{A}$ represents the space of d-tuples $\boldsymbol{\xi} = (\xi_1, \ldots, \xi_d)$ that map to microstructures that satisfy the statistical properties $S = \{S_1, \ldots, S_p\}$.

Remark 4.8: In our theoretical derivations in this section, we have ensured that $\mathcal{A}$ is indeed a convex, connected and compact region of R^d. Hence, starting from a large set of points $\{\boldsymbol{y}_i\},\ i = 1, \ldots, N$ in $\mathcal{A}$, one can represent the complete region $\mathcal{A}$ as the convex hull of the points $\{\boldsymbol{y}_i\},\ i = 1, \ldots, N$.

Each of the microstructures in $\mathcal{M}_{S_2}$ (by definition) satisfies all required statistical properties, therefore they are equally probable to occur. That is, every point in the manifold $\mathcal{M}_{S_2}$ is equiprobable. This observation provides a way to construct the stochastic model for the allowable microstructures. Define the stochastic model for the topology variation as $\mathcal{F}^{-1}(\boldsymbol{\xi}) : \mathcal{A} \rightarrow M$ where $\boldsymbol{\xi} = (\xi_1, \ldots, \xi_d)$ is a uniform random variable chosen from $\mathcal{A}$. This low-dimensional stochastic model $\mathcal{F}^{-1}$ for the microstructure is the stochastic input in the SPDE (Eq. (3.13)) defining the diffusion problem.

3.5 Numerical implementation

This section contains recipes for the numerical implementation of the theoretical developments detailed in the previous sections. We divide this section into various subsections that sequentially discuss the data-driven strategy, starting with the generation of the samples given some limited microstructural information (Section 3.5.1), the algorithm for constructing the low-dimensional region $\mathcal{A}$ (Section 3.5.2) and the Smolyak algorithm for the solution of the SPDEs (Section 3.5.3).

3.5.1 Microstructure reconstruction: creating the samples $\boldsymbol{x}_i$

Given some experimentally determined statistical correlation functions of the microstructure, the goal is to reconstruct a large set of microstructures satisfying these correlation functions. This is the first step towards building a reduced-order model to the microstructural space. In this work, the microstructure is considered to be a level cut of a Gaussian Random Field (GRF). The statistical correlations are enforced during the reconstruction of the GRF using the given information [87, 69, 88]. With this method, a set of N 3D models of the property variations can be generated.

3.5.2 Constructing the low-dimensional region $\mathcal{A}$

The reconstruction procedure results in a large set of random samples $\boldsymbol{x}_i$ from the space $\mathcal{M}_{S_2}$. The following steps are followed to compute the corresponding points $\{\boldsymbol{y}_i\}$.

Step 1: Find the pair-wise distances, $\mathbf{P}$ between the N samples $\boldsymbol{x}_i$, $i = 1, \ldots, N$. This is done by first defining an appropriate distance metric, $\mathcal{D}$ between the microstructures. In the example (Section 3.6) using two-phase microstructure, we define the distance between two microstructures as the difference between their three-point correlations. This operation is obviously of $O(N^2)$ complexity.

Step 2: Construct the neighborhood graph, G, of this sample set. That is, determine which points are neighbors on the manifold based on the distance $\mathbf{P}(i, j)$. Find the nearest k-neighbors of each point. This is performed using a sorting algorithm ($O(NlogN)$ complexity). Connect these points on the graph G and set the edge lengths equal to $\mathbf{P}(i, j)$. The total complexity of this operation is $O(N^2 logN)$.

```
for i = 1:N
[z,I] = sort ($\mathbf{P}(i,:)$), z are the sorted distances
and I are the corresponding indices
G(1:k,i) = I(2:k+1)
```

Step 3: Estimate the geodesic distance $\mathbf{M}(i, j)$ between all pairs of points on the manifold. This can be done by computing the shortest path distances in the graph G. There are several algorithms to compute the shortest path on a graph. In our implementation, we utilize Floyd's algorithm to compute $\mathbf{M}(i, j)$. The complexity of this step is $O(N^3)$.

```
Initialize $\mathbf{M}(i,j)$ as
$\mathbf{M}(i,j) = \mathbf{P}(i,j)$ if i,j are neighbors or $\mathbf{M}(i,j) = \infty$ otherwise

for k = 1:N
    for each pair (i,j) in 1:N
        $\mathbf{M}(i,j) = \min(\mathbf{M}(i,j), \mathbf{M}(i,k) + \mathbf{M}(k,j))$
```

Step 4: Decide on the optimal dimensionality, d, of the low-dimensional space $\mathcal{A}$. Using the graph G [30], estimate the average geodesic MST length. This is done as shown below.

```
Choose $Q$ integers $p = p_1, \ldots, p_Q$ between 1 and $N$
    Randomly pick $p$ samples from the $N$ available samples
    Compute the length of the MST of these samples, $L(p)$

Find the best least squares fit value of $a$ for
$L(p) = a\log(p) + \epsilon_p$
The optimal dimension $d$ is
$d = \text{round}(\frac{1}{1-a})$
```

We utilize the code in [89] to compute the length functional of the MST. The complexity of this step is $O(NlogN)$.

Step 5: Construct the d-dimensional embedding using MDS.

```
Compute $\mathbf{A}(i, j) = -\frac{1}{2}\mathbf{M}^2(i, j)$
Compute $\mathbf{B} = \mathbf{HAH}$
Compute the eigenvalues of $\mathbf{B}$;  $\mathbf{B} = \boldsymbol{\Gamma\Lambda\Gamma}$
Define  $\mathbf{Y} = \boldsymbol{\Gamma\Lambda}^{\frac{1}{2}}$
```

The low-dimensional mapping of the input sample points is given by the first d components of $\mathbf{Y}$. That is, $\boldsymbol{y}_{ik} = \mathbf{Y}(k, i)$ for $i = 1, \ldots, N$ and $k = 1, \ldots, d$. The complexity of this step is $O(nN^2)$, where n is the pixel count in each image. Here, $n = p \times p \times p \sim 128^3$. For number of samples $N \ll n$, MDS is computationally more feasible than PCA, which has a complexity of $O(n^2N)$.

Step 6: Following Remark 4.8, the low-dimensional region $\mathcal{A}$ that maps to the high-dimensional microstructural space $\mathcal{M}_S$ is given by the convex hull of the set of low-dimensional points $(\boldsymbol{y}_1, \ldots, \boldsymbol{y}_N)$. We utilize the Qhull program [90] to compute the convex hull of multidimensional data sets.

```
$\mathcal{A}$ = convex hull$(\boldsymbol{y}_1, \ldots, \boldsymbol{y}_N)$
```

3.5.3 Utilizing this reduced-order representation: Stochastic collocation

The above generated d-dimensional embedding is utilized as an input stochastic model for the solution of SPDEs. We utilize a sparse grid collocation strategy for constructing the stochastic solution [14]. The method essentially solves the problem at various points $\boldsymbol{\xi}$ on the stochastic space and constructs an interpolation based approximation to the stochastic solution. The sparse grid collocation strategy used utilizes piecewise multi-linear hierarchical basis functions as interpolation functions [14]. For a given set of stochastic collocation points $\boldsymbol{\xi}_i$, $i = 1, \ldots, M$, from $\mathcal{A}$, we find the corresponding images of these points (using the procedures detailed in Section 3.4.5) $\boldsymbol{x}_i = \mathcal{F}^{-1}(\boldsymbol{\xi}_i)$. These microstructural images are utilized as inputs (property maps) in the solution of the SPDEs.

Remark 5.1: In the stochastic collocation approach, the collocation points are usually given in the unit hypercube, i.e. $\boldsymbol{p} \in [0, 1]^d$. As a first step, this point $\boldsymbol{p}$ must be mapped to a corresponding point $\boldsymbol{\xi} \in \mathcal{A}$.

```
for $i = 1 : M$
    determine the collocation point $\boldsymbol{p}_i \in [0, 1]^d$
    compute the point $\boldsymbol{\xi}_i \in \mathcal{A}$
    compute $\mathbf{x}_i = \mathcal{F}^{-1}(\boldsymbol{\xi}_i)$
    solve the PDE using $\mathbf{x}_i$ as input
```

3.6 Illustrative example

In this section, we showcase the theoretical developments detailed in the previous sections with a realistic example.

3.6.1 Two-phase microstructures

The non-linear dimension reduction strategy is applied to construct a reduced-order model for the distribution of material in a two-phase metal-metal composite. The problem of interest is as follows:

Compute the PDFs of temperature evolution in a metal-metal composite microstructure when only limited statistics of the material distribution is known.

This topological uncertainty translates to uncertainties in the thermal diffusivity $\alpha(x)$ of the microstructure. For clarity of presentation, we divide the solution into multiple sections. 1) The first step is the extraction of topological statistics from the experimental image provided. These statistics are then utilized to reconstruct a large set of 3D microstructures $\{\mathbf{x}_i\},\ i = 1, \ldots, N$. 2) The next step is to construct the low-dimensional representation of the class of microstructures utilizing the samples $\{\mathbf{x}_i\},\ i = 1, \ldots, N$ in the input space. 3) The final step is to utilize the reduced-order representation of the microstructural topology (and hence, the thermal diffusivity coefficient) as an input stochastic model to solve for the evolution of the temperature statistics.

Data extraction and sample set construction

We start from a given experimental image of a microstructure. The image ($204\mu m \times 236\mu m$), shown in Fig. 3.10, is of a Tungstan-Silver composite [66]. This is a well characterized system, which has been used to test various reconstruction procedures [68, 67]. The first step is to extract the necessary statistical information from the experimental image. The image is cropped, deblurred and discretized. The volume fraction of silver is $p = 0.2$. The experimental two-point correlation is extracted from the image. The normalized two-point correlation ($g(r) = \frac{L_2(r)-p^2}{p-p^2}$), is shown in Fig. 3.11. The data extraction was performed in Matlab.

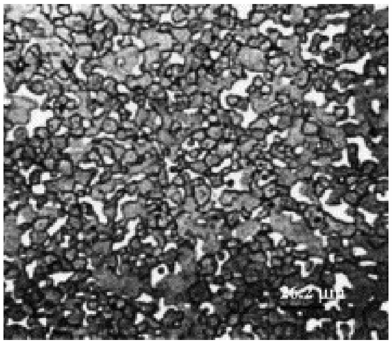

Figure 3.10: Experimental image of a two-phase composite (from [66]).

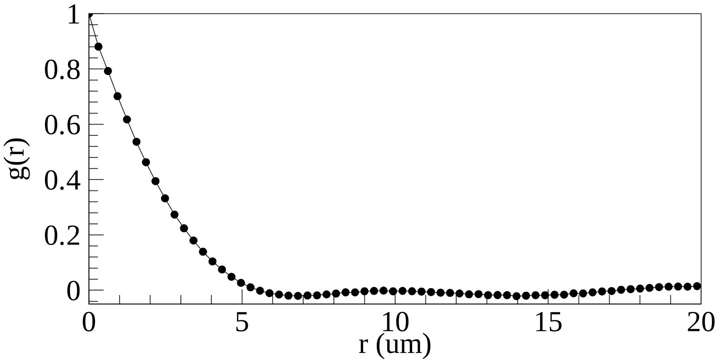

Figure 3.11: The two-point correlation function.

The next step is to utilize these extracted statistical relations (volume fraction and two-point correlation) to reconstruct a class of 3D microstructures. We utilize a statistics based reconstruction procedure based on Gaussian Random Fields (GRF). In this method, the 3D microstructure is obtained as the level cuts to a random field, $\varphi(\boldsymbol{x}),\ \boldsymbol{x} \in D$. The random field has a field-field correlation $\langle\varphi(0)\varphi(r)\rangle = \gamma(r)$. The statistics of the reconstructed 3D image can be matched to the experimental image by suitably modifying the field-field correlation function and the level cut values (see [68] for a detailed discussion). Following the work in [68], the GRF is assumed to satisfy a specified field-field correlation given by

$$\gamma(r) = \frac{e^{-r/\beta} - (r_c/\beta)e^{-r/r_c}}{1-(r_c/\beta)} \frac{\sin(2\pi r/d)}{2\pi r/d}, \tag{3.31}$$

where the field is characterized by the correlation length β, a domain scale d and a cutoff scale r_c. For a specific choice of (β, d, r_c), one can construct a microstructure from the resulting GRF. The (theoretical) two-point correlations corresponding to this reconstructed microstructures is computed. Optimal values of (β, d, r_c) are obtained by minimizing the error between the theoretical two-point correlation and the experimental two-point correlation. The theoretical two-point correlation corresponding to $(\beta, d, r_c) = (2.229, 12.457, 2.302)\mu m$ is plotted in Fig. 3.12.

Using the optimal parameters of the GRF (to match with the experimental data), realizations of 3D microstructure were computed. Each microstructure consisted of $65 \times 65 \times 65$ pixels. This corresponds to a size of $20\mu m \times 20\mu m \times 20\mu m$. One realization of the 3D microstructure reconstructed using the GRF is shown in Fig. 3.13.

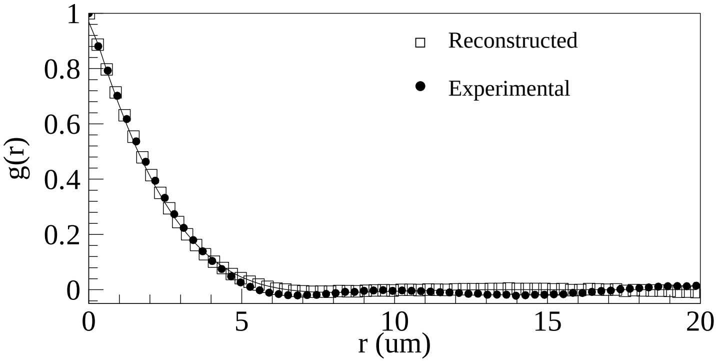

Figure 3.12: Comparison of the two-point correlation function from experiments and from the GRF.

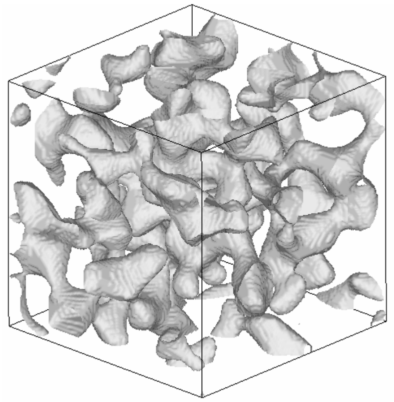

Figure 3.13: One instance (realization) of the two-phase microstructure.

Nonlinear dimension reduction and construction of the topological model

The GRF based reconstruction detailed above was used to generate a set of $N = 1000$ samples of two-phase microstructure. Each microstructure is represented as a $65 \times 65 \times 65$ pixel image. The three-point correlations of all these samples are calculated. The three-point correlation is easily computed as follows: for a given value of (a, b, c), randomly place triangles of side lengths a, b, c on the microstructure. Count the number of times all three vertices of the triangle lie on the same phase. $S_3(a, b, c)$ is the ratio of the number of such successful placements over the total number of tries. In our computations, we randomly place 500, 000 triangles to compute S_3 for each value of (a, b, c). The total computational time to reconstruct 1000 microstructures along with their S_3 was 30 minutes on 25 nodes of our in-house Linux cluster.

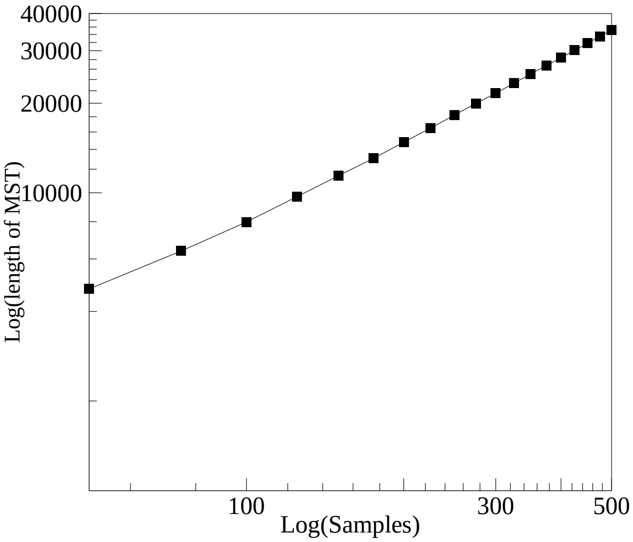

Figure 3.14: Plot of the length functional of the MST of the graph G for various sample sizes.

Based on the calculated S_3, the pairwise distance matrix $\mathbf{P}$ is computed. This took 6 minutes to compute on a 3.8*GHz* PC. From this, the geodesic distance matrix $\mathbf{M}$ and the graph G are computed. These are used to estimate the optimal dimensionality of the low-dimensional space by computing the length functional of the MST of the graph G. The Matlab code available at [89] was utilized. Fig. 3.14 plots the length functional of the MST of the graph G for various sample sizes. The optimal dimensionality of the low-dimensional set is related to the slope of this line (see Eq. (3.20)). The slope of the curve is computed using a simple least squares fit. The optimal dimensionality was estimated to be $d = 9$ ($a \sim 0.885$). The total computational time to estimate the dimensionality was 8 minutes on a 3.8*GHz* PC.

Multi Dimensional Scaling is performed using the geodesic distance matrix **M**. The 9 largest eigenvalues and their corresponding eigenvectors are used to represent the input samples. The low-dimensional region $\mathcal{A}$ is constructed as the convex hull of these $N(= 1000)$ 9-dimensional points ξ_i. This region coupled with the mappings developed in Section 3.4.5 define the reduced-order stochastic input model $\mathcal{F}^{-1} : \mathcal{A} \rightarrow \mathcal{M}_{S_2}$.

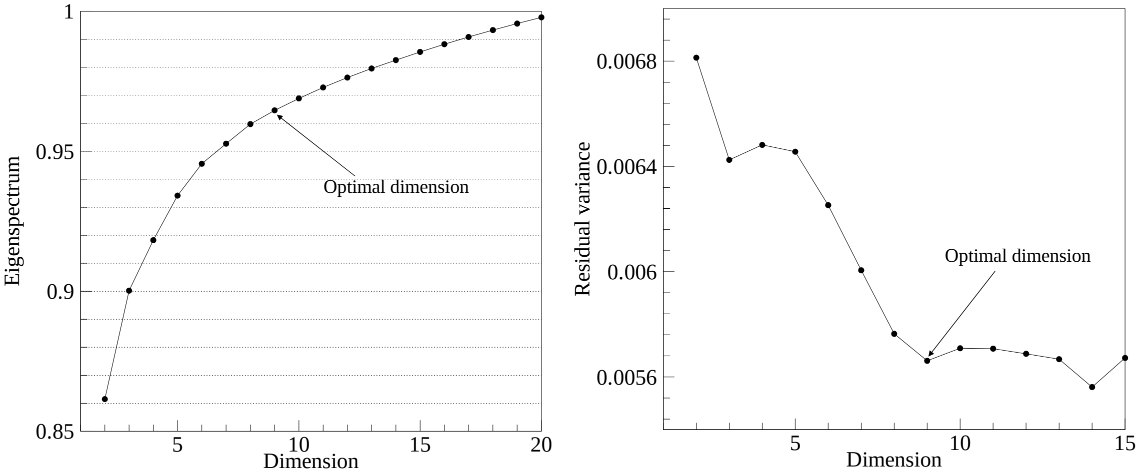

Figure 3.15: (Left) The cumulative eigenspectrum of the data, $\frac{\sum_{i=1}^{d}\lambda_i}{\sum_{i=1}^{N}\lambda_i}$. (Right) The residual variance for different dimensionalities of the region $\mathcal{A}$, computed from MDS.

Fig. 3.15 illustrates the potential difficulty in choosing the dimensionality of the region $\mathcal{A}$ based on simple variance errors (i.e. choose the value of d that accounts for 90% of the variance in the data). Fig. 3.15(a) plots the eigenspectrum of the computed eigenvalues of **B** ($\frac{\sum_{i=1}^{d}\lambda_i}{\sum_{i=1}^{N}\lambda_i}$). All dimensionalities beyond $d = 4$ account for over 90% of the variance in the data. Hence, there arises some ambiguity in simply choosing the dimensionality of the reduced mode based on this plot. Fig. 3.15(b) plots the residual variance of the low-dimensional representation for various dimensionalities. The residual variance measures the difference between the intrinsic manifold distance matrix, **M** and the pairwise Euclidian matrix, $\mathbf{D}_{\mathcal{A}}$, recovered from MDS (see Eq. 3.23) for various dimensionalities d. It is defined in terms of the element-wise correlation between the two matrices, $e = 1 - r^2(\mathbf{D}_{\mathcal{A}}, \mathbf{M})$, where r here is the standard linear correlation coefficient [91]. Notice that all the dimensions above $d = 8$ have fairly small variance, with $d = 14$ having the minimum. This ambiguity in choosing the dimensionality of the low-dimensional representation is overcome by using the ideas discussed in Section 3.4.3, resulting in an optimal dimensionality of $d = 9$.

Utilizing the model to solve a stochastic PDE: Diffusion in random heterogeneous media

The procedure detailed above results in the function $\mathcal{F}^{-1}$. $\mathcal{F}^{-1}$ is a mapping from a 9-dimensional space $\mathcal{A}$ to the space of microstructures $\mathcal{M}_{S_2}$. $\mathcal{F}^{-1}$ along with $\boldsymbol{\xi} \in \mathcal{A}$ serve as the stochastic input for the diffusion equation. A simple diffusion problem is considered (Eq. 3.13). A computational domain of $65 \times 65 \times 65$ is considered (this corresponds to a physical domain of $20\mu m \times 20\mu m \times 20\mu m$). The random heterogeneous microstructure is constructed as a $65 \times 65 \times 65$ pixel image. The steady-state temperature profile, when a constant temperature of 0.5 is maintained on the left wall and a constant temperature of -0.5 is maintained on the right wall, is evaluated. All the other walls are thermally insulated. The axis along which the temperature boundary conditions are imposed is denoted as the x-axis (left-right) while the vertical axis is the z-axis.

The construction of the stochastic solution is through sparse grid collocation strategies (Smolyak algorithm). A level 5 interpolation scheme is used to compute the stochastic solution in 9 dimensions. The stochastic problem was reduced to the solution of 26017 deterministic decoupled equations. Fifty

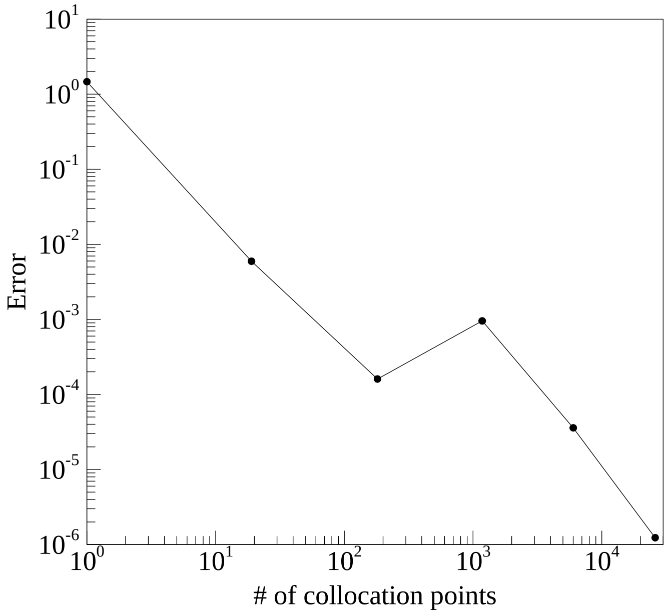

Figure 3.16: Reduction in the interpolation error with increasing number of collocation points.

nodes (each with two 3.8G CPUs) of our 64-node Linux cluster were utilized to solve these deterministic equations. These are dual core processors with hyperthreading capabilities thus each node was used to perform the computation for 4 such problems. The total computational time was about 210 minutes. Each deterministic problem involved the solution of a diffusion problem on a given microstructure using an 64×64×64 element grid (uniform hexahedral elements).

The reduction in the interpolation error with increasing depth of interpolation is shown in Fig. 3.16. The interpolation error is defined as the variation of the interpolated value of the function from the computed value ($e = max_{i=1:n_{no}}(|f - I(f)|)$, where n_{no} is the number of nodes). As the level of interpolation increases, the number of sampling points used to construct the stochastic solution increases [14]. Notice that there is a slight jump in the error going from an interpolation of depth 2 to depth 3. This is probably due to the presence of some highly localized fluctuations of the stochastic solution that is captured only when the depth of interpolation reaches 3. Nevertheless, the error reduction shown above follows the theoretical convergence estimates for using Smolyak based interpolation [14].

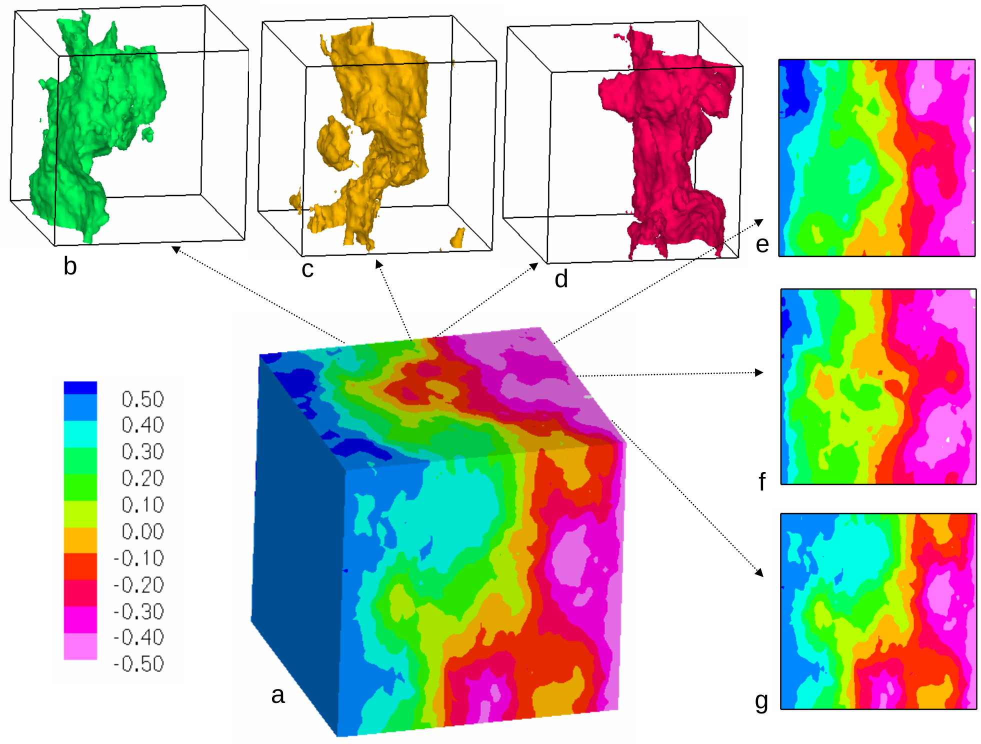

Figure 3.17: Steady-state mean temperature: (a) temperature contour, (b-d) temperature iso-surfaces, and (e-g) temperature slices.

The mean temperature is shown in Fig. 3.17. The figure plots iso-surfaces of temperatures −0.25 (Fig. 3.17(b)), 0.0 (Fig. 3.17(c)) and 0.25 (Fig. 3.17(d)). The figure also shows temperature slices at three different locations of the xz plane: $y = 0$ (Fig. 3.17(e)), $y = 8\mu m$ (Fig. 3.17(f)) and $y = 16\mu m$ (Fig. 3.17(g)).

The standard deviation and other higher-order statistics of the temperature variation are shown in Fig. 3.18. Fig. 3.18(a) plots standard deviation iso-surfaces. Figs. 3.18(d)–3.18(f) plot slices of the temperature deviation at three

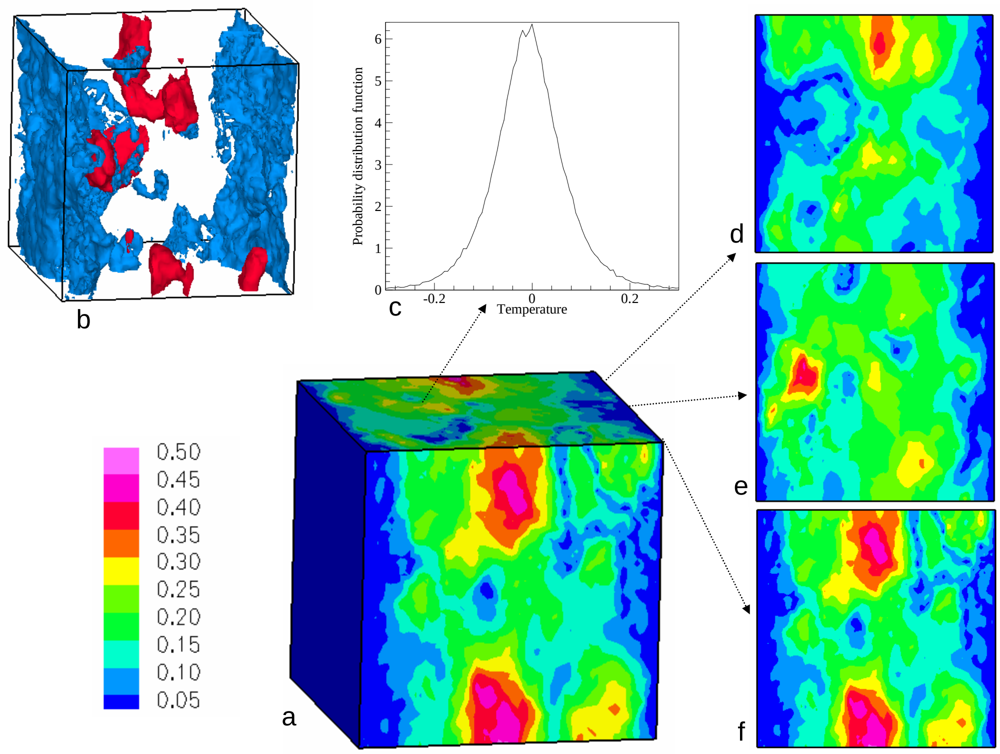

Figure 3.18: Standard deviation of temperature: (a) standard deviation contours, (b) standard deviation iso-surfaces, (c) temperature PDF at a point, and (d-f) standard deviation slices.

different planes $y = 0$, $y = 8\mu m$, $y = 16\mu m$, respectively. The standard deviation reaches 48% of the maximum temperature difference maintained. A point from a region of high-standard deviation ($A = (4, 4, 20)\mu m$) is chosen and the PDF of temperature at this point is determined. Fig. 3.18c plots the PDF for the point.

We conclude this section by making a few observations. The physical features of the topology variation will have an effect on the low-dimensional model. If the correlation length (of the two-point correlation) decreases the optimal dimensionality of the model will increase and vice versa. The model reduction strategy developed is data-driven: the transformation only converts the given finite input data set into a set of low-d points. In case the input data,

$\{\boldsymbol{x}_i\}$ all belong to a localized region of $\mathcal{M}_{S_2}$, the model reduction strategy framework will construct a low-dimensional parametrization of only this localized region. By increasing the amount of data utilized, one can make sure that the complete space, $\mathcal{M}_{S_2}$ is sampled, ensuring that the data-driven model reflects the variability in the complete space.

3.7 Conclusions

A non-linear model reduction technique for converting experimentally determined statistics into viable, realistic stochastic input models of property variability has been developed in the present work. The major advantages of the proposed developments are: it seamlessly meshes with any reconstruction method, directly converts samples into an equiprobable low-order model of the property, and is applicable to *any* property variation (for instance, property variation in polycrystalline materials, permeability variation in heterogeneous porous media, etc.).

The current developments borrow generously from ideas in image processing and psychology where the problem of manifold learning is frequently encountered. Ideas from differential geometry are employed to show the accuracy and asymptotic convergence of the reduced-order model. We showcase the framework developed to construct a realistic reduced-order stochastic model that describes the material and property variation in a two-phase microstructure (starting from an experimental image of the microstructure). We utilize this stochastic model as an input in the solution of a SPDE governing diffusion in random heterogeneous media. The solution provides an understanding of how uncertainty in the topology of the microstructure affects the evolution of a dependant variable (temperature).

The basic model reduction ideas envisioned in this work are not limited to generation of viable stochastic input models of property variations. This framework has direct applicability to problems where working in high-dimensional spaces is computationally intractable, for instance, in visualization of property evolution, extracting process-property maps in low-dimensional spaces, among others. Furthermore, the generation of a low-dimensional surrogate space has major ramifications in the optimizing of properties-processes and structures, making complicated operations like searching, contouring and sorting computationally much more feasible. These potentially exciting areas of application of the non-linear model reduction framework developed here offer fertile avenues of further research.

Different reduction techniques (for instance, locally linear embedding, kernel PCA, self organizing maps) can be incorporated into the general model reduction strategy formulated here. This is an area that is unexplored and could potentially result in very efficient, real time, data-driven, stochastic reduced-order model generation techniques. In addition to the importance of such models in process modeling of heterogeneous materials (polycrystals, composites, concrete, etc.), many other technological applications in modeling multiscale thermal/flow transport in geological media, soil contamination and reservoir engineering remain to be explored.

CHAPTER 4

ANALYSIS OF FLOW THROUGH HETEROGENEOUS RANDOM MEDIA: A STOCHASTIC MULTISCALE SYSTEM

4.1 Introduction

Thermal and hydrodynamic transport in random heterogeneous media are ubiquitous processes occurring in various scales ranging from the large scale (e.g. geothermal energy systems, oil recovery, geological heating of the earth's crust) to smaller scales (e.g. heat transfer through composites, polycrystals, flow through pores, inter-dendritic flow in solidification, heat transfer through fluidized beds). There has been increasing interest in reliably modelling and predicting the thermal and hydrodynamic behavior of such media. One of the challenging mathematical issues in the analysis of transport through heterogeneous random media is the multiscale nature of the property variations. Complete response evaluation involving full (fine-scale) spatial and temporal resolution simulations of multiscale systems is extremely expensive. Computational techniques have been developed that solve for a coarse-scale solution by defining an appropriate coarse-scale problem that captures the effect of the fine-scales [94]. The more popular techniques developed for such upscaling fall under the category of multiscale methods viz. the variational multiscale (VMS) method (operator upscaling) [95, 96, 97, 98, 99, 100], the heterogenous multiscale method [101, 102] and the multiscale finite element method [103, 104, 105, 106, 107]. Further related techniques are presented in [108, 109]. These computationally scalable techniques have resulted in the development of black box simulators that have been used with significant success in the solution of large scale transport problems in complex geometries.

The multiscale analysis of such systems inherently assumes that the complete, fine-scale variation of the permeability is known. This assumption limits the applicability of these frameworks since it is usually not possible to experimentally determine the complete structure of the media at the finest scale. In most cases, only a few statistical descriptors of the property variation or the property variation in small test regions can be experimentally determined. This limited information about the permeability necessitates viewing the permeability variation as a random field that satisfies certain statistical properties/correlations. This naturally results in describing the physical phenomena as stochastic partial differential equations (SPDEs) instead of partial differential equations (PDEs).

In the past decade, there has been tremendous progress in posing and solving SPDEs. Several techniques like Generalized Polynomial Chaos expansion [7, 8, 11, 12, 37, 39, 41], wavelet expansion and collocation based strategies [14, 16, 110, 111] have been developed to solve SPDEs. These techniques have been applied with significant success to solve single scale stochastic problems. In recent years, there has been significant interest in coupling deterministic multiscale methods with techniques in stochastic analysis to investigate critical multiscale systems in the presence of uncertainties.

There are two key questions that have to be sequentially answered to construct a stochastic multiscale framework that models transport phenomena only given limited information: (1) Techniques to convert/encode limited statistical information and/or sampled property values into a viable (stochastic) input model for the (multiscale) permeability variation and (2) Given this input multiscale stochastic model, techniques to solve the stochastic multiscale equations.

The basic idea to solve the stochastic multiscale set of equations is to extend deterministic multiscale methods to their stochastic analogues. Spectral strategies to pose and solve stochastic multiscale problems have been investigated by Xu [112] and Asokan and Zabaras [42]. Collocation based strategies have recently been developed in [20]. The key is to define appropriate ways to link the fine-scale (subgrid) stochastic variation with the coarse-scale stochastic variation of the dependent variables.

In the present work we are interested in analyzing flow through random heterogeneous media given limited statistical information about the multiscale permeability variation. We link stochastic analysis and multiscale methods to investigate this problem.

4.2 Problem definition

Fig. 4.1 shows a schematic of the problem of interest. Denote the domain as $\mathcal{D} \subset R^{n_{sd}}$, where n_{sd} is the number of spatial dimensions. The characteristic length scale of $\mathcal{D}$ is L. Denote the length scale of permeability fluctuation as l. In the problems that we are interested in solving the characteristic length of the domain is a couple of orders of magnitude larger than the characteristic length scale of the permeability fluctuations $l \ll L$.

We are interested in evaluating the pressure, p and velocity, $\boldsymbol{u}$ in the domain, $\mathcal{D}$. The variables $(\boldsymbol{u}(\boldsymbol{x}), p(\boldsymbol{x}))$ depend on the (multiscale) permeability distribution, $k(\boldsymbol{x})$ in the domain. However, the complete permeability distribution in un-

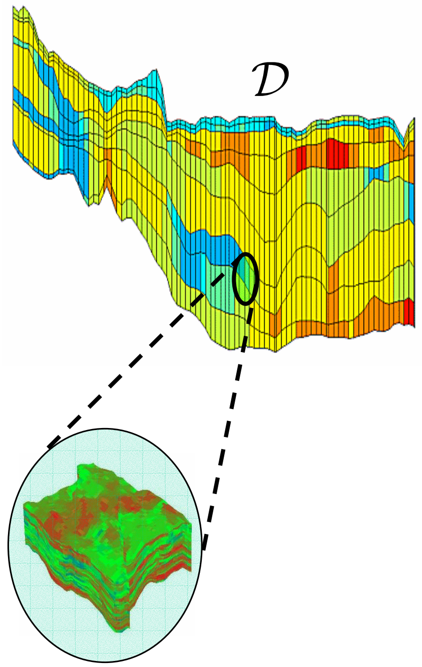

Figure 4.1: Schematic of the problem of interest.

known. Only some limited statistics and/or snapshots of the permeability are given. This limited information available to characterize the permeability necessitates assuming that the permeability is a realization of a random field. This is mathematically stated as follows: Let Ω be the space of all allowable permeability variations. This is our event space. Every point $k = \{k(\boldsymbol{x}, \omega), \forall \boldsymbol{x} \in \mathcal{D}, \omega \in \Omega\}$ in this space is equiprobable. Consequently, we can define a σ-algebra $\mathcal{F}$ and a corresponding probability measure $\mathcal{P} : \mathcal{F} \to [0, 1]$ to construct a complete probability space $(\Omega, \mathcal{F}, \mathcal{P})$ of allowable permeability. To make this abstract description amenable to numerical simulation, a finite-dimensional approximation/representation [44] of this abstract set is necessary. Various data-driven strategies to represent the set Ω as a finite-dimensional function are discussed in Chapter 3. The stochastic permeability is represented as

$$k(\boldsymbol{x}, \omega) \equiv k(\boldsymbol{x}, Y_1, \ldots, Y_N) \equiv k(\boldsymbol{x}, \boldsymbol{Y}), \tag{4.1}$$

where $Y_1, \ldots, Y_N$ are uncorrelated random variables.

The pressure and velocity are characterized by the following set of equations

$$\nabla \cdot \boldsymbol{u}(\boldsymbol{x}, \boldsymbol{Y}) = f(\boldsymbol{x}), \tag{4.2}$$

$$\boldsymbol{u}(\boldsymbol{x}, \boldsymbol{Y}) = -k(\boldsymbol{Y}) \nabla p(\boldsymbol{x}, \boldsymbol{Y}), \tag{4.3}$$

where the source/sink term $f(\boldsymbol{x})$ is taken to be deterministic. Furthermore, f is also assumed to not have a multiscale character. These assumptions are simply to make the subsequent developments clear. It is fairly straightforward to account for uncertainties in f as well as to analyze the effects of a multiscale f [113].

The basic idea is to solve the problem on a coarse spatial discretization, $\mathcal{D}^c$, while taking into account the fine-scale variation in the stochastic permeability. In the next section, we detail a stochastic extension to the variational multiscale method to solve this problem. The stochastic multiscale formulation is based on the multiscale formulation detailed in the papers by Juanes et al. [113] and Arbogast et al. [114]. The augmentation of the deterministic multiscale formulation to its stochastic counterpart mainly depends on two straightforward developments: (a) defining the appropriate stochastic function spaces (both finite- and infinite-dimensional), and (b) defining the appropriate localization assumptions. For brevity of presentation, we will concentrate on these two aspects. The interested reader in referred to [113, 114] for other details.

4.3 Stochastic variational multiscale formulation

For the problem to be physically relevant, we assume that the stochastic permeability satisfies some conditions, particularly:

Assumption 1: k is positive and uniformly coercive:

$$\begin{gathered}\exists\, k_{min}, k_{max} \in (0, \infty) : \\ \mathcal{P}(\omega \in \Omega : k(\boldsymbol{x}, \omega) \in [k_{min}, k_{max}], \forall \boldsymbol{x} \in \mathcal{D}) = 1.\end{gathered} \tag{4.4}$$

As stated in Section 4.2, the abstract representation of $k(., \omega)$ in Ω is replaced by a more tractable finite-dimensional representation $k(., \boldsymbol{Y})$, with $\boldsymbol{Y} \in \Gamma \subset R^N$. Corresponding to the probability measure $\mathcal{P} : \mathcal{F} \rightarrow [0, 1]$, we denote the equivalent probability measure $\rho : \Gamma \rightarrow [0, 1]$.

The governing equations for the velocity and pressure given in the mixed form are as follows:

$$k^{-1}\boldsymbol{u} + \nabla p = 0, \tag{4.5}$$

$$\nabla \cdot \boldsymbol{u} = f. \tag{4.6}$$

The above constitutive and conservation equations are supplemented with the following boundary conditions

$$p = p_o \;\; on \;\; \partial\mathcal{D}_p, \tag{4.7}$$

$$\boldsymbol{u} \cdot \boldsymbol{n} = u_o \;\; on \;\; \partial\mathcal{D}_u. \tag{4.8}$$

Without loss of generality, we assume that the boundary conditions are deterministic and that the Neumann condition is homogeneous [113], $u_o = 0 \;\; on \;\; \partial\mathcal{D}_u$.

The next step is to introduce the appropriate function spaces in which the velocity and pressure lie. In contrast to their deterministic counterparts, the velocity and pressure defined here are stochastic processes. Most dependent variables one encounters in stochastic analysis are usually random processes [45, 115, 116, 117] that are defined in product spaces. These variables (for instance $p(\boldsymbol{x}, \boldsymbol{Y})$) usually have one structure in the stochastic space $p(., \boldsymbol{Y})$ and another in the physical space $p(\boldsymbol{x}, .)$. The numerical analysis/approximation [45, 115] of such functions can be performed by defining the appropriate *tensor product spaces*. The interested reader is referred to [45, 115] for insightful discussions on the definitions of these product spaces. Following [45, 115], we define appropriate function spaces that encode variations of the function in the physical domain $\mathcal{D}$ and in the stochastic space Γ.

Remark 3.1: We will consider stochastic functions that belong to $\mathcal{S}$, the space of all square integrable functions, with measure $\rho(\boldsymbol{Y})$. Given a deterministic function space A, its stochastic counterpart is the tensor product space $\mathcal{A} \equiv \mathcal{S} \otimes A$.

We introduce the following tensor product function spaces:

$$
\begin{aligned}
\mathcal{W} &\equiv \mathcal{S} \otimes W \equiv L^2(\Gamma) \otimes L^2(\mathcal{D}), \;\text{ with, }\; (p, p) \equiv \|p\|^2_{\mathcal{W}} := \int_\Gamma d\rho(\boldsymbol{Y}) \int_{\mathcal{D}} p^2 dx, && (4.9)\\
\mathcal{H} &\equiv \mathcal{S} \otimes H \equiv L^2(\Gamma) \otimes H(div, \mathcal{D}), \;\text{ with, }\; (\boldsymbol{u}, \boldsymbol{u}) \equiv \|\boldsymbol{u}\|^2_{\mathcal{H}} := \int_\Gamma d\rho(\boldsymbol{Y}) \int_{\mathcal{D}} \boldsymbol{u} \cdot \boldsymbol{u} dx, && (4.10)\\
\mathcal{V} &= \{\boldsymbol{u} : \boldsymbol{u} \in \mathcal{H}, \boldsymbol{u}(., \boldsymbol{Y}) \cdot \boldsymbol{n} = 0 \;\; on \;\; \partial\mathcal{D}_u, \;\; \forall\, \boldsymbol{Y} \in \Gamma\}. && (4.11)
\end{aligned}
$$

The problem defined by Eqs. (4.5) and (4.6) along with the boundary conditions Eqs. (4.7) and (4.8) can be written in mixed variational form: Find $(\boldsymbol{u},\ p) \in \mathcal{V} \times \mathcal{W}$ such that

$$
\begin{aligned}
(\boldsymbol{v}, k^{-1}\boldsymbol{u}) - (\nabla \cdot \boldsymbol{v}, p) &= -\langle \boldsymbol{v} \cdot \boldsymbol{n}, p_o \rangle, \quad \forall \boldsymbol{v} \in \mathcal{V}, && (4.12)\\
(w, \nabla \cdot \boldsymbol{u}) &= (w, f), \quad \forall w \in \mathcal{W}, && (4.13)
\end{aligned}
$$

where $\langle f, g \rangle$ is defined as $\int_\Gamma d\rho(\boldsymbol{Y}) \int_{\partial\mathcal{D}_p} f g d\boldsymbol{x}$.

Variational multiscale approach: The exact solution $\boldsymbol{u}$ is assumed to be made up of contributions [98] from two different (spatial) scales namely, the coarse-scale solution $\boldsymbol{u}_c(\boldsymbol{x}, .)$ that can be resolved using a coarse (spatial) mesh and a subgrid solution $\boldsymbol{u}_f(\boldsymbol{x}, .)$:

$$\boldsymbol{u} = \boldsymbol{u}_c + \boldsymbol{u}_f, \;\; p = p_c + p_f. \tag{4.14}$$

This additive sum decomposition induces a similar decomposition for the spatial part of the fine-scale tensor-product function spaces into a direct sum of a coarse-scale and a subgrid tensor-product function spaces.

$$\mathcal{W} = \mathcal{W}_c \oplus \mathcal{W}_f, \;\; \mathcal{H} = \mathcal{H}_c \oplus \mathcal{H}_f, \;\; \mathcal{V} = \mathcal{V}_c \oplus \mathcal{V}_f. \tag{4.15}$$

The main idea is to develop models for characterizing the effect of the subgrid solution $\boldsymbol{u}_f(\boldsymbol{x}, .)$ on the coarse-scale solution and to subsequently derive a modified coarse-scale formulation that only involves $\boldsymbol{u}_c(\boldsymbol{x}, .)$. The additive decomposition provides a way of splitting the fine-scale problem given by Eqs. (4.12)-(4.13) into a coarse-scale problem and a subgrid problem. Testing against the coarse-scale test functions results in the coarse-scale variational problem: Find $(\boldsymbol{u}_c, \; p_c) \in \mathcal{V}_c \times \mathcal{W}_c$ such that

$$\begin{aligned} (\boldsymbol{v}_c, k^{-1}(\boldsymbol{u}_c + \boldsymbol{u}_f)) - (\nabla \cdot \boldsymbol{v}_c, (p_c + p_f)) &= -\langle \boldsymbol{v}_c \cdot \boldsymbol{n}, p_o \rangle, \quad \forall \boldsymbol{v}_c \in \mathcal{V}_c, && (4.16) \\ (w_c, \nabla \cdot (\boldsymbol{u}_c + \boldsymbol{u}_f)) &= (w_c, f), \quad \forall w_c \in \mathcal{W}_c. && (4.17) \end{aligned}$$

Similarly testing against the subgrid test functions results in the subgrid variational problem: Find $(\boldsymbol{u}_f, \; p_f) \in \mathcal{V}_f \times \mathcal{W}_f$ such that

$$\begin{aligned} (\boldsymbol{v}_f, k^{-1}(\boldsymbol{u}_c + \boldsymbol{u}_f)) - (\nabla \cdot \boldsymbol{v}_f, (p_c + p_f)) &= -\langle \boldsymbol{v}_f \cdot \boldsymbol{n}, p_o \rangle, \quad \forall \boldsymbol{v}_f \in \mathcal{V}_f, && (4.18) \\ (w_f, \nabla \cdot (\boldsymbol{u}_c + \boldsymbol{u}_f)) &= (w_f, f), \quad \forall w_f \in \mathcal{W}_f. && (4.19) \end{aligned}$$

Note that both the coarse-scale variational equations Eqs. (4.16)-(4.17) as well as the subgrid variational equations Eqs. (4.18)-(4.19) contain coarse and subgrid variations in the dependent variable ($\boldsymbol{u}_c, p_c; \; \boldsymbol{u}_f, p_f$). The key is to solve

Eqs. (4.18)-(4.19) for $\boldsymbol{u}_f$ and construct a functional representation of the subgrid variation, $\boldsymbol{u}_f$ and p_f *in terms of the coarse-scale variation*, $\boldsymbol{u}_c$:

$$\boldsymbol{u}_f = \Phi(\boldsymbol{u}_c), \quad p_f = \Psi(\boldsymbol{u}_c). \tag{4.20}$$

This representation can be subsequently used to remove explicit dependence of $\boldsymbol{u}_f$ and p_f in Eqs. (4.16)-(4.17). The key problem is now to solve Eqs. (4.18)-(4.19). But these equations are defined over the complete global domain, $\mathcal{D}$. Solving the subgrid problem on the global domain is equivalent to solving the fine-scale problem itself. To make the problem computationally tractable, some localization assumptions have to be made to convert this global subgrid problem into a set of local subgrid problems [113].

Finite element approximation spaces: Before defining the localization assumptions, the finite element approximation spaces at the fine-scale and coarse-scale are first defined. As stated before (Remark 3.1), the stochastic function spaces are simply tensor product spaces of $\mathcal{S}$ with the corresponding deterministic spaces.

Fine-scale approximation spaces: Let $\mathcal{V}_h$ and $\mathcal{W}_h$ be finite-dimensional subspaces of the spatial part of the corresponding continuum spaces $\mathcal{V}$ and $\mathcal{W}$. That is

$$\mathcal{W}_h = \mathcal{S} \otimes W_h, \quad \mathcal{V}_h = \mathcal{S} \otimes V_h. \tag{4.21}$$

Note that W_h and V_h should satisfy the discrete inf-sup condition [118]. Consider a partition, $\mathcal{T}_h$ of the domain $\mathcal{D}$ into non-overlapping elements e_i, $\mathcal{T}_h = \bigcup_{i=1}^{N_h} e_i$, where N_h is the number of elements of the grid. Following [113], define also the skeleton of the partition, $\mathcal{SP}_h = \bigcup_{a=1}^{M_h} \gamma_a$, where M_h is the number of element faces denoted by γ_a. The partition $\mathcal{T}_h$ is denoted as the fine-grid, on which the fine-scale permeability is defined. The deterministic finite element approximation space for the velocity, V_h is taken to be the lowest-order Raviart-Thomas [119, 113] space, $RT_0(\mathcal{T}_h)$, and the deterministic finite element approximation space for the fine scale pressure, W_h is taken to be the space of piece-wise constants on the fine mesh, $P_0(\mathcal{T}_h)$.

Coarse-scale approximation spaces: Consider a coarse-scale partition of the domain, $\mathcal{D}$. Denote this partition as $\mathcal{T}_c = \bigcup_{i=1}^{N_c} E_i$. Denote by $\mathcal{SP}_c = \bigcup_{a=1}^{M_c} \Lambda_a$ the associated skeleton of the coarse-scale discretization. Here, N_c is the number of coarse-elements E_i and M_c is the number of coarse-element faces denoted by Λ_a. Following [113], we also assume for simplicity that the partitions $\mathcal{T}_h$ and $\mathcal{T}_c$ – the fine- and coarse-grid, respectively – are nested, conforming, and consist of rectangular elements. Since $\mathcal{W}_h = \mathcal{S} \otimes P_o(\mathcal{T}_h)$, choose the coarse-scale pressure as belonging to the space of piecewise constant functions, $\mathcal{W}_c^h = \mathcal{S} \otimes \mathcal{P}_o(\mathcal{T}_c)$. The choice of the coarse-scale velocity approximation spaces now has to be compatible with this choice of the pressure approximation. In the analogous deterministic developments, the two choices for such spaces were the lowest order Raviart-Thomas space (used in [113]) and the Brezzi-Douglas-Marini space of order 1 (used in [96]). We choose to utilize the stochastic analog to the lowest order Raviart-Thomas space in the current work. We can now associate the coarse-scale velocity with the lowest-order Raviart-Thomas space, $RT_0(\mathcal{T}_c)$ as:

$$\mathcal{V}_c^h = \mathcal{S} \otimes V_c^h, \quad V_c^h = \{\boldsymbol{u}_c : \boldsymbol{u}_c = \sum_{a=1}^{M_c} \boldsymbol{N}_a^c u_a^c, \;\; u_a^c = 0 \;\; \forall \Lambda_a \in \partial \mathcal{D}_u\}, \tag{4.22}$$

where $\mathcal{V}_c^h$ is the finite-dimensional approximation to the coarse-scale continuum space $\mathcal{V}_c$. Here, $\boldsymbol{N}_a^c$ is the RT_0 basis function associated with face Λ_a, and u_a^c is the corresponding degree of freedom (the integrated coarse-flux through Λ_a [113]). The coarse-scale pressure approximation is piecewise constant on the coarse-mesh, $P_0(\mathcal{T}_c)$:

$$\mathcal{W}_c^h = \mathcal{S} \otimes W_c^h, \quad W_c^h = \{w_c : w_c = \sum_{i=1}^{N_c} \phi_i^c w_i^c\}, \tag{4.23}$$

where $\mathcal{W}_c^h$ is the finite-dimensional approximation to the coarse-scale continuum space $\mathcal{W}_c$. Here, ϕ_i^c is the pressure basis function for the coarse-element i, which is equal to one in element E_i and zero in all other elements. w_i^c is the corresponding pressure degree of freedom (the average pressure in coarse-element E_i).

Subgrid-scale approximation spaces: The subgrid-scale velocities have to accurately mimic the fine-scale velocities. To ensure this, they are restricted to belong to the lowest-order Raviart-Thomas space on the fine grid *within each coarse-element* [113]. Denote by $E_{i,h} = \mathcal{T}_h(E_i)$ the fine grid defined over the coarse element E_i. The subgrid-scale velocity field defined on each coarse element satisfies the condition

$$\begin{aligned} V_{f,i}^h &\subset RT_0(E_{i,h}), \quad (4.24)\\ \mathcal{V}_{f,i}^h &= \mathcal{S} \otimes V_{f,i}^h, \quad (4.25) \end{aligned}$$

where $\mathcal{V}_{f,i}^h$ is the finite-dimensional approximation to the subgrid-scale continuum space $\mathcal{V}_f$, constrained to a coarse element E_i. The elements of $\mathcal{V}_{f,i}^h$ can naturally be extended to all of $\mathcal{D}$ by zero. The global subgrid velocity space can then be defined as the direct sum of the subgrid spaces over the coarse elements

$$\mathcal{V}_f^h = \bigoplus_{i=1}^{N_c} \mathcal{V}_{f,i}^h. \tag{4.26}$$

Similarly, the subgrid pressure space is restricted to belong to the space of piecewise constant functions on each coarse element

$$\begin{aligned} W_{f,i}^h &\subset P_0(E_{i,h}), \quad (4.27)\\ \mathcal{W}_{f,i}^h &= \mathcal{S} \otimes W_{f,i}^h, \quad (4.28) \end{aligned}$$

where $\mathcal{W}^h_{f,i}$ is the finite-dimensional approximation to the subgrid-scale continuum space $\mathcal{W}_f$, constrained to a coarse element E_i. The elements of these spaces are extended to zero functions to the entire spatial domain [113], $\mathcal{D}$, and the subgrid pressure space is defined as

$$\mathcal{W}^h_f = \bigoplus_{i=1}^{N_c} \mathcal{W}^h_{f,i}. \tag{4.29}$$

Localization Assumptions: Having defined the appropriate finite element approximation spaces, we now move to the problem of reducing the global subgrid problem (defined by Eqs. (4.18)-(4.19)) into a set of local subgrid problems defined over the coarse elements E_i.

The key localization assumption in the construction of the multiscale framework is to ensure that the approximation is locally conservative at both scales [113]. This implies that the discrete version of the conservation equation is satisfied on each element in the coarse and fine grids. Furthermore, we also assume that this condition is satisfied *not in a distributed sense, but for each stochastic realization (i.e. point-wise in stochastic space)*. This leads to the following condition

$$(w_c, \nabla \cdot \boldsymbol{u}_c)_{E_i} = (w_c, f)_{E_i}, \tag{4.30}$$

where $(.,.)_{E_i}$ is the corresponding inner product defined over the coarse-element E_i. This condition (in its strong, point-wise form) is equivalent to [113]

$$\nabla \cdot \boldsymbol{u}_c = \Pi_c f, \tag{4.31}$$

where $\Pi_c f$ is the projection of the source/sink term onto the space W_c of piecewise constants on the coarse grid. As stated in the beginning of this section, we assume that the sourse/sink function does not display a multiscale nature, i.e.

it is equal to its projection on the space of coarse-scale pressures ($f = \Pi_c f$). Substituting Eq. (4.30) into the coarse-scale conservation equation Eq. (4.17) results in

$$(w_c, \nabla \cdot \boldsymbol{u}_f)_{E_i} = 0, \ \forall E_i \in \mathcal{T}_c. \tag{4.32}$$

Since w_c is constant in each coarse element, using the divergence theorem and the assumption that this condition is valid point-wise in stochastic space, results in the following condition on the subgrid velocities in each coarse element

$$\int_{\partial E_i} \boldsymbol{u}_f \cdot \boldsymbol{n} d\Lambda = 0, \quad \forall E_i \in \mathcal{T}_c. \tag{4.33}$$

Eq. (4.33) is the essential condition [113] that guarantees mass conservation at both scales and allows for the localization of the subgrid problem. This localization assumption converts the global subgrid problem into a set of local Neumann problems with boundary conditions defined by Eq. (4.33). Furthermore, the subgrid test function $\boldsymbol{v}_f$ must satisfy $\boldsymbol{v}_f \cdot \boldsymbol{n} = 0$ on ∂E_i which results in the following constraint

$$(\nabla \cdot \boldsymbol{v}_f, p_c)_{E_i} = 0, \ \forall E_i \in \mathcal{T}_c. \tag{4.34}$$

Finally, we define the space of subgrid pressure $\mathcal{W}_f^h$ as the orthogonal complement of $\mathcal{W}_c^h$ in $\mathcal{W}_h$ (i.e. $(w_f, w_c) = 0$). Now, since $\mathcal{W}_C^h = \text{div } \mathcal{V}_c^h$, this results in an additional constraint

$$(\nabla \cdot \boldsymbol{v}_c, p_f)_{E_i} = 0, \ \forall E_i \in \mathcal{T}_c. \tag{4.35}$$

The subgrid problem: Using the localization assumption Eqs. (4.33), (4.34), (4.35) the localized subgrid problem can be defined as follows: For each coarse element, $E_i = 1, \ldots, N_c$, find $(\boldsymbol{u}_f, p_f) \in \mathcal{V}_{f,i}^h \times \mathcal{W}_{f,i}^h$, such that

$$
\begin{aligned}
(\boldsymbol{v}_f, k^{-1}\boldsymbol{u}_f)_{E_i} - (\nabla \cdot \boldsymbol{v}_f, p_f)_{E_i} &= -(\boldsymbol{v}_f, k^{-1}\boldsymbol{u}_c)_{E_i}, \quad \forall \boldsymbol{v}_f \in \mathcal{V}^h_{f,i}, \qquad (4.36)\\
(w_f, \nabla \cdot \boldsymbol{u}_f)_{E_i} &= (w_f, f - \nabla \cdot \boldsymbol{u}_c)_{E_i}, \quad \forall w_f \in \mathcal{W}^h_{f,i}. \qquad (4.37)
\end{aligned}
$$

Since $f = \nabla \cdot \boldsymbol{u}_c$ (assumption that the sourse/sink exhibits no multiscale character), the RHS of Eq. (4.37) is identically zero. The interested reader is referred to [113] for detailed discussion of the case when the source/sink function displays multi-scale behavior where deterministic analysis is provided. It is straightforward to extend those arguments to the stochastic case. Note that given $\boldsymbol{u}_c$ and the appropriate boundary conditions, the above problem has a unique solution for the subgrid velocity and pressure. The global subgrid scale solution $(\boldsymbol{u}_f, p_f)$ is obtained by patching together the solutions on each coarse element.

Multiscale basis functions: Eqs. (4.36)-(4.37) represent the subgrid scale velocity and pressure in terms of the coarse-scale velocity. Recollect that the coarse-scale velocity is represented in terms of the RT_0 basis functions (Eq. (4.22)) and the M_c degrees of freedom as $\boldsymbol{u}_c = \sum_{a=1}^{M_c} \boldsymbol{N}^c_a u^c_a$. We therefore represent the subgrid scale variation in terms of the finite number of coarse-scale degrees of freedom [113] as

$$
\boldsymbol{u}_f = \sum_{a=1}^{M_c} \boldsymbol{N}^f_a u^c_a, \quad p_f = \sum_{a=1}^{M_c} \phi^f_a u^c_a. \qquad (4.38)
$$

The above equations transform the problem of finding the function $\Phi(\boldsymbol{u}_c)$ and $\Psi(\boldsymbol{u}_c)$ (defined in Eq. (4.20)) into finding the subgrid scale basis functions $(\boldsymbol{N}^f_a, \phi^f_a)$ associated with each coarse-scale degree of freedom. For computational efficiency, the multiscale basis function representing the multiscale velocity is defined as the sum of the coarse-scale and subgrid-scale components as

$$\boldsymbol{u} \;=\; \sum_{a=1}^{M_c} (\boldsymbol{N}_a^c + \boldsymbol{N}_a^f) u_a^c = \sum_{a=1}^{M_c} \boldsymbol{N}_a^{ms} u_a^c. \tag{4.39}$$

The multiscale basis functions are associated with each coarse-scale interface Λ_a. The multiscale basis functions are constructed based on defining the Greens function to the subgrid Eqs. (4.36)-(4.37) [98, 99]. In the context of deterministic mixed multiscale methods, various authors have constructed these multiscale basis functions [96, 106, 107]. We utilize the deterministic definition of the multiscale basis functions used in [120, 113] to define the stochastic multiscale basis functions. The multiscale basis function is the solution to a flow problem restricted to a pair of adjacent coarse elements that share a common coarse interface. The course terms are specified in such a way that the flow through the interface is identically one (based on the Green's function idea). It is straightforward to extend this definition of the multiscale basis function to the case when the permeability is stochastic.

The stochastic multiscale basis functions $(\boldsymbol{N}_a^{ms}, \phi_a^{ms})$ for the interface Λ_a (which is shared by the coarse elements E_i and E_j) are the solution to the following stochastic local problem:

$$k^{-1}\boldsymbol{N}_a^{ms} + \nabla \phi_a^{ms} \;=\; 0, \quad in \;\; E_i \cup E_j, \tag{4.40}$$

$$\boldsymbol{N}_a^{ms} \cdot \boldsymbol{n} \;=\; 0, \quad on \;\; \partial(E_i \cup E_j), \tag{4.41}$$

$$\nabla \cdot \boldsymbol{N}_a^{ms} \;=\; \begin{cases} +k(\boldsymbol{x}, .)/\int_{E_i} k(\boldsymbol{x}, .)d\boldsymbol{x}, & \text{if } \boldsymbol{x} \in E_i, \\ -k(\boldsymbol{x}, .)/\int_{E_j} k(\boldsymbol{x}, .)d\boldsymbol{x}, & \text{if } \boldsymbol{x} \in E_j. \end{cases} \tag{4.42}$$

The coarse-scale problem: We next turn to the coarse-scale variational equations. Based on the localization assumptions Eqs. (4.33)-(4.35), the coarse-scale variational equations Eqs. (4.16)-(4.17) reduce to the following: Find $(\boldsymbol{u}_c, p_c) \in$

$\mathcal{V}_c^h \times \mathcal{W}_c^h$, such that

$$(\boldsymbol{v}_c, k^{-1}\boldsymbol{u}_c) + (\boldsymbol{v}_c, k^{-1}\boldsymbol{u}_f) - (\nabla \cdot \boldsymbol{v}_c, p_c) = -\langle \boldsymbol{v}_c \cdot \boldsymbol{n}, p_o \rangle, \quad \forall \boldsymbol{v}_c \in \mathcal{V}_c^h, \tag{4.43}$$

$$(w_c, \nabla \cdot \boldsymbol{u}_c) = (w_c, f), \quad \forall w_c \in \mathcal{W}_c^h. \tag{4.44}$$

Following [113], the problem is expressed in its equivalent symmetric form by defining the stochastic multiscale velocity space, $\mathcal{V}_{ms}^h$ and stochastic multiscale pressure spaces $\mathcal{W}_{ms}^h$ as follows:

$$\mathcal{V}_{ms}^h = \mathcal{S} \otimes V_{ms}^h, \;\; V_{ms}^h = \{\boldsymbol{u}_{ms} : \boldsymbol{u}_{ms} = \sum_{a=1}^{M_c} \boldsymbol{N}_{ms}^c u_a^c, \;\; u_a^c = 0 \;\; \forall \Lambda_a \in \partial \mathcal{D}_u\}, \tag{4.45}$$

$$\mathcal{W}_{ms}^h = \mathcal{S} \otimes W_{ms}^h, \;\; W_{ms}^h = \{w_{ms} : w_{ms} = \sum_{i=1}^{N_c} \phi_i^c (w_i^c + \sum_a \tilde{\phi}_a^{ms} u_a^c)\}, \tag{4.46}$$

where $\tilde{\phi}_a^{ms} = \phi_a^{ms} - \frac{1}{|E_i|}\int_{E_i} \phi_a^{ms} d\boldsymbol{x}$.

With this definition of the finite-dimensional function spaces, the stochastic coarse-scale problem can be written as: Find $(\boldsymbol{u}_{ms}, p_{ms}) \in \mathcal{V}_{ms}^h \times \mathcal{W}_{ms}^h$, such that

$$(\boldsymbol{v}_{ms}, k^{-1}\boldsymbol{u}_{ms}) - (\nabla \cdot \boldsymbol{v}_{ms}, p_{ms}) = -\langle \boldsymbol{v}_{ms} \cdot \boldsymbol{n}, p_o \rangle, \quad \forall \boldsymbol{v}_{ms} \in \mathcal{V}_{ms}^h, \tag{4.47}$$

$$(w_{ms}, \nabla \cdot \boldsymbol{u}_{ms}) = (w_{ms}, f), \quad \forall w_c \in \mathcal{W}_c^h. \tag{4.48}$$

Once the coarse-scale variables are solved, the fine-scale velocity and pressure can be reconstructed (if necessary) by resorting to the additive decomposition Eq. (4.14). The subgrid part is obtained by a linear combination of the coarse-scale fluxes and the subgrid scale basis functions.

The stochastic multiscale framework: The abstract framework to solve the stochastic multiscale problem defined by Eqs. (4.2)-(4.3) is given in Fig. 4.2.

As seen in Fig. 4.2, the key steps involved are

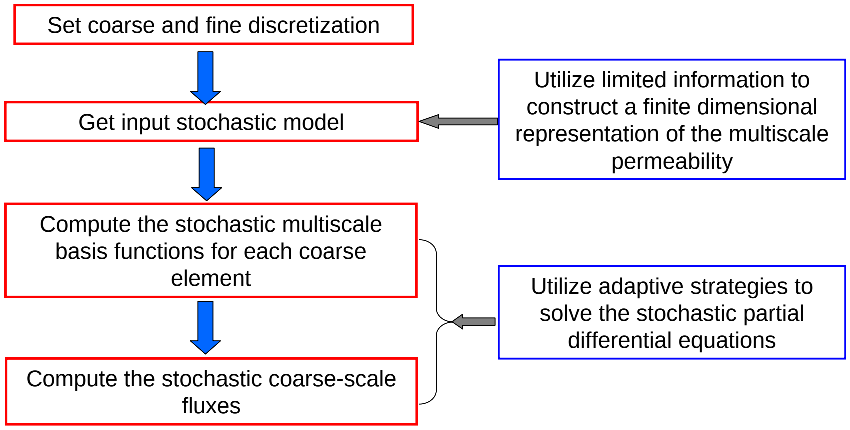

Figure 4.2: The stochastic multiscale framework.

- From limited data determine the fine-scale stochastic permeability. This requires data driven strategies to construct viable finite-dimensional representation of the stochastic permeability. Different techniques are discussed in Chapter. 3.
- Find the stochastic multiscale basis functions for each coarse element interface by solving Eqs. (4.40)-(4.42).
- Use these multiscale basis functions to solve for the stochastic coarse-scale velocities and pressure given by Eqs. (4.47)-(4.48). Adaptive techniques to solve the above set of SPDEs are discussed in Section 3.5.3.

4.4 The complete algorithm

The complete schematic of the stochastic multiscale procedure is illustrated in Fig. 4.3. The data-driven strategies (discussed in Chapter. 3) convert the limited information available into a plausible, realistic stochastic representation of the fine-scale permeability variation. The adaptive sparse grid collocation strategy is used to construct the stochastic multiscale basis functions over all the coarse elements. Following this, the stochastic coarse-scale equations are solved for the coarse-scale stochastic pressure and velocity.

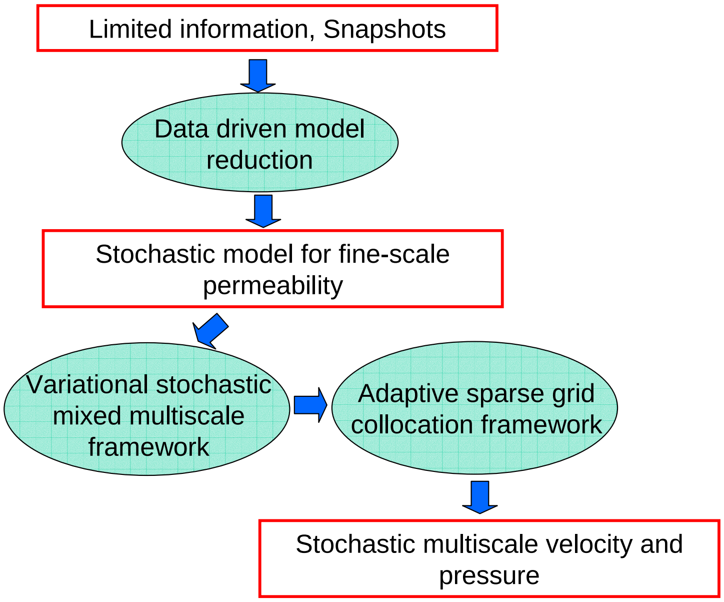

Figure 4.3: Schematic of the developed stochastic multiscale framework.

4.5 Numerical examples

In this section, we apply the complete stochastic analysis framework- from data-driven model generation, the stochastic variational mixed multiscale formulation to the adaptive solution of the resulting SPDEs. In the first example, we compare the effect of uncertainties in the small scale permeability variations and the effect of uncertainties in large scale geological features on the flow characteristics in a domain. In the second example, we look at the effect of localized uncertainties in permeability and how they propagate into the complete domain.

4.5.1 Effect of uncertainties at different scales

The schematic of the domain of interest is shown in Fig. 4.4. The region is part of an outcrop (where extensive measurements of permeability have been performed [124]) in Lawyer Canyon in Texas. The domain of interest is a square of length 200 ft. Flow is driven by an injection well at the left bottom corner of the domain and a production well at the top right corner. There is a low-permeability fault running across the domain. Limited information about the spatial variation in the fine-scale permeability is available in the form of semi-variograms and mean permeability (Fig. 4.5). Furthermore, the exact location and characteristics of the fault are unknown. Hence both the fine-scale permeability variation as well as the large-scale fault features have to be considered to be stochastic.

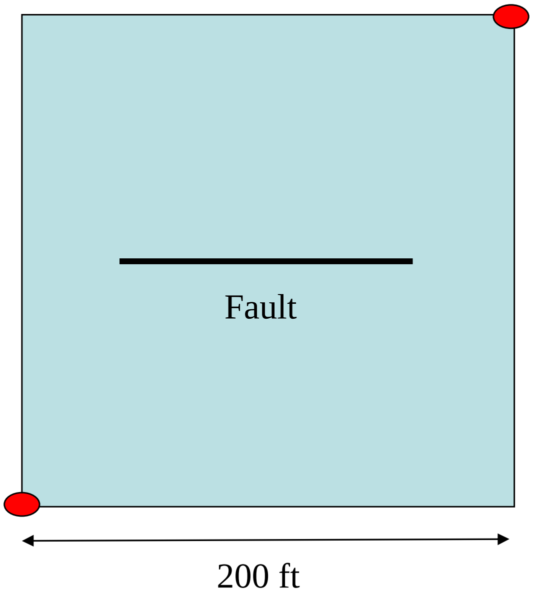

Figure 4.4: Schematic of the domain. A fault runs across the middle of the domain.

Effect of stochastic fine-scale permeability: We first investigate the effect of the stochastic fine-scale permeability keeping the location of the fault fixed. The fault is assumed to originate at (40, 100) and have a length of 100 feet and a width of 20 feet. A reduced model for the fine-scale permeability is constructed from the limited statistics available. Since in this case, the correlation structure of the permeability variation is available, we utilize the KL expansion to construct a viable stochastic model.

The two-point correlation is extracted and the KL expansion is performed. Fig. 4.6 (right) plots the first 40 eigenvalues constructed from the KL expansion. Note the logarithmic scale used. The first 25 eigenvalues represent about 95% of the total information. The KL expansion is truncated to 25 terms and this generates a 25-dimensional input stochastic model for the fine-scale permeability.

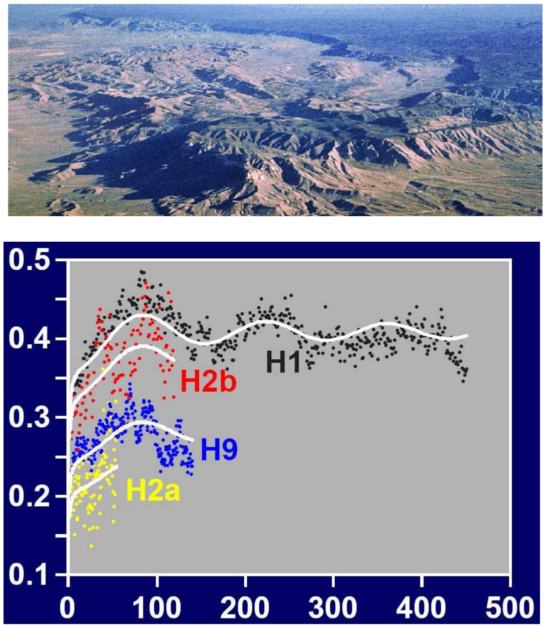

Figure 4.5: The Lawyer Canyon in Texas, where extensive measurements of permeability was made. Data available includes the semi-variograms of the permeability.

Three eigenvectors utilized in the KL expansion are shown in Fig. 4.7. Note

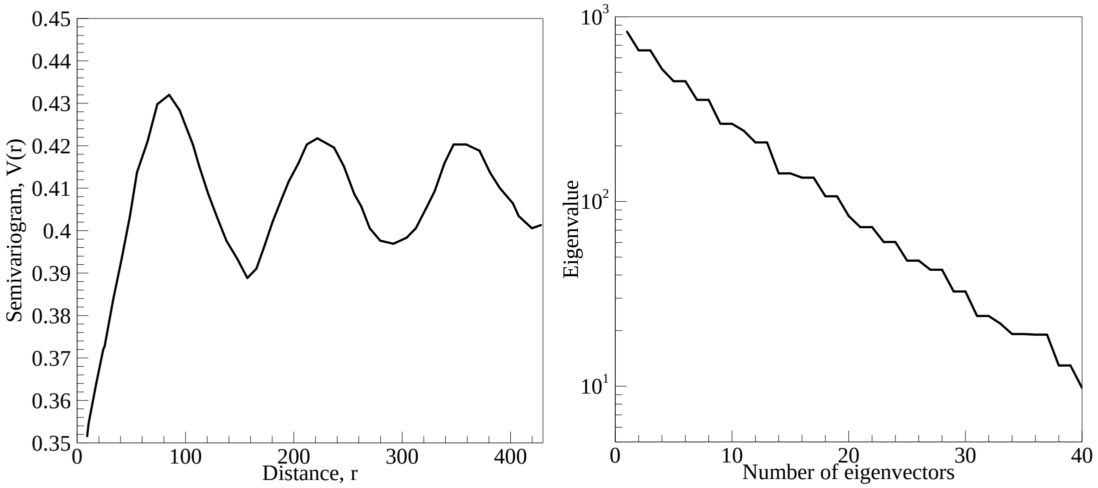

Figure 4.6: (left) Experimental semi-variogram of permeability. (right) The KL expansion of the correlation structure.

that the eigenvectors are in fact eigenvectors of the log-permeability field.

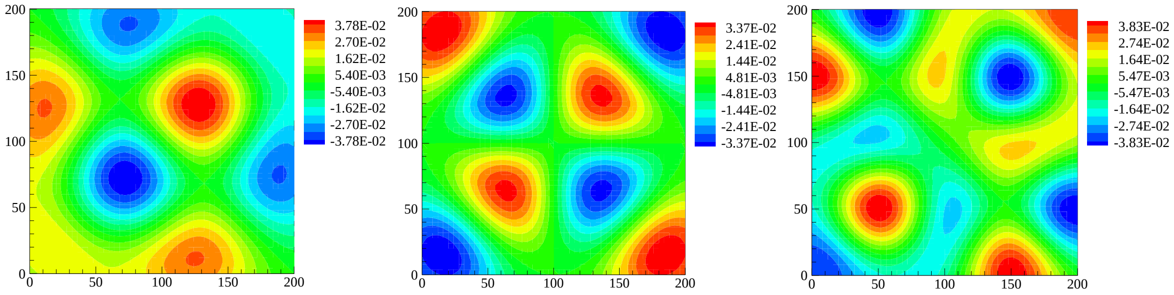

Figure 4.7: Three eigenvectors constructed from the KL expansion.

Fig. 4.8 shows two extreme realizations of the log-permeability field constructed utilizing the KL model. Note the close to 7 orders of magnitude variation in the permeability variation in these realizations.

The fine-scale permeability is given as 100 × 100 fineblocks in the domain. Aggressive upgridding is utilized and a coarse-scale discretization of 10 × 10 is utilized in the stochastic variational mixed multiscale framework. The 100-fold coarse-graining results in the representation of the system by only 320 upscaled

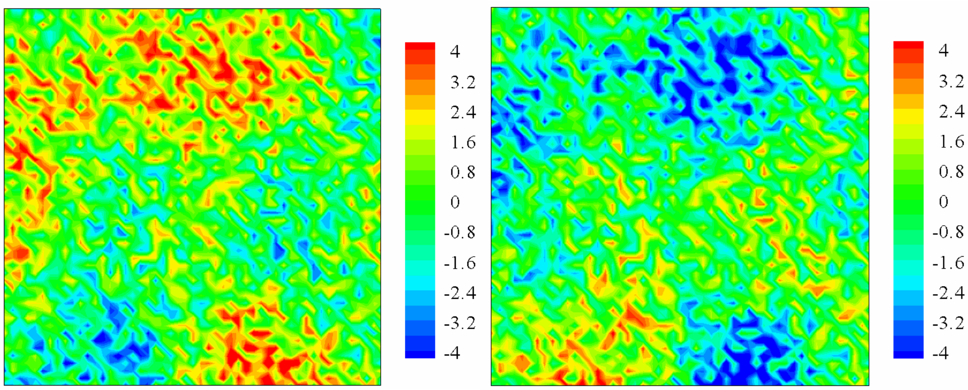

Figure 4.8: Two extreme realizations of the log-permeability generated from the KL expansion.

coarse variables.

30 nodes of our local Linux cluster (corresponding to 120 processors) was utilized. The total computational time was about 96 hours to solve this 25 + 2 (stochastic + spatial domain) dimensional problem. Fig. 4.9 (left) plots the convergence of the stochastic pressure (mean and standard deviation) with increasing number of collocation points, while Fig. 4.9 (right) plots the convergence of the stochastic *x*-direction flux with increasing number of collocation points. For the same depth of interpolation about 2.9×10^9 collocation points would have been required using conventional sparse grid collocation.

Fig. 4.10 plots the mean values of the coarse-scale pressure and *x*-direction flux. Note that the pressure is stratified around the region where the permeability fault is located.

Fig. 4.11 plots the standard deviation of the stochastic coarse-scale pressure and *x*-direction flux. The low-permeability fault leads in preferential flow around the fault. This leads to stratification of pressure around the fault as well as negligible flow. This is clearly seen as the very small standard deviation in

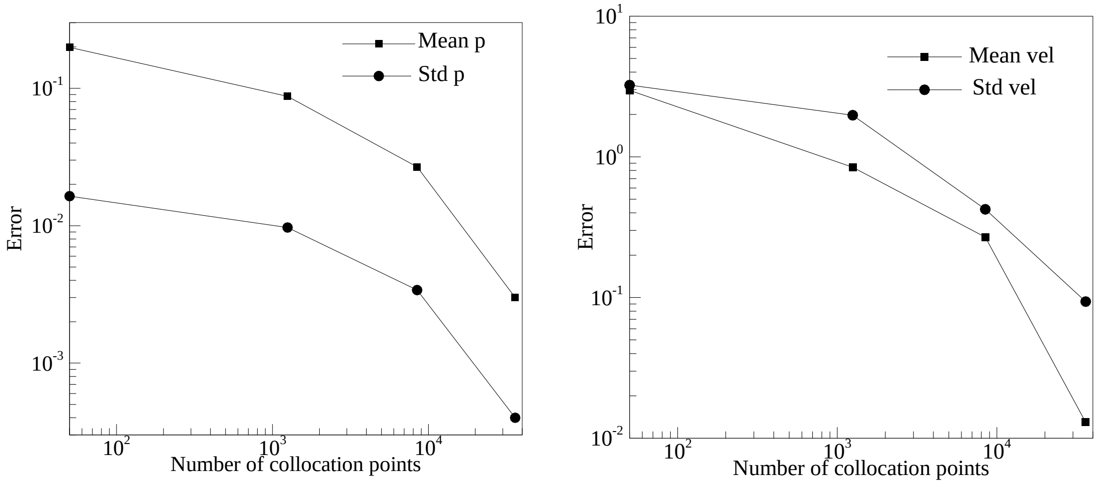

Figure 4.9: Convergence of the stochastic solution (mean and standard deviation) with increasing number of collocation points. (left) Stochastic coarse-scale pressure, (right) Stochastic coarse-scale *x*-direction flux.

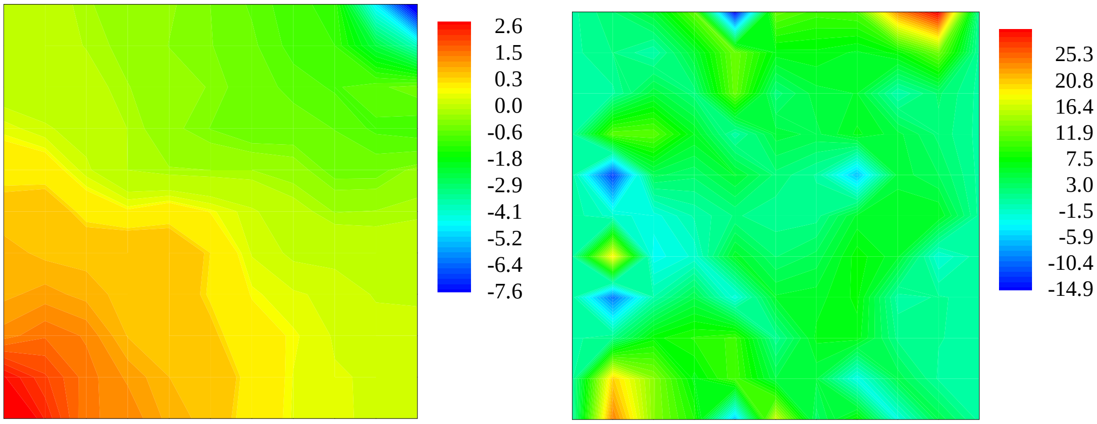

Figure 4.10: Mean stochastic coarse-scale solution. (left) Coarse-scale pressure, (right) Coarse-scale *x*-direction flux.

pressure in the middle of the domain where the fault is located. Furthermore, this results in a large variation in flux around the permeability fault as can be seen in Fig. 4.11 (right).

To check the accuracy of the stochastic solution, we perform comparison with the stochastic solution constructed using Monte-Carlo sampling strate-

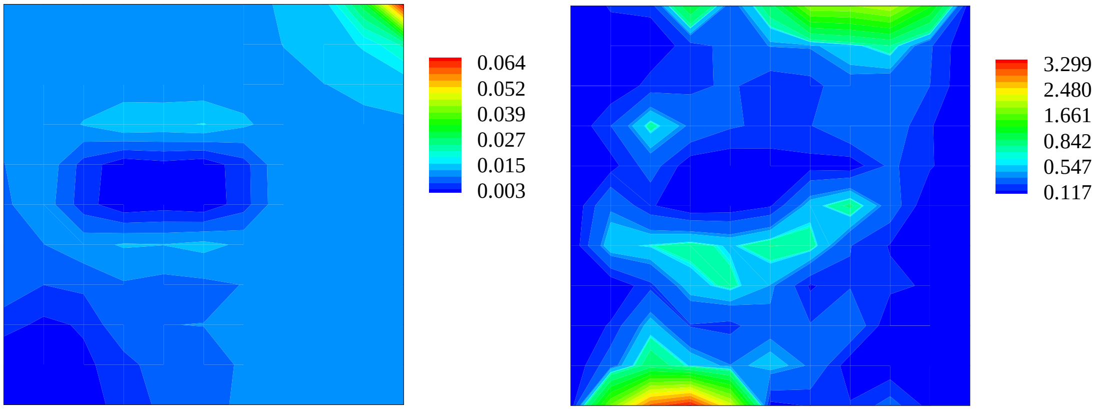

Figure 4.11: Standard deviation of the stochastic coarse-scale solution. (left) Coarse-scale pressure, (right) Coarse-scale *x*-direction flux.

gies. 10^6 samples were utilized to compute the statistics using the Monte Carlo method. This took about 900 hours using 30 nodes of our in-house Linux cluster. Fig. 4.12 plots the difference between the mean values of the coarse-scale pressure and *x*-direction flux computed from the two methods.

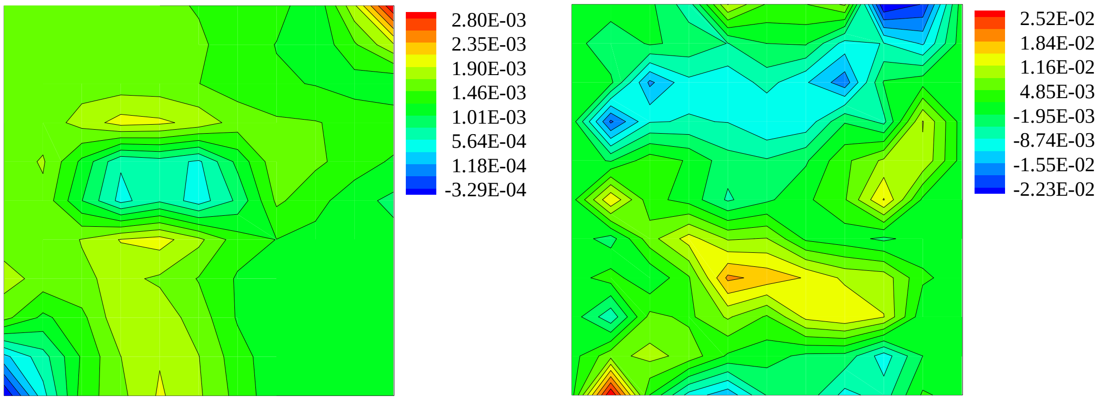

Figure 4.12: Difference in the mean value of the stochastic solutions using the adaptive sparse grid strategy and Monte Carlo sampling. (left) Mean pressure, (right) Mean *x*-direction flux.

Notice the difference in the mean pressure is very close to zero close to the injection well as well as on the permeability fault. On the other hand, since the flow will preferentially try to avoid the fault (resulting in the largest deviation around this region), there will be high variability in the *x*-direction flux immediately above and below the permeability fault. This leads to the largest error occurring here as seen clearly in Fig. 4.12. This is also clearly illustrated in Fig. 4.13 which plots the difference between the standard deviation of the coarse-scale pressure and *x*-direction flux computed from the two methods.

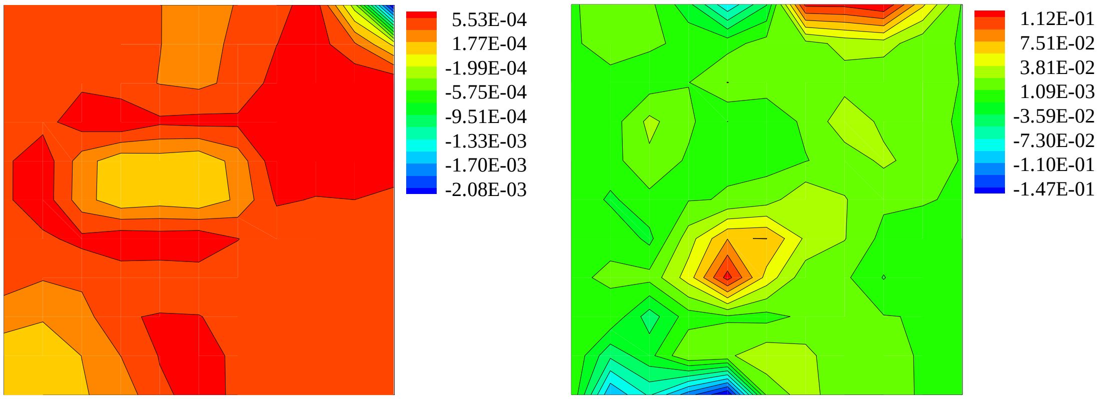

Figure 4.13: Difference in the standard deviation of the stochastic solutions using the adaptive sparse grid strategy and Monte Carlo sampling. (left) Standard deviation in pressure, (right) Standard deviation in the *x*-direction flux.

Fig. 4.14 plots streamlines based on the mean coarse-scale velocity distribution in the domain. The streamlines preferentially circumvent the permeability barrier.

From the stochastic solution, the probability distribution function of the coarse-scale *x*-direction flux is plotted at two spatial locations $(120, 40)$ and $(180, 160)$. The PDFs are plotted in Fig. 4.15. PDFs of coarse-scale pressure (not shown) also exhibited similar trends. The fine-scale stochastic permeability essentially caused a ‘smearing’ of the coarse-scale pressure and velocity fluxes.

Effect of uncertainty in large-scale permeability barrier: Next we focus on the effects of uncertainty in the location of the permeability barrier on the

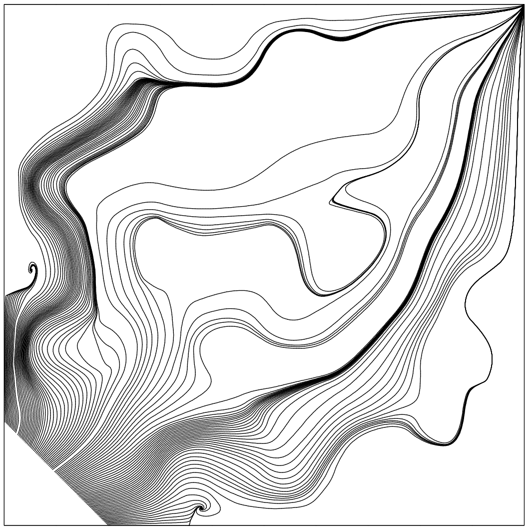

Figure 4.14: Streamlines drawn on the mean stochastic coarse-scale velocity.

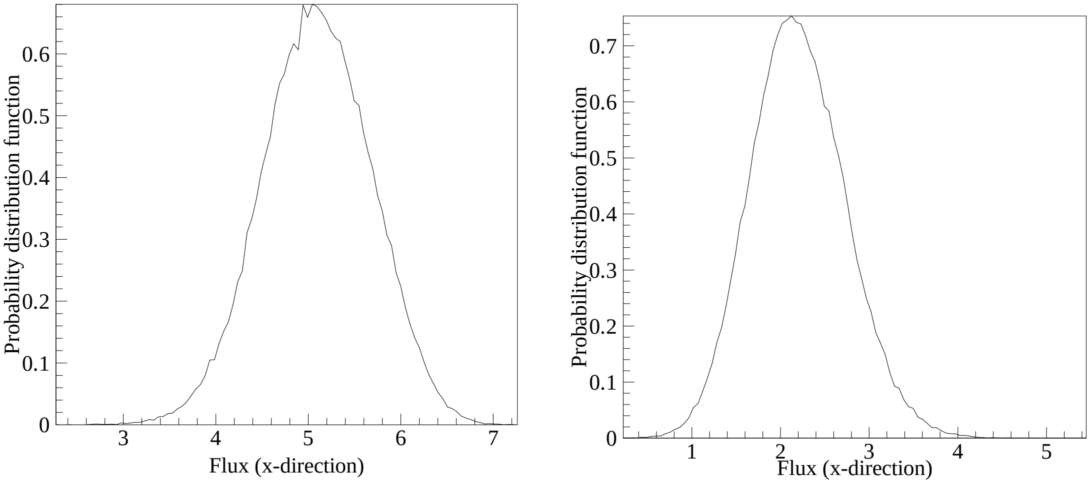

Figure 4.15: Probability distribution functions of the coarse-scale flux (*x*-direction) for two points in the domain.

coarse-scale stochastic pressure and velocity flux. We set the fine-scale permeability variation to its mean value and utilize the same 100-fold coarse-grained discretization as in the previous problem. We assume that there is 10% uncertainty in the location, length and width of the permeability barrier. This is quantified by 4 independent uniform random variables, (Y_1, Y_2, Y_3, Y_4), on the domain

$[-1, 1]$ as

$$\begin{aligned} x_l &= (0.2 + 0.05Y_1) * 200, \\ y_l &= (0.5 + 0.05Y_2) * 200, \\ L_{barrier} &= (0.5 + 0.05Y_3) * 200, \\ W_{barrier} &= (0.1 + 0.05Y_4) * 200, \end{aligned}$$

where (x_l, y_l) is the start position of the barrier, and $L_{barrier}$, $W_{barrier}$ are the length and width of the barrier, respectively. The variational stochastic mixed multiscale framework is utilized to solve this problem. 40 nodes of our local Linux cluster (corresponding to 160 processors) is utilized to solve the problem. The total computational time was about 240 minutes.

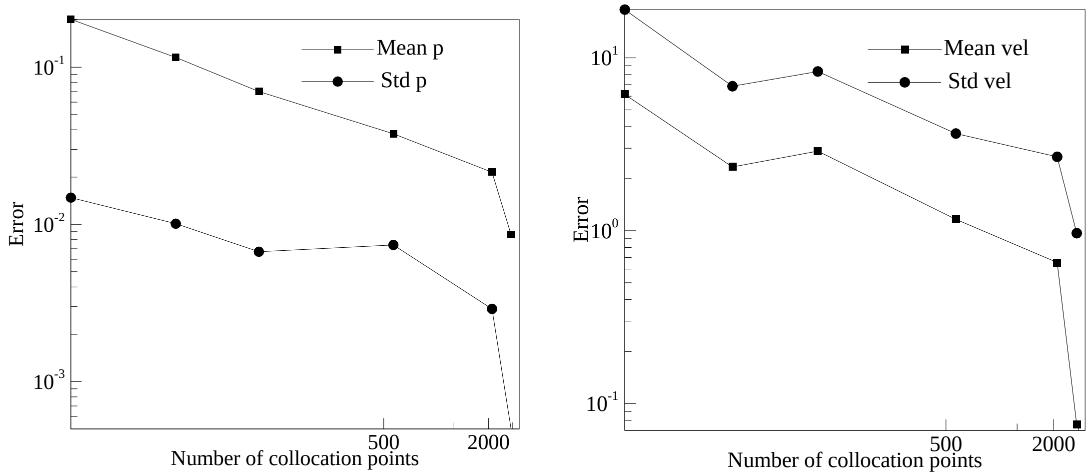

Figure 4.16: Convergence of the stochastic solution (mean and standard deviation) with increasing number of collocation points. (left) Stochastic coarse-scale pressure, (right) Stochastic coarse-scale x-direction flux.

Fig. 4.16 (left) plots the convergence of the stochastic pressure with increasing number of collocation points, while Fig. 4.16 (right) plots the convergence of the stochastic x-direction flux with increasing number of collocation points.

For the same depth of interpolation about 8000 collocation points would have been required using conventional sparse grid collocation. The adaptive sparse grid strategy sampled the 4D stochastic space anisotropically with the random dimension corresponding to the *x*-location of the permeability barrier being the most sensitive dimension.

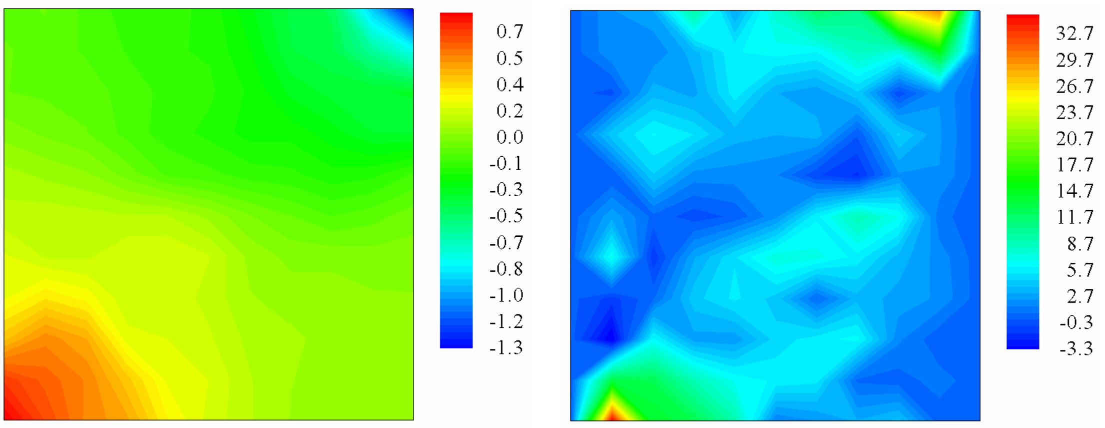

Figure 4.17: Mean contours of the stochastic coarse-scale solution. (left) Coarse-scale pressure, (right) Coarse-scale *x*-direction flux.

Fig. 4.17 plots the mean contours of the stochastic coarse-scale pressure and flux in the *x*-direction. The effects of the fine-scale variation in the structure of permeability is visible in the uneven pressure contours near the injection and production wells. Furthermore, the pressure is essentially uniform close to the middle of the domain where the permeability barrier lies. This is also seen in Fig. 4.17 (right), where most of the flow circumvents the location of the fault. This is even more clearly seen in the streamlines drawn on the mean coarse-scale velocity field as shown in Fig. 4.18.

Fig. 4.19 plots the standard deviation contours of the coarse-scale stochastic pressure and *x*-direction flux. As expected, most of the deviation in the pressure occurs close to the region of the permeability fault. Interestingly, most of the

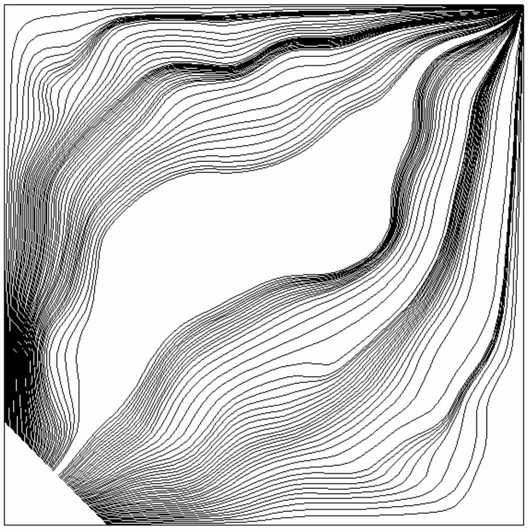

Figure 4.18: Streamlines drawn on the mean stochastic coarse-scale velocity.

large deviation region is 'downstream' of the location of the uncertainty– along the direction of flow. This is also seen in Fig. 4.19 (right) where the region of large standard deviation is on either side of the permeability barrier and extends along the flow direction downstream towards the production well on the top right.

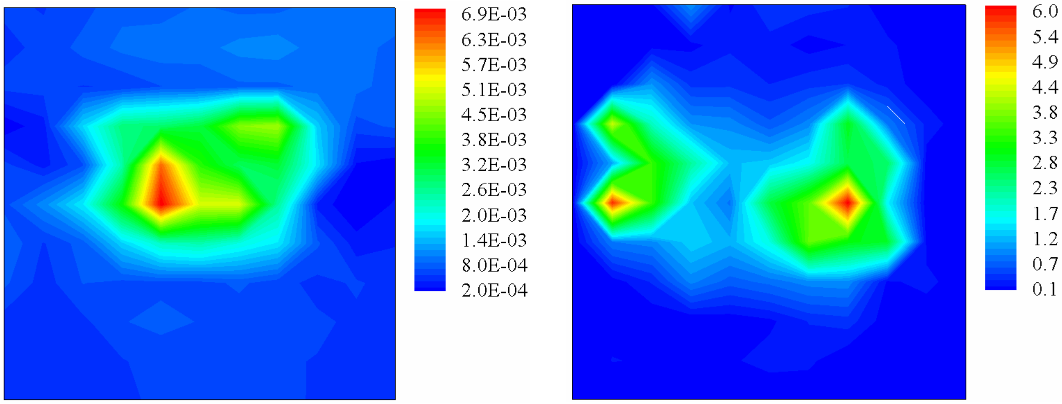

Figure 4.19: Standard deviation of the stochastic coarse-scale solution. (left) Coarse-scale pressure, (right) Coarse-scale *x*-direction flux.

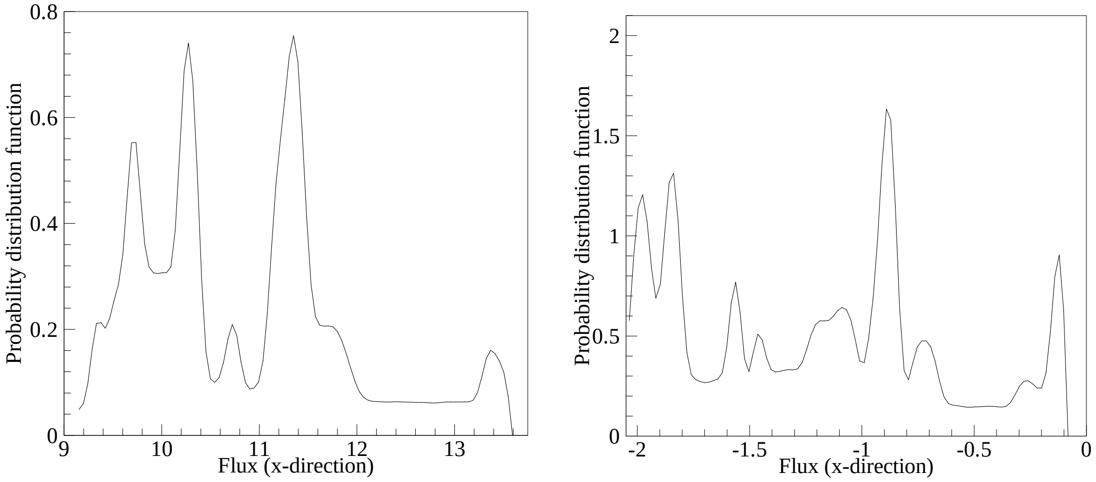

Figure 4.20: Probability distribution functions of the coarse-scale flux (x-direction) for two points in the domain.

From the stochastic solution, the probability distribution function of the coarse-scale x-direction flux is plotted at two spatial locations. The first point $(120, 40)$ has a relatively large standard deviation in the flux, while the second point $(100, 60)$ has a smaller standard deviation. The PDFs are plotted in Fig. 4.20. Notice that the PDFs at both points have several peaks (in contrast with the previous case) pointing to the possibility of mode shifts existing. In particular, Fig. 4.20 (right) is the PDF of a point that lies very close to the permeability barrier and it clearly shows up to 10 distinct peaks. It appears that small variations in the location of the peak results in significant changes in the flow patterns leading to the multi-modal structure of the PDF.

We investigate this possibility by reducing the problem to its most sensitive stochastic dimension. As stated earlier, the adaptive sparse grid collocation algorithm preferentially refines the stochastic solution along regions of steep variations and discontinuities. Most of the refinement proceeded along the dimension that characterized the uncertainty in the x-location of the permeability

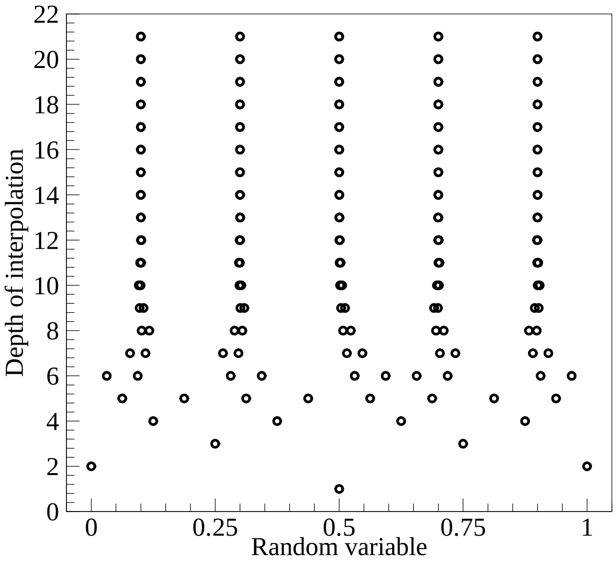

Figure 4.21: The refinement of the adaptive sparse grid. Each row of points represents the refinement at a particular level of interpolation. The interpolation starts at the bottom.

barrier (i.e. Y_1). We solved a problem with this as the only input stochastic variable. Fig. 4.21 plots the evolution of the adaptive grid. Notice that after the 8-th level of interpolation, most of the refinement is concentrated at 5 points. This implies the definite existence of steep gradients or discontinuities around these points in stochastic space. This is clearly seen in Fig. 4.22, where the PDF of the coarse-scale flux in the x-direction is plotted at two spatial points. The PDF in both cases consist of 5 sharp peaks.

In Fig. 4.23, we illustrate this mode shift behavior by plotting two realizations of the coarse-scale stochastic flux (x-direction). These two realizations correspond to two points in stochastic space that are separated by 1% (Y_1 = 0.295, 0.305). This corresponds to a mode-shift located at $Y_1 = 0.30$ as seen in Fig. 4.21. The flow structure close to the permeability barrier is significantly different for the two cases.

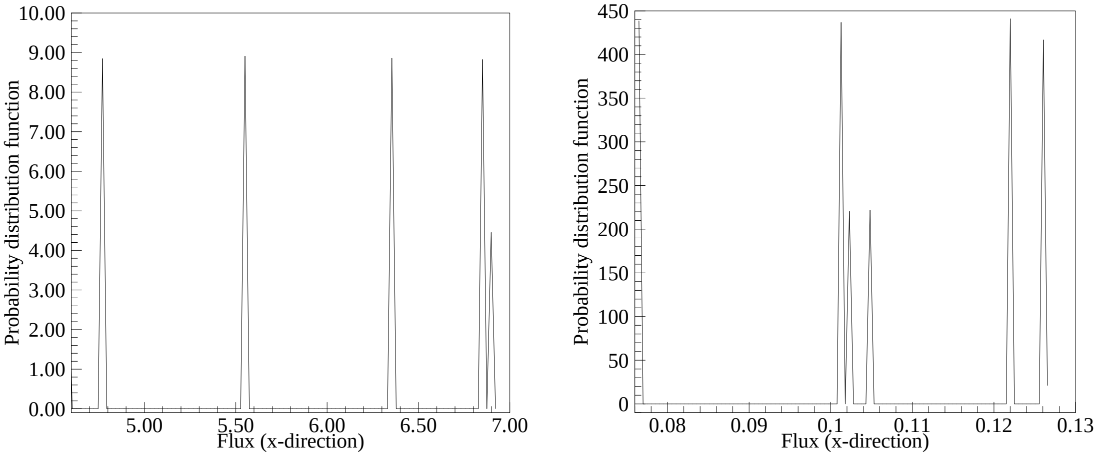

Figure 4.22: Probability distribution functions of the coarse-scale flux (*x*-direction) for two points in the domain.

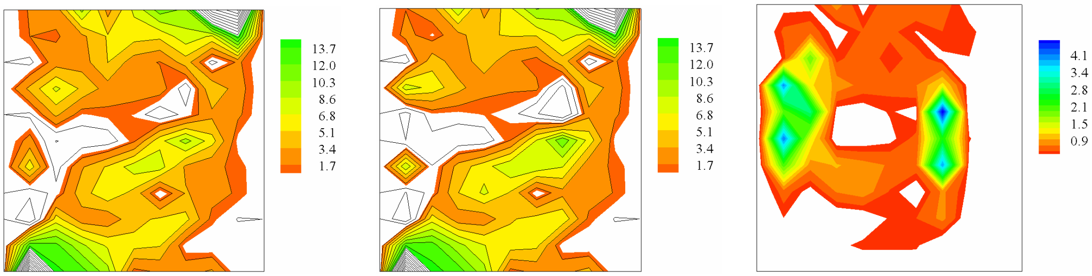

Figure 4.23: (left and center) Two realizations of the coarse-scale flux (*x*-direction) for a 1% perturbation in the *x*-location of the permeability barrier, (right) Difference between the two solutions.

In comparison with the uncertainty due to fine-scale permeability variation, even a small uncertainty in the location of large-scale structures results in significant variabilities in the flow patterns.

4.5.2 Effect of localized uncertainties

In this second example, we look at the effect of localized uncertainties in permeability and how they propagate into the complete domain. A schematic of the domain is shown in Fig. 4.24. The region consists of a 250×150 ft^2 domain where the fine-scale permeability is given in 1 ft^2 blocks. An injection well is located at the bottom left corner of the domain while a production well is placed at the top right corner of the domain. No flow boundary conditions are enforced on all the four boundaries. The fine-scale discretization of the domain corresponds to a 250 × 150 element triangulation.

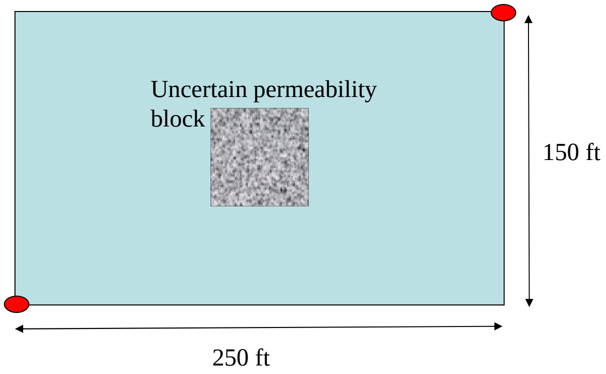

Figure 4.24: Schematic of the domain. The permeability is uncertain in part of the domain.

The fine-scale permeability in the domain is shown in Fig. 4.25. The deterministic permeability is taken from the 10-th SPE comparative project [125]. The permeability shows variation of 5 orders of magnitude. Furthermore, there is a localized region of uncertain fine-scale permeability in the central portion of the domain, corresponding to a 50 × 50 ft^2 domain. Aggressive coarse-scaling is performed at the complete domain which is characterized using a coarse 50 × 30 element discretization.

We are given a finite number of snapshots of plausible fine-scale permeability distributions in the uncertain permeability block. Based on the number of available snapshots, we consider two cases (a) for small number of snapshots, a linear model reduction strategy is utilized to construct a data-driven model of

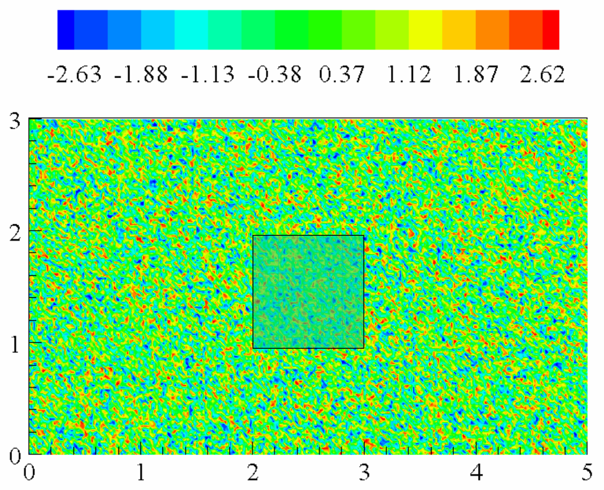

Figure 4.25: The fine-scale log permeability distribution in the domain. The axes are scaled (1 unit = 50 ft).

the fine-scale permeability in the domain, and (b) if a large number of snapshots are available, a non-linear model reduction strategy is utilized.

Small number of snapshots

In this case, a data-set containing 85 plausible fine-scale permeability distributions in the uncertain part of the domain is available. Based on the discussion in Chapter. 3, the covariance matrix C [140] is constructed using these 85 permeability distributions and the eigenvalue problem solved. Fig. 4.26 plots the eigen-spectrum of the covariance matrix. The first six eigenmodes accurately represent the variability in the given data-set. These eigen-modes are utilized to construct the corresponding low-dimensional representation of the stochastic-fine-scale permeability distribution in the central block of the domain. The dimensionality of the representation is 6.

12 nodes of our local Linux cluster (corresponding to 48 processors) was utilized. The total computational time was about 24 hours to solve this 6 + 2 (stochastic + spatial domain) dimensional problem. Fig. 4.27 (left) plots the con-

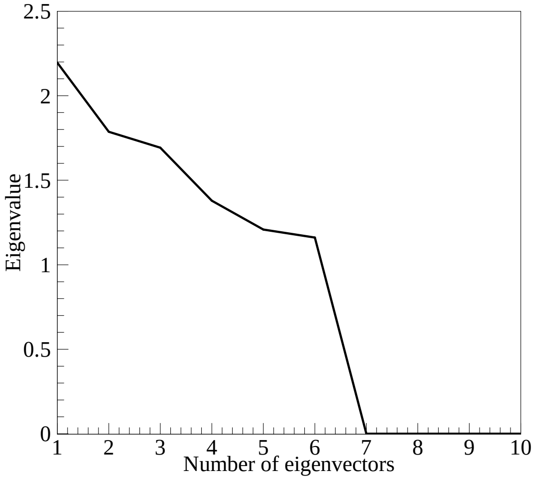

Figure 4.26: The eigen-spectrum of the data set. The first 6 eigen-modes represent most of the variation that the input data set exhibits.

vergence of the stochastic pressure (mean and standard deviation) with increasing number of collocation points, while Fig. 4.27 (right) plots the convergence of the stochastic *x*-direction flux with increasing number of collocation points.

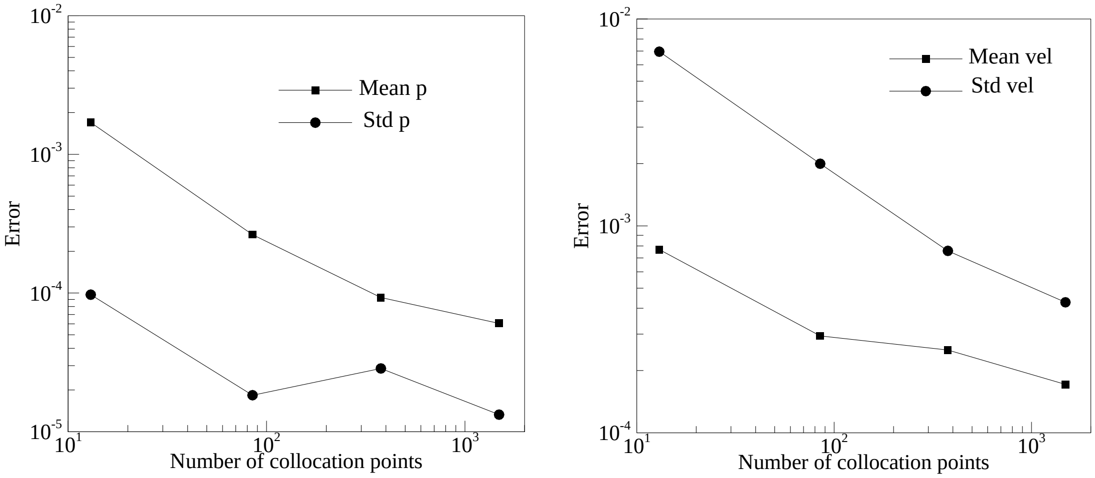

Figure 4.27: Convergence of the stochastic solution (mean and standard deviation) with increasing number of collocation points. (left) Stochastic coarse-scale pressure, (right) Stochastic coarse-scale *x*-direction flux.

Fig. 4.28 plots the mean contours of the stochastic coarse-scale pressure and flux in the *x*-direction. Note the highly dendrite-like structure of the *x*-direction flux. Due to the large variation in the permeability, the flow tries to find the path with the largest permeability resulting in this dendrite-like structure.

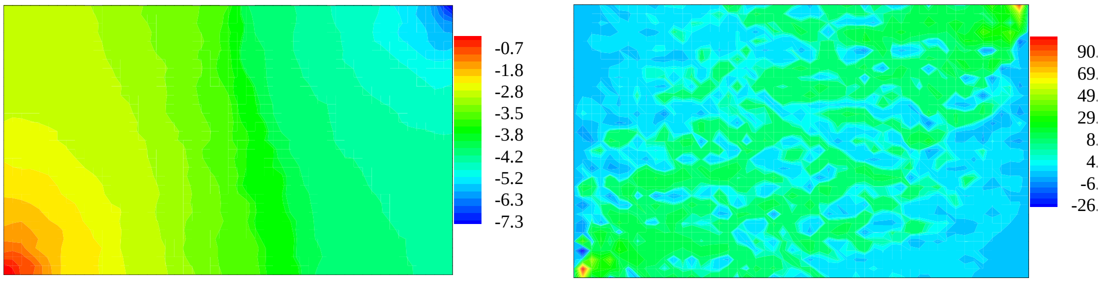

Figure 4.28: Mean contours of the stochastic coarse-scale solution. (left) Coarse-scale pressure, (right) Coarse-scale *x*-direction flux.

Fig. 4.29 plots the standard deviation contours of the coarse-scale stochastic pressure and *x*-direction flux. Upstream of the uncertain permeability block, the standard deviation of the coarse-scale pressure and velocity are both negligible. Most of the deviation in the pressure occurs in the uncertain domain with its effects felt downstream of the uncertain domain. The velocity flux has maximum deviation in the region of uncertainty and the deviation rapidly decays in the rest of the domain.

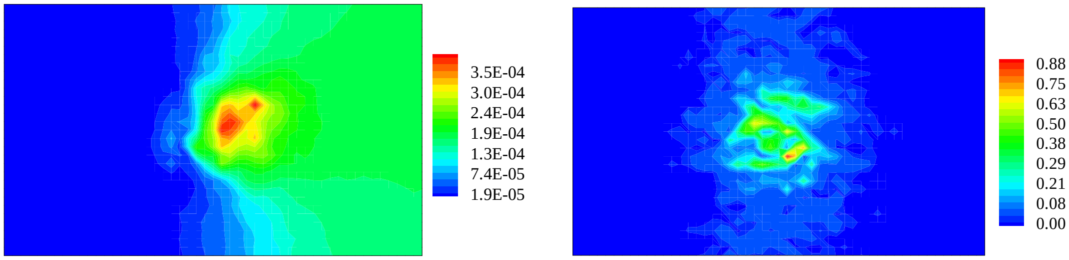

Figure 4.29: Standard deviation of the stochastic coarse-scale solution. (left) Coarse-scale pressure, (right) Coarse-scale *x*-direction flux.

From the stochastic solution, the probability distribution function of the coarse-scale pressure and *x*-direction flux is plotted at two spatial locations. The first point (50, 50) is upstream of the localized uncertain region, while the second point (125, 75) is in the region of uncertain fine-scale permeability. The PDFs are plotted in Figs. 4.30 and 4.31. For the point upstream, the probability distributions are peaked and have a very small range of variation. In comparison, the point in the region of uncertainty has a significantly larger range of variability.

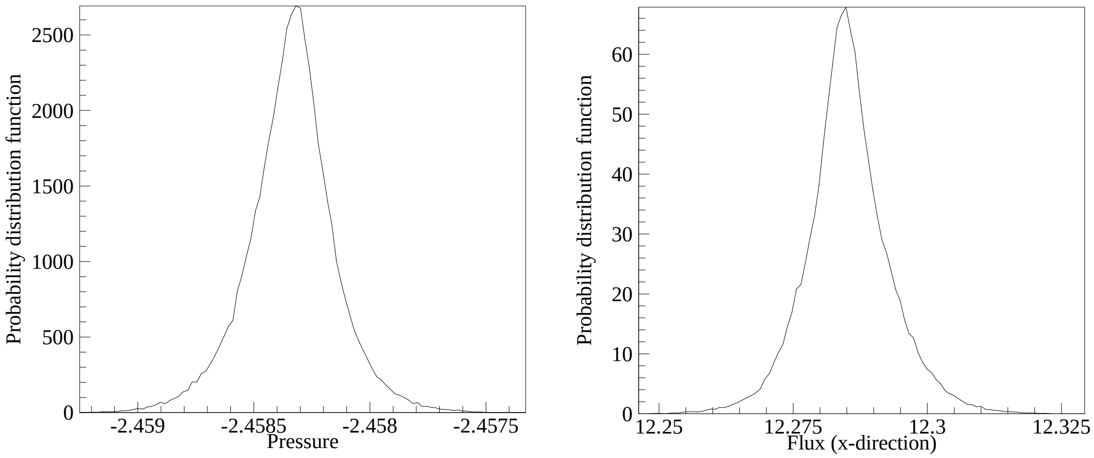

Figure 4.30: Probability distribution functions of the coarse-scale pressure (left) and flux (*x*-direction) (right) for a point upstream of the uncertainty.

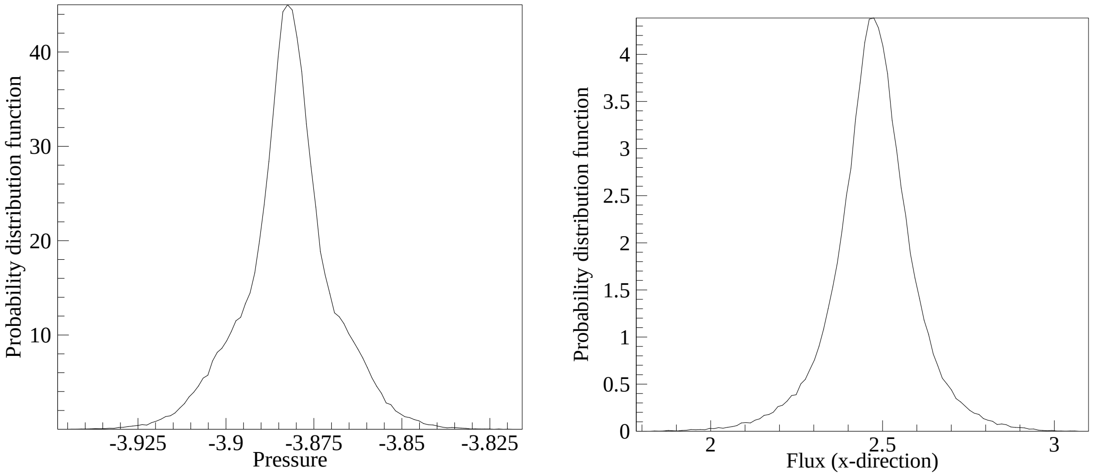

Figure 4.31: Probability distribution functions of the coarse-scale pressure (left) and flux (*x*-direction) (right) for a point in the uncertain domain.

Large number of snapshots

In this case, a data-set containing 1500 plausible fine-scale permeability distributions in the uncertain part of the domain is available. Based on the discussion in Chapter. 3, the neighborhood graph G is constructed using these 1500 permeability distributions. Following this, the geodesic distance matrix is computed. The BHH theorem [21] is used to compute the intrinsic dimensionality of the dataset. The dimensionality is related to the slope of the length functional of the minimal spanning graph (MST) of the neighborhood graph G of the dataset (see [21]). Fig. 4.32 plots the variation in the length functional of the MST. The optimal dimensionality was estimated to be $d = 5$. The corresponding low-dimensional representation of the stochastic-fine-scale permeability distribution in the central block of the domain is constructed.

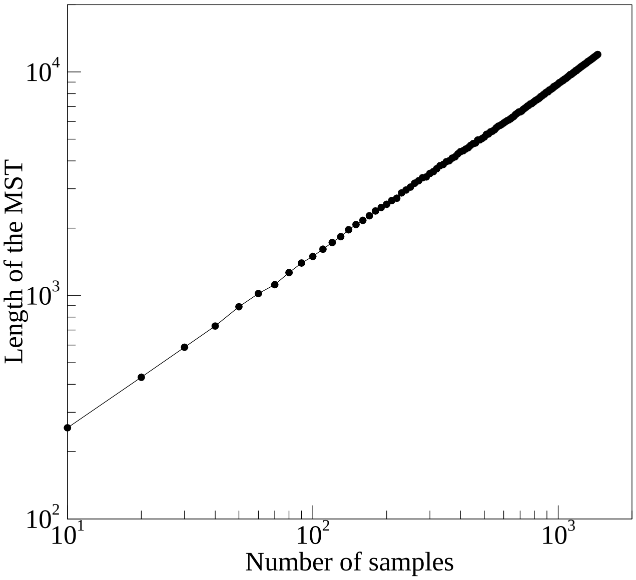

Figure 4.32: Plot of the length functional of the MST of the graph G for various sample sizes. The intrinsic dimension is related to the slope of the graph.

50 nodes of our local Linux cluster (corresponding to 200 processors) was utilized. The total computational time was about 12 hours to solve this 5 + 2

(stochastic + spatial domain) dimensional problem.

Fig. 4.33 plots the mean contours of the stochastic coarse-scale pressure and flux in the *x*-direction. The mean results are very similar to the results obtained by generating a data-driven model utilizing a much lower amount of initial information.

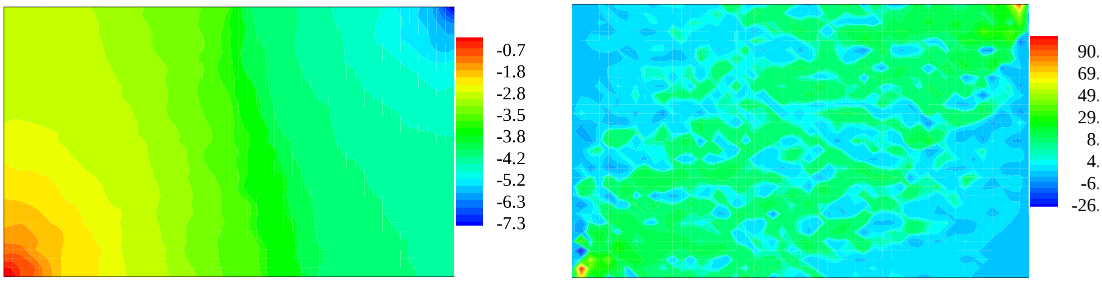

Figure 4.33: Mean contours of the stochastic coarse-scale solution. (left) Coarse-scale pressure, (right) Coarse-scale *x*-direction flux.

On the other hand, Fig. 4.34 plots the standard deviation contours of the coarse-scale stochastic pressure and *x*-direction flux. The utilization in more information (larger number of snapshots to build the input model) results in an overall reduction in the standard deviation in the domain, though the general trends are similar (compare Figs. 4.29 and 4.34).

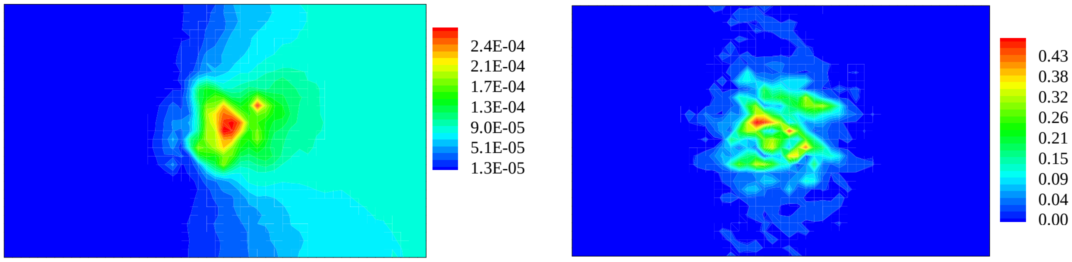

Figure 4.34: Standard deviation of the stochastic coarse-scale solution. (left) Coarse-scale pressure, (right) Coarse-scale *x*-direction flux.

From the stochastic solution, the probability distribution function of the

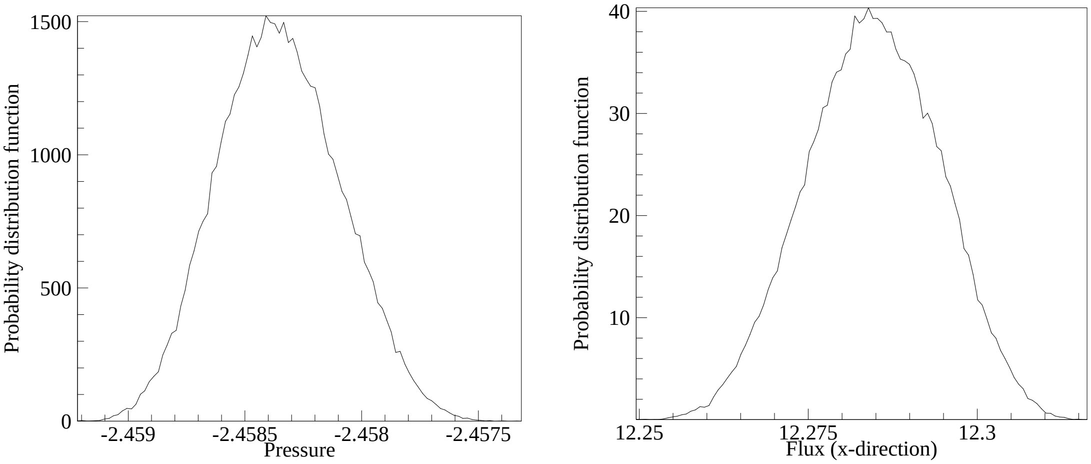

Figure 4.35: Probability distribution functions of the coarse-scale pressure (left) and flux (*x*-direction) (right) for a point upstream of the uncertainty.

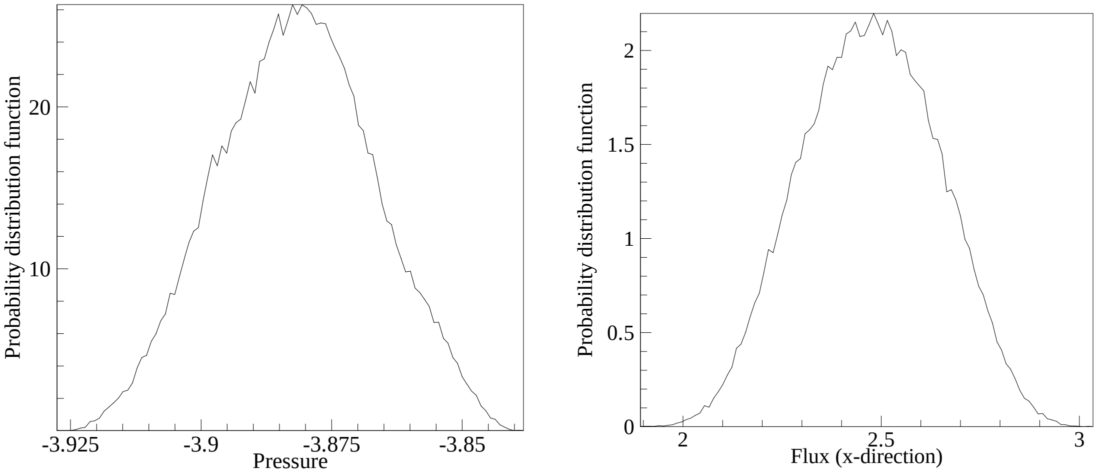

Figure 4.36: Probability distribution functions of the coarse-scale pressure (left) and flux (*x*-direction) (right) for a point in the uncertain domain.

coarse-scale pressure and *x*-direction flux is plotted at the same two spatial locations. The PDFs are plotted in Figs. 4.35 and 4.36. For the point upstream, the probability distributions are peaked and have a very small range of variation. In comparison, the point in the region of uncertainty has a significantly larger range of variability. Comparing Fig. 4.36 with Fig. 4.31 illustrates the effect of the incorporation of more data into the construction of the stochastic input model.

CHAPTER 5

CONCLUSIONS AND SUGGESTIONS FOR THE FUTURE RESEARCH

We have extended the state-of-art in deterministic multiscale modeling of flow through heterogeneous media to a stochastic multiscale framework. We accomplish this in three steps. In the first step, a variational stochastic mixed multiscale formulation is developed to incorporate the effects of stochastic fine-scale permeability. The input to this is a finite-dimensional representation of the stochastic permeability that is constructed from limited permeability information in the form of snapshots or statistics. We utilize various data-driven model reduction strategies to embed this limited information into viable stochastic input models of the permeability. The resulting multiscale SPDEs are solved utilizing an adaptive sparse grid collocation strategy. We showcase the complete formulation through realistic large scale applications of flow through heterogeneous random media. This is (to the best knowledge of the authors) the first instance of a stochastic variational multiscale treatment of flow through random heterogeneous media.

Although this thesis has addressed the fundamental issues with (a) solving stochastic partial differential equations in a computationally tractable form (b) generating reliable stochastic input models from limited experimental data, and (c) extend deterministic multiscaling ideas to stochastic multiscaling, there are several areas where developments are required. Suggestions for the continuation of this study are provided next.

5.1 Stochastic inverse problems

Experimental evidence suggests that the dynamics of many physical phenomena are significantly affected by the underlying uncertainties associated with variations in properties and fluctuations in operating conditions. Recent developments in stochastic analysis have opened the possibility of realistic modeling of such systems in the presence of multiple sources of uncertainties. These advances raise the possibility of solving the corresponding stochastic inverse problem: the problem of designing/estimating the evolution of a system in the presence of multiple sources of uncertainty given limited information. A scalable, parallel methodology for stochastic inverse/design problems can developed. The key features of the development could be the following (a) The representation of the underlying uncertainties and the resultant stochastic dependant variables is performed using a sparse grid collocation methodology. (b) A stochastic sensitivity method based on multiple solutions to deterministic sensitivity problems. (c) The stochastic inverse/design problem is transformed to a deterministic optimization problem in a larger-dimensional space that is subsequently solved using deterministic optimization algorithms. This ensures that the design framework relies entirely on deterministic direct and sensitivity analysis of the continuum systems, thereby significantly enhancing the range of applicability of the framework for the design in the presence of uncertainty of many other systems usually analyzed with legacy codes.

5.2 Incorporating correlation statistics and investigating regularization

In classical inverse problems [126, 127, 128, 129, 130, 131], the ill-posednes requires some form of regularization or smoothing assumptions for computing the solution. But in the context of stochastic inverse problems, we are searching for a solution *in a distribution sense* in a much larger space (tensor product space of spatio-temporal and stochastic variations). This expanded search space essentially guarantees a stochastic solution [137]. Nevertheless, regularization arguments play a very significant role in reducing the computational effort by imposing some smoothness criteria on the designed stochastic solution. Future work would be to investigate mathematical approaches to stochastic regularization as a purely computational strategy: (a) utilize spatial (temporal) regularization via parametrization of the spatial (temporal) representation of the unknown stochastic fields, and (b) utilize stochastic regularization via parametrization of the stochastic field.

Spatial (temporal) parametrization of the unknown stochastic fields: An ideal strategy would be to extend deterministic parametric representation of fields in a straightforward manner for the spatial representation of stochastic fields. There are many methodologies to parametrically represent the spatial variation of a stochastic field $q(\boldsymbol{x}, \boldsymbol{Y})$ (wavelets, polynomials, Bézier surfaces among others). Consider a Bézier representation of $\boldsymbol{q}(\boldsymbol{x}, \boldsymbol{Y})$- a stochastic field in two spatial dimensions. A Bézier curve of order (m_{x1}, m_{x2}) is defined by a set of

$(m_{x1}+1)\times(m_{x2}+1)$ control points $P_{i,j}$ as

$$q(x1, x2, \boldsymbol{Y}) = \sum_{i=0}^{m_{x1}} \sum_{j=0}^{m_{x2}} P_{i,j}(\boldsymbol{Y}) B_i^{m_{x1}}(x1) B_j^{m_{x2}}(x2), \quad \text{where,} \tag{5.1}$$

$$B_i^{m_x}(x) = \frac{m_x!}{i!(m_x - i)!} x^i (1 - x)^{m_x - i}. \tag{5.2}$$

The design variables are now the stochastic control values $P_{i,j}(\boldsymbol{Y})$. These design variables can be subsequently represented in terms of n_q collocated values as

$$P_{i,j}(\boldsymbol{Y}) = \sum_{r=1}^{n_q} P_{i,j}^r(\boldsymbol{Y}_r) L_r(\boldsymbol{Y}). \tag{5.3}$$

The sensitivity equations are now defined in terms of these n_q deterministic parameters. Since the choice of the parametrization controls the spatial smoothness of the solution, it is necessary to construct convergence estimates as the spatial parametrization is varied. Some preliminary work on convergence of this approximation is given in [138]. Similar arguments can be utilized to parameterize the temporal variation of the stochastic field.

Stochastic regularization of the unknown stochastic fields: An alternative strategy is to consider some stochastic regularization. This can be imposed by enforcing some correlation structure on the unknown stochastic field. The correlation kernel $C(\boldsymbol{x})$ determines the stochastic field and imposes some smoothness on its spatial variability. This will convert the problem of designing the stochastic field $\boldsymbol{q}$ to the problem of designing its correlation structure $C(\boldsymbol{x})$. The unknown correlation function is represented in terms of its spectral expansion

$$C(r) = \sum_{i=1}^{K} a_i \sin(ix/L), \tag{5.4}$$

where L is the characteristic length of the system and $\{a_i\}$ is the set of K Fourier modes of the correlation function (and we have assumed that the field is isotropic, without loss of generality). By representing the correlation this way, the stochastic optimization problem is converted to computing the modal coefficients $\{a_i\}$. The design parameters are now the set of K scalars $\{a_i\}$. Given any correlation kernel, the Karhunen-Loève expansion can be utilized to explicitly represent the stochastic field as

$$q(\boldsymbol{x}, \omega) = E(q(\boldsymbol{x}, \omega)) + \sum_{i=0}^{N} \sqrt{\lambda_i} f_i(\boldsymbol{x}) Y_i(\omega), \tag{5.5}$$

where $(\lambda_i, f_i(\boldsymbol{x}))$ are the eigen-pairs of the correlation function. The stochastic sensitivity equations are formulated in terms of these K deterministic scalars. The choice of the number of modes K used in the representation of the unknown correlation provides a measure of the regularization. Including higher frequencies (larger K) allows $C(r)$ to be very steep representing a highly uncorrelated field. One would expect to utilize an iterative solution strategy to sequentially increase the number of Fourier modes in the expansion to guarantee the accuracy of the stochastic solution. Defining and constructing the gradient of the cost functional is important along with developing a strategy for estimating the number of modes required based on the statistics of the measurements.

Spatial correlation statistics provides some notion of how easy or difficult it is to physically realize the designed process. A very large or small correlation signifies expensive manufacturing, fabrication or operating conditions. This introduces the possibility of computing the designed fields with some constraints to obtain physically accessible fields. The above proposed strategies naturally take into account these issues.

5.3 Stochastic low-dimensional modeling

In the stochastic inverse/design problem, we need to solve the direct problem and the sensitivity problem for all of the collocation points at each iteration. For large stochastic dimensionality, each iteration in the optimization procedure will take substantial amount of computational time. The solution procedure can be accelerated significantly if a reduced order model of the system can be constructed. A development would be to utilize model reduction strategies to extract the coherent structures [132] of the system evolution. *This reduced representation can either be created off-line or adaptively modified on-the-fly* [133, 134, 135].

One area of research would be to extend the classical POD method to stochastic evolution equations based on recent work in [139] coupled with recent work [133, 134, 135] on solving constrained optimization problems using POD basis. We propose to develop a compact expansion of the stochastic dependent variable into stochastic spatial modes. Consider a random field $\boldsymbol{u}(\boldsymbol{x}, t; \boldsymbol{Y})$ in a space-time domain and we look for biorthogonal representations as

$$\boldsymbol{u}(\boldsymbol{x}, t; \boldsymbol{Y}) \quad = \quad \sum_{i=1}^{K} b_i^{(h)}(t) \boldsymbol{a}_i^{(h)}(\boldsymbol{x}; \boldsymbol{Y}). \tag{5.6}$$

The spatial-stochastic modes $\boldsymbol{a}_i^{(h)}(\boldsymbol{x}; \boldsymbol{Y})$ are constructed from snapshots of the stochastic field (either from off-line calculations, available numerical data or experimental data) by solving an eigenvalue problem. This eigen-value problem arises from the Euler-Lagrange equations resulting from minimizing the residual of the projection of the stochastic field onto the basis functions [132, 139]. The residual is calculated based on some norm $\{,.,\}_h$. Recent work [139] has suggested that this stochastic counterpart of the POD framework will produce low-order ODEs (in terms of the temporal coefficients $b_i^{(h)}(t)$) that are independent of the stochastic dimensionality of the system. It is important that care be taken in choosing the appropriate norm over which to construct the spatial stochastic basis. As a preliminary step, one could utilize inner products based on the mean, variance and standard deviation [139]:

$$\{b,c\}_0 := \int_{\mathcal{D}} \langle b\rangle \cdot \langle c\rangle d\boldsymbol{x}, \quad \{b,c\}_1 := \int_{\mathcal{D}} \langle b\cdot c\rangle d\boldsymbol{x} \quad \{b,c\}_2 := \int_{\mathcal{D}} \left(\langle b\cdot c\rangle - \langle b\rangle \cdot \langle c\rangle\right) d\boldsymbol{x} \tag{5.7}$$

The construction of these spatial-stochastic modes $\boldsymbol{a}_i$ should be done using sparse grid collocation. That is, the stochastic modes are represented as

$$\boldsymbol{a}_k^{(h)}(\boldsymbol{x};\mathbf{Y}) = \sum_{i=1}^{M} \hat{\boldsymbol{a}}_{ki}^{(h)}(\boldsymbol{x},\mathbf{Y}_i)L_i(\mathbf{Y}). \tag{5.8}$$

An arbitrary stochastic field is represented in terms of these stochastic modes as

$$\boldsymbol{u}(\boldsymbol{x},t;\boldsymbol{Y}) = \sum_{i=1}^{K} b_i^{(h)}(t) \sum_{j=1}^{M} \boldsymbol{a}_{ij}^{(h)}(\boldsymbol{x};\mathbf{Y}_j)L_j(\mathbf{Y}). \tag{5.9}$$

The unknowns are the deterministic coefficients $\{b_i\}$. Inserting this representation, Eq. (5.9) into Eqs. (2.3) and using the orthogonality properties of the modes results in a set of ODEs for the modal coefficients, $\{b_i\}$.

$$(\mathcal{B}(\sum_{i=1}^{K} b_i^{(h)}(t)\boldsymbol{a}_i^{(h)} : \{\boldsymbol{q},\alpha\}), b_j^{(h)}) = 0, \quad j = 1,...,K, \tag{5.10}$$

which can be written in compact form as

$$\frac{\partial b_j^h}{\partial t} = \mathcal{F}_j(b_j^h), \quad j = 1,...,K. \tag{5.11}$$

The cost functional, its gradient and the stochastic optimization problem can now be posed in terms of this set of ODEs instead of the set of SPDEs.

$$\begin{aligned} \text{Minimize} \quad & \mathcal{CF}(\{b_i\},\{q_i\}), \\ \text{subject to} \quad \frac{\partial b_i^h}{\partial t} &= \mathcal{F}_i(b_i^h), \quad j = 1,...,K, \\ b_i(0) &= b_i^0. \end{aligned} \tag{5.12}$$

There has been recent progress on developing reduced order models to control systems defined by PDEs [133, 134, 135]. In such approaches, an adaptive procedure is used that successively updates the ensemble of data snapshots and the reduced order model during the optimization procedure. It would be helpful to utilize this strategy via straightforward extension to computing stochastic modes (Eq. 5.9) for the control/optimization of SPDEs.

BIBLIOGRAPHY

[1] Major aircraft disasters, information available at (`http://dnausers.d-n-a.net/dnetGOJG/Disasters.htm`).

[2] AIM, Accelerated insertion of materials program, DSO Office, DARPA, information available at `http://www.darpa.mil/dso/thrust/matdev/aim.htm`.

[3] Prognosis, Prognosis program, DSO Office, DARPA, information available at `http://www.arpa.mil/dso/thrust/matdev/prognosis.htm`.

[4] National security assessment of the U.S. forging industry, Bureau of industry and security, U.S. dept. of commerce `https://www.bis.doc.gov/defenseindustrialbaseprograms/osies/`.

[5] MAI, Metals affordability initiative, AFRL/ML, information available at `http://www.wrs.afrl.af.mil/contract/`.

[6] The USAF/Navy forging supplier initiative, information available at: `http://www.onr.navy.mil/scitech/industrial/mantech/docs/successes/metals/`.

[7] R. G. Ghanem, P. D. Spanos, Stochastic Finite Elements: A Spectral Approach, Dover publications, 1991.

[8] R. Ghanem, Probabilistic characterization of transport in heterogeneous porous media, Comput. Methods Appl. Mech. Engrg. 158 (1998) 199-220.

[9] R. Ghanem, A. Sarkar, Mid-frequency structural dynamics with parameter uncertainty, Comput. Methods Appl. Mech. Engrg. 191 (2002) 5499-5513.

[10] R. Ghanem, Higher order sensitivity of heat conduction problems to random data using the spectral stochastic finite element method, ASME J. Heat Transfer 121 (1999) 290-299.

[11] D. Xiu, G. E. Karniadakis, Modeling uncertainty in steady state diffusion problems via generalized polynomial chaos, Comput. Methods Appl. Mech. Engrg. 191 (2002) 4927-4948.

[12] D. Xiu, G. E. Karniadakis, Modeling uncertainty in flow simulations via generalized polynomial chaos, J. Comp. Physics 187 (2003) 137–167.

[13] D. Xiu, G. E. Karniadakis, A new stochastic approach to transient heat conduction modeling with uncertainty, Int. J. Heat Mass Transfer 46 (2003) 46814693.

[14] B. Ganapathysubramanian, N. Zabaras, Sparse grid collocation schemes for stochastic natural convection problems, Journal of Computational Physics 225 (1) (2007) 652–685.

[15] I. Babuska, F. Nobile, R. Tempone, A stochastic collocation method for elliptic partial differential equations with random input data, ICES Report 05-47, 2005.

[16] D. Xiu, J. S. Hesthaven, High order collocation methods for the differential equation with random inputs, SIAM J. Sci. Comput. 27 (2005) 1118–1139.

[17] C. W. Gardiner, Handbook of stochastic methods for physics, chemistry and the natural sciences, Springer-Verlag,1990

[18] M. Loѐve, Probability Theory, Springer-Verlag: 4th Edition, Berlin, 1977.

[19] C. Desceliers, R. Ghanem, C. Soize, Maximum likelihood estimation of stochastic chaos representations from experimental data, Int. J. Numer. Meth. Engng. 66 (2006) 978–1001.

[20] B. Ganapathysubramanian, N. Zabaras, Modelling diffusion in random heterogeneous media: Data-driven models, stochastic collocation and the variational multi-scale method, Journal of Computational Physics, 226 (2007) 326-353

[21] B. Ganapathysubramanian and N. Zabaras, A non-linear dimension reduction methodology for generating data-driven stochastic input models, J. Comput. Phys., in press (http://dx.doi.org/10.1016/j.jcp.2008.03.023).

[22] S. T. Roweis, L. K. Saul, Nonlinear Dimensionality Reduction by Locally Linear Embedding, Science 290 (2000) 2323–2326.

[23] J. Tenenbaum, V. DeSilva, J. Langford, A global geometric framework for nonlinear dimension reduction, Science, 2000.

[24] V. deSilva, J. B. Tenenbaum, Global versus local methods in nonlinear dimensionality reduction, Advances in Neural Information Processing Systems 15 (2003) 721–728.

[25] M. Bernstein, V. deSilva, J. C. Langford, J. B. Tenenbaum, Graph approximations to geodesics on embedded manifolds, Dec 2000, Preprint may be downloaded at the URL: `http://isomap.stanford.edu/BdSLT.pdf`.

[26] J. R. Munkres, Topology, Second edition, Prentice-Hall, 2000.

[27] J. A. Costa, A. O. Hero, Entropic Graphs for Manifold Learning, Proc. of IEEE Asilomar Conf. on Signals, Systems, and Computers, Pacific Groove, CA, November, 2003.

[28] J. A. Costa, A. O. Hero, Geodesic Entropic Graphs for Dimension and Entropy Estimation in Manifold Learning, IEEE Trans. on Signal Processing 52 (2004) 2210–2221.

[29] T. H. Cormen, C. E. Leiserson, R. L. Rivest, C. Stein, Introduction to Algorithms, 2001, The MIT Press.

[30] J. A. Costa, A. O. Hero,Manifold Learning with Geodesic Minimal Spanning Trees, 2003, arXiv:cs/0307038v1.

[31] D. Frenkel, B. Smit, Understanding Molecular Simulations: From Algorithms To Applications, Academic Press, 2002.

[32] L. Guadagnini, A. Guadagnini, D. M. Tartakovsky, Probabilistic reconstruction of geologic facies, J. Hydrol. 294 (2004) 57–67.

[33] C. L. Winter, D. M. Tartakovsky, Mean flow in composite porous media. Geophys. Res. Lett., 27 (2000) 1759-1762, 2000

[34] C. L. Winter, D. M. Tartakovsky, Groundwater flow in heterogeneous composite aquifers. Water Resour. Res., 38 (2002) 23.1

[35] C. L. Winter, D. M. Tartakovsky, A. Guadagnini, Numerical solutions of moment equations for flow in heterogeneous composite aquifers. Water Resour. Res., 38 (2002) 13.1

[36] C. L. Winter, D. M. Tartakovsky, A. Guadagnini, Moment equations for flow in highly heterogeneous porous media. Surv. Geophys., 24 (2003) 81-106.

[37] M. Jardak, C-H. Su, G. E. Karniadakis, Spectral Polynomial Chaos Solutions of the Stochastic Advection Equation, J. Sci. Comput. 17 (2002) 319–338.

[38] D. Lucor, C-H. Su, G. E. Karniadakis, Karhunen-Loève representation of periodic second-order autoregressive processes, International Conference on Computational Science (2004) 827-834.

[39] X. Wan, G. E. Karniadakis, An adaptive multi-element generalized polynomial chaos method for stochastic differential equations, J. Comp. Physics 209 (2005) 617–642.

[40] X. Wan, D. Xiu, G. E. Karniadakis, Stochastic Solutions for the Two-Dimensional Advection-Diffusion Equation, SIAM J. Sci. Computing 26 (2005) 578–590.

[41] D. Xiu, G. E. Karniadakis, The Wiener-Askey Polynomial Chaos for Stochastic Differential Equations, SIAM J. Sci. Computing 24 (2002) 619–644.

[42] B. Velamur Asokan, N. Zabaras, Variational multiscale stabilized FEM formulations for transport equations: stochastic advection-diffusion and incompressible stochastic Navier-Stokes equations, J Comp. Physics 202 (2005) 94–133.

[43] M. K. Deb, I. K. Babuska, J. T. Oden, Solution of stochastic partial differential equations using the Galerkin finite element techniques, Comput. Methods Appl. Mech. Engrg. 190 (2001) 6359–6372.

[44] I. Babuska, R. Tempone, G. E. Zouraris, Solving elliptic boundary value problems with uncertain coefficients by the finite element method: the stochastic formulation, Comput. Methods Appl. Mech. Engrg. 194 (2005) 1251–1294.

[45] I. Babuska, R. Tempone, G. E. Zouraris, Galerkin finite elements approximation of stochastic finite elements, SIAM J. Numer. Anal. 42 (2004) 800–825.

[46] D. Xiu,, D. Lucor, C.-H. Su, G. E. Karniadakis, Performance Evaluation of Generalized Polynomial Chaos, International Conference on Computational Science, Lecture Notes in Computer Science, Vol. 2660, pp. 346-354, Springer, 2003.

[47] R. Tempone, Numerical Complexity Analysis of Weak Approximation of Stochastic Differential Equations, PhD Thesis, 2002.

[48] B. Velamur Asokan, N. Zabaras, Using stochastic analysis to capture unstable equilibrium in natural convection, J. Comp. Physics 208 (2005) 134–153.

[49] E. Novak, K. Ritter, The curse of dimension and a universal method for numerical integration, Multivariate approximation and splines, G. Nurnberger, J. W. Schmidt, G. Walz (eds.), 1997, 177–188.

[50] T. Gerstner, M. Griebel, Numerical integration using sparse grids, Numerical Algorithms, 18 (1998) 209–232.

[51] T. Grestner, M. Griebel, Dimension adaptive tensor product quadrature, Computing 71 (2003) 65–87.

[52] E. Novak, K. Ritter, R. Schmitt, A. Steinbauer, On an interpolatory method for high dimensional integration, J. Comp. Appl. Mathematics, 112 (1999) 215–228.

[53] V. Barthelmann, E. Novak, K. Ritter, High dimensional polynomial interpolation on sparse grids, Adv. Compu. Math. 12 (2000) 273–288.

[54] A. Klimke. Uncertainty Modeling using Fuzzy Arithmetic and Sparse Grids, PhD Thesis, Universitt Stuttgart, Shaker Verlag, Aachen, 2006.

[55] C. Canuto, M. Y. Hussaini, A. Quarteroni, T. A. Zang, Spectral Methods: Fundamentals in Single Domains Series, Springer 2006

[56] D. Xiu, Efficient Collocational Approach for Parametric Uncertainty Analysis, Communications In Computational Physics 2 (2007) 293–309.

[57] A. Klimke, B. Wohlmuth, Algorithm 847: *spinterp*: Piecewise Multilinear Hierarchical Sparse Grid Interpolation in *MATLAB*, ACM Transactions on Mathematical Software 31 (2005).

[58] A. Klimke, Sparse Grid Interpolation Toolbox – User's Guide, IANS report 2006/001, University of Stuttgart, 2006.

[59] `http://mpdc.mae.cornell.edu/Software`.

[60] Y. Shen, P. Tong, K. -Q. Xia, Turbulent convection over rough surfaces, Phys. Rev. Let. 76 (1996) 908–911.

[61] D. M. Tartakovsky, D. Xiu, Stochastic analysis of transport in tubes with rough walls, J. Comput. Physics 217 (2006) 248-259.

[62] E. Bodenschatz, W. Pesch, G. Ahlers, Recent developments in Rayleigh-Bénard convection, Annu. Rev. Fluid Mech. 32 (2000) 709–778.

[63] P. Nithiarasu, K. N. Seetharamu, T. Sundararajan, Natural convective heat transfer in a fluid saturated variable porosity medium, Int. J. Heat Mass Transfer 40 (1997) 3955–3967.

[64] C. Manwart, R. Hilfer, Reconstruction of random media using Monte Carlo methods, Physical Review E 59 (1999) 5597–5600.

[65] D. Samanta, N. Zabaras, Modeling melt convection in solidification processes with stabilized finite element techniques, International Journal for Numerical Methods in Engineering, 64 (2005) 1769–1799.

[66] S. Umekawa, R. Kotfila, O. D. Sherby, Elastic properties of a tungsten-silver composite above and below the melting point of silver, J. Mech. Phys. Solids 13 (1965) 229-230.

[67] J. Aldazabal, A. Martin-Meizoso, J. M. Martinez-Esnaola, Simulation of liquid phase sintering using the Monte-Carlo method, Mater. Sci. Eng. A 365 (2004) 151-155.

[68] A. P. Roberts, E. J. Garboczi, Elastic properties of a tungsten-silver composite by reconstruction and computation, J. Mech. Phys. Solids 47 (1999) 2029–2055.

[69] L. Arleth, S. Marčelja. T. Zemb, Gaussian random fields with two level-cuts– Model for asymmetric microemulsions with nonzero spontaneous curvature, The Journal of Chemical Physics 115 (8) (2001) 3923–3936.

[70] `http://www.mathworks.com/products/matlab/`.

[71] F. F. Abraham, J. Q. Broughton, N. Bernstein, E. Kaxiras, Spanning the Length Scales in Dynamic Simulation, Computers In Physics 12 (1998) 538–546.

[72] H. Li, K. E. Torrance, An experimental study of the correlation between surface roughness and light scattering for rough metallic surfaces, Advanced Characterization Techniques for Optics, Semiconductors, and Nanotechnologies II, edited by Angela Duparr, Bhanwar Singh, Zu-Han Gu, Proceedings of SPIE Vol. 5878 (SPIE, Bellingham, WA, 2005).

[73] GSLIB: Geostatistical Software Library, available at `http://www.pe.utexas.edu/Geosci/Software/GSLIB/gslib.html`.

[74] N. Zabaras, S. Sankaran, An information-theoretic approach to stochastic materials modeling, IEEE Computing in Science and Engineering (CISE), special issue of 'Stochastic Modeling of Complex Systems', March/April issue (2007) 50–59.

[75] V. Sundararaghavan, N. Zabaras, Classification of three-dimensional microstructures using support vector machines, Computational Materials Science 32 (2005) 223–239.

[76] S. Sankaran, N. Zabaras, A maximum entropy approach for property prediction of random microstructures, Acta Materialia 54 (2006) 2265–2276.

[77] N. Zabaras, S. Sankaran, Computing property variability of polycrystals induced by grain size and orientation uncertainties, Acta Materialia 55 (2007) 2279-2290.

[78] A Global Geometric Framework for Nonlinear Dimensionality Reduction, freely downloadable software available at `http://isomap.stanford.edu/`.

[79] J. T. Kent, J. M. Bibby, K. V. Mardia, Multivariate Analysis (Probability and Mathematical Statistics), Elsevier (2006).

[80] S. Torquato, Statistical description of microstructures, Ann. Rev. Mater. Sci. 32 (2002) 77-111.

[81] S. Torquato, Random Heterogeneous Materials: Microstructure and Macroscopic Properties, Springer, 2002.

[82] C. Goffman, G. Pedrick, First course in functional analysis, Prentice-Hall, 2002.

[83] J. Breadwood, J.H. Halton, J.M. Hamersley, The shortest path through many points, Proc. Cambridge Philos. Soc. 55 (1959) 299–327.

[84] W. Hardle, L. Simar, Applied Multivariate Statistical Analysis, 2004, available online at `http://www.quantlet.com/mdstat/scripts/mva/htmlbook/`.

[85] C-G. Li, J. Guo, G. Chen, X-F. Nie, Z. Yamg, A version of Isomap with explicit mapping, Proceedings of the Fifth International conference on machine learning and cybernetics, Dalian, Aug 2006.

[86] C. L. Y. Yeong, S. Torquato, Reconstructing random media. II. Three-dimensional media from two-dimensional cuts, Phys. Rev. E 58 (1998) 224-233.

[87] A. P. Roberts, M. A. Knackstedt, Structure property correlations in model composite materials, Phys. Rev. E 54 (1996) 2313–2328.

[88] P. S. Koutsourelakis, G. Deodatis, Simulation of multi-dimensional binary random fields with application to modeling of two phase random media, J. Engg. Mech. 132 (2006) 619–631.

[89] Intrinsic Dimension and Entropy Estimation in Manifold Learning, Matlab codes available at `http://www.eecs.umich.edu/hero/IntrinsicDim/`.

[90] The Qhull source code available at `http://www.qhull.org/`.

[91] P. J. Bickel, K. A. Doksum, Mathematical statistics- Basic ideas and selected topics, Prentice Hall, 2001.

[92] H. Hotelling, Tubes and Spheres in n-Spaces and a Class of Statistical Problems, American Journal of Mathematics 61 (1939) 440–460.

[93] T. F. Cox, M. A. A. Cox, Multidimensional scaling, Chapman and Hall, 1994.

[94] T. Arbogast, S. L. Bryant, A two-scale numerical subgrid technique for waterflood simulations, SPE J. (2002) 446-457.

[95] T. Arbogast, S. E. Minkoff, P. T. Keenan, An operator-based approach to upscaling the pressure equation, Computational Methods in Water Resources XII, Computational Methods in Contamination and Remediation of Water Resources Vol. 1, Computational Mechanics Publications, Southampton, UK (1998).

[96] T. Arbogast, Implementation of a locally conservative numerical subgrid upscaling scheme for two-phase darcy flow, Comput. Geosci. 6 (2002) 453-480.

[97] T. Arbogast, Numerical subgrid upscaling of two-phase flow in porous media, Lecture Notes in Physics vol. 552, Springer, Berlin (2000).

[98] T. J. R. Hughes, Multiscale phenomena: Greens functions, the dirichlet-to-neumann formulation, subgrid scale models, bubbles and the origin of stabilized methods, Comp. Meth. Appl. Mech. Eng. 127 (1995) 387-401.

[99] T. J. R. Hughes, G. R. Feijo, L. Mazzei, J. B. Quincy, The variational multiscale method a paradigm for computational mechanics, Comp. Meth. Appl. Mech. Engrg. 166 (1998) 3-24.

[100] R. Juanes, T. W. Patzek, A variational multiscale finite element method for multiphase flow in porous media, Finite Elements in Analysis and Design, 41 (2005) 763–777.

[101] W. E, B. Engquist, The heterogeneous multiscale methods, Comm. Math. Sci. 1 (2003) (1) 87-133.

[102] W. E., P. B. Ming, P. W. Zhang, Analysis of the heterogeneous multiscale method for elliptic homogenization problems, preprint (2003).

[103] T. Y. Hou, X. H. Wu, A multiscale finite element method for elliptic problems in composite materials and porous media, J. Comput. Phys. 134 (1997) 169-189.

[104] T. Y. Hou, X. H. Wu, Z. Q. Cai, Convergence of a multiscale finite element method for elliptic problems with rapidly oscillating coefficients, Math. Comput. 68 (1999) 913-943.

[105] P. Park, T. Y. Hou, Multiscale numerical methods for singularly-perturbed convection diffusion equations, Int. J. Comput. Meth. 1 (2004) 17-65.

[106] Y. Efendiev, V. Ginting, T. Y. Hou, R. Ewing, Accurate multiscale finite element methods for two-phase flow simulations, J. Comput. Phys., submitted.

[107] J.E. Aarnes, V. Kippe, K.A. Lie, Mixed multiscale finite elements and streamline methods for reservior simulation of large geomodels, Adv. water. Resources. 28 (2005) 257–271.

[108] I. Babuska, U. Banerjee, J. Osborn, Generalized finite element methods: main ideas, results and perspective, Int. J. Comput. Meth. 1 (2004) 67-103.

[109] G. Sangalli, Capturing small scales in elliptic problems using a residual-free bubbles finite element method, SIAM MMS 1 (2003) 485-503.

[110] D. Xiu, Efficient collocational approach for parametric uncertainty analysis, Comm. Computational Physics 2 (2) (2007) 293–309.

[111] X. Ma, N. Zabaras, An adaptive hierarchical sparse grid collocation algorithm for the solution of stochastic differential equations, J. Comput. Phys., submitted.

[112] X. Frank Xu, A multiscale stochastic finite element method on elliptic problems involving uncertainties, Comput. Methods Appl. Mech. Engrg. 196 (2007) 2723-2736

[113] R. Juanes, F.-X. Dub, A locally-conservative variational multiscale method for the simulation of flow in porous media with multiscale source terms, Computational Geosciences, 2008, in press.

[114] T. Arbogast, K. J. Boyd, Subgrid Upscaling and Mixed Multiscale Finite Elements, SIAM J. Num. Analysis 44 (2006) 1150 - 1171

[115] Ch. Schwab, R. A. Todur, Sparse finite elements for stochastic elliptic problems–higher moments, Computing 71 (1) (2003) 43–63.

[116] Ch. Schwab, R. A. Todur, Sparse finite elements for elliptic problems with stochastic loading, Numerische Mathematik 95 (2001) 707–734.

[117] T. Petersdorff, Ch. Schwab, Sparse finite element methods for operator equations with stochastic data, Applications of Mathematics 51 (2006) 145–180.

[118] F. Brezzi, M. Fortin, Mixed and hybrid finite element methods, Springer-Verlag 1991

[119] P.A.Raviart, J.M. Thomas, A mixed finite element method for second order elliptic problems, in: Mathematical aspects of the finite element method, Lecture Notes in Mathematics 606, Springer-Verlag, Berlin 1977

[120] V. Kippe, J.E.Aarnes, K.A.Lie, A comparison of multiscale methods for elliptic problems in porous media flow, Computational Geosciences, (2007) in press.

[121] P. Holmes, J. L. Lumley, G. Berkooz, Turbulence, Coherent Structures, Dynamical Systems and Symmetry, Cambridge University Press, 1998.

[122] F. Nobile, R. Tempone, C. Webster, An anisotropic sparse grid collocation method for elliptic partial differential equations with random input data, MOX, Dipartimento di Matematica, Politecnico di Milano, Italy, 2007.

[123] S. Smolyak, Quadrature and interpolation formulas for tensor product of certain classes of functions, Soviet Math. Dokl. 4 (1963) 240–243.

[124] J.W. Jennings, S.l. Bryant, Outcrop permeability statistics and implication for fluid flow and reactive transport modeling, Bureau of Economic Geology, U. Texas Austin, 2000 report.

[125] M.A. Christie, M.J. Blunt, Tenth SPE comparative solution project: A comparison of upscaling techniques, SPE Reserv. Eval. Eng. 4 (2001) 308–317.

[126] A. N. Tikhonov, V. Y. Arsenin, Solutions of Ill-Posed Problems. John Wiley, New York, 1977.

[127] O. Alifanov, Inverse Heat Transfer Problems, Springer, 1995.

[128] H. W. Engl, M. Hanke,A. Neubauer, Regularization of Inverse Problems, Kluwer Academic Publishers, 1996.

[129] A. Kirsch, An Introduction to the Mathematical Theory of Inverse Problems, Springer, 1996.

[130] V. Isakov, Inverse Problems for Partial Differential Equations (Applied Mathematical Sciences), Springer, 2005.

[131] V. A. Morozov, Methods for Solving Incorrectly Posed Problems. Springer-Verlag, New York, 1984.

[132] P. Holmes, J. L. Lumley, G. Berkooz, Turbulence, Coherent Structures, Dynamical Systems and Symmetry, Cambridge Univ press, 1996.

[133] S.S. Ravindran, Adaptive Reduced-Order Controllers for a Thermal Flow System, SIAM Journal on Scientific Computing 23 (2002) 1925–1943.

[134] S.S. Ravindran, Control of flow separation over a forward-facing step by Model reduction, Computer Methods in Applied Mechanics and Engineering 191 (2002) 4599–4617.

[135] K. Ito, S.S. Ravindran, Reduced Basis Method for Optimal Control of Unsteady Viscous Flows, International Journal of Computational Fluid Dynamics 15 (2001) 97–113.

[136] D. Venturi, X. Wan, G. E. Karniadakis, Stochastic low-dimensional modeling of random laminar wake past a circular cylinder, preprint.

[137] J Kaipio, E Somersalo, Statistical and computational inverse problems, Springer, New York, 2005.

[138] N. Zabaras, B. Ganapathysubramanian, A scalable framework for the solution of stochastic inverse problems using a sparse grid collocation approach, J. Computational Physics 227 (2008) 4697–4735.

[139] D. Venturi, X. Wan, G. E. Karniadakis, Stochastic low-dimensional modeling of random laminar wake past a circular cylinder, preprint.

[140] B. Ganapathysubramanian and N. Zabaras, A stochastic multiscale framework for modeling flow through heterogeneous porous media, Journal of Computational Physics, under review.